SAPIENZA
UNIVERSITÀ DI ROMA

Orbit Determination and Time Synchronization for a Lunar Radio Navigation System

Department of Mechanical and Aerospace Engineering
Ph.D. in Aeronautical and Space Engineering (XXXVII cycle)

Andrea Sesta
ID number 1757970

Advisor
Prof. Luciano Iess

Co-Advisor
Prof. Daniele Durante

Academic Year 2023/2024

Thesis not yet defended

Orbit Determination and Time Synchronization for a Lunar Radio Navigation System
PhD thesis. Sapienza University of Rome

This thesis has been typeset by LaTeX and the Sapthesis class.

Author's email: andrea.sesta@uniroma1.it

Dedicated to
MP and DV

Abstract

Interest in lunar exploration has significantly increased in recent years due to the potential for a permanent human presence on the Moon and its value as a testing ground for deep space exploration technologies. In this scenario, the European Space Agency's Moonlight concept proposes deploying a Lunar Communication and Navigation Service (LCNS) constellation of 4-5 small satellites in Elliptical Lunar Frozen Orbits (ELFOs). This system would offer Position, Navigation, and Timing (PNT) services to cis-lunar platforms and lunar surface users.

During phases 0 and A of the Moonlight project, the ATLAS consortium[1] proposed a Lunar Radio Navigation System (LRNS) architecture. This system includes ground support and tracking via a network of small parabolic antennas (approximately 26 cm diameter) operating at K-band (22-27 GHz). The antennas can track multiple satellites simultaneously using Multiple Spacecraft Per Aperture (MSPA) tracking, enabled by Spread Spectrum (SS) modulation with unique codes for each satellite. Onboard transponders establish two-way coherent links to the ground, enabling precise Doppler and ranging measurements with chip rates of 20-25 Mcps. MSPA, combined with SS modulation, facilitates Same Beam Interferometry (SBI), which uses a single ground station to differentiate phase measurements of two satellites, reducing common-mode noise errors and providing accurate relative position measurements to complement Doppler and range.

My work focused on orbit determination and time synchronization simulations for the LRNS system to evaluate performance and define navigation message accuracy requirements. I analyzed the constellation's performance across different scenarios, assessing the effect of orbital maneuvers and the improvements from the additional SBI data compared to Doppler and range measurements alone. Additionally, I considered different media calibration systems at ground stations, such as Global Navigation Satellite System (GNSS) calibration and Water Vapor Radiometers (WVRs) for tropospheric and ionospheric correction, evaluating their effect on the satellite constellation positioning accuracy.

A key parameter for the architecture is the Signal-In-Space Error (SISE), primarily related to the ephemerides reconstruction of the satellite constellation and clock desynchronization error. The evolution of SISE as a function of the Age Of Data (AOD) determines navigation message accuracy over time, dictating message validity and imposing constraints on the update frequency. Thus, realistic dynamical mismodeling was included in the orbit determination simulation.

The LRNS constellation enables positioning at the Moon's South Pole, but it can be exploited for navigation of secondary users if the satellites are in view. In the second part of the thesis, I focused on assessing the performance of autonomous orbit determination performed during a lunar transfer orbit using both GNSS and LRNS data. This approach significantly reduces mission costs by eliminating the need for ground station support and alleviates associated time and technical constraints, thus paving the way for autonomous guidance of satellites toward the Moon.

[1]The ATLAS consortium has been led by Prof. Luciano Iess from the Center for Aerospace Research of Sapienza (CRAS), University of Rome, with the participation of academic and industrial partners (CNRS/Université de la Cote d'Azur, Insitute of Geodesy and Geomatic of the Wroclaw University, Argotec and Leonardo)

Contents

List of Figures

List of Tables

List of Acronyms

ADEV	Allan Deviation.
AOD	Age Of Data.
BER	Bit Error Rate.
BIPM	Bureau International des Poids et Mesures.
BPSK	Binary Phase-Shift Keying.
CCSDS	Consultative Committee for Space Data Systems.
CDM	Code Division Multiplexing.
CDM-M	Code Division Multiplexing with Majority voting.
CDMA	Code Division Multiple Access.
CE	Code Epochs.
CRAS	Center for Aerospace Research of Sapienza.
DDOR	Delta-Differential One-way Ranging.
DLL	Delay Lock Loop.
DOP	Dilution Of precision.
DSA	Deep Space Antenna.
DWE	Direct-With-Earth.
ECSS	European Cooperation for Space Standardization.
ELFO	Elliptical Lunar Frozen Orbit.
EOP	Earth Orientation Parameters.
ESA	European Space Agency.
ESOC	European Space Operations Centre.
ESTRACK	European Space Tracking network.
EUFR	External Ultra-stable Frequency Reference.
FOC	Full Operational Capability.
FOV	Field Of View.
GNSS	Global Navigation Satellite System.
GODOT	General Orbit Determination and Optimisation Toolkit.
GPS	Global Positioning System.
GTO	Geostationary Transfer Orbit.

HPBW	Half Power Beam-Width.
ICRF	International Celestial Reference Frame.
IOC	Initial Operational Capability.
ISECG	International Space Exploration Coordination Group.
ITRF	International Terrestrial Reference Frame.
JPL	Jet Propulsion Laboratory.
LCNS	Lunar Communication and Navigation Service.
LEOP	Launch and Early Orbit Phase.
LNA	Low Noise Amplifier.
LNSP	LunaNet Service Provider.
LOS	Line Of Sight.
LRNS	Lunar Radio Navigation System.
MAI	Multiple-Access Interference.
MGA	Medium Gain Antenna.
MSPA	Multiple Spacecraft Per Aperture.
MTO	Moon Transfer Orbit.
NASA	National Aeronautics and Space Administration.
OCXO	Oven Controlled Crystal Oscillator.
OD	Orbit Determination.
ODTS	Orbit Determination and Time Synchronization.
OQPSK	Offset Quadrature Phase-Shift Keying.
PLL	Phase Locked Loop.
PN	Pseudo-Noise.
PNT	Position Navigation and Timing.
POD	Precise Orbit Determination.
PVT	Position, Velocity and Time.
RAAN	Right Ascension of the Ascending Node.
RAFS	Rubidium Atomic Frequency Standard.
RF	Radio Frequency.
RFDA	Radio Frequency Distribution Assembly.
RMS	Root Mean Square.
RSS	Root Sum Square.
RTLT	Round-Trip Light Time.
RTN	Radial-Transverse-Normal.
SBI	Same Beam Interferometry.

SFCG	Space Frequency Coordination Group.
SGU	Signal Generation Unit.
SISE	Signal-In-Space Error.
SISRE	Signal-in-Space Ranging Error.
SNR	Signal-to-Noise Ratio.
SPE	Sun-Probe-Earth.
SRP	Solar Radiation Pressure.
SS	Spread Spectrum.
TAI	International Atomic Time.
TC	Telecommand.
TCM	Trajectory Correction Maneuver.
TDB	Barycentric Dynamical Time.
TEC	Total Electron Content.
TLE	Two-Line Element.
TM	Telemetry.
TML	Truncated Maximum Length.
TRL	Technology Readiness Level.
TS	Time Synchronization.
TT	Time Transfer.
TT&C	Telemetry, Tracking and Command.
TTCP	Tracking Telemetry and Command Processor.
TWSTFT	Two-Way Satellite Time and Frequency Transfer.
TWTA	Traveling-Wave-Tube Amplifiers.
UEE	User Equipment Error.
UERE	User Equivalent Ranging Error.
UNE	User Navigation Error.
UQPSK	Unbalanced Quadrature Phase-Shift Keying.
USO	Ultra Stable Oscillator.
UTC	Coordinated Universal Time.
VLBI	Very Long Baseline Interferometry.
WLS	Weighted Least Squares.
WVR	Water Vapor Radiometer.
ZTD	Zenith Total Delay.
ZWD	Zenith Wet Delay.

Chapter 1

Introduction

In recent years, the interest in lunar exploration has grown substantially, both for the intrinsic value of a permanent human presence on our satellite and its use as a relatively close place to test the required technologies for human deep space exploration. Major factors in the renewed interest in the Moon are the challenges of a human mission to Mars and the recent discovery of water ice in the South Pole of our moon (International Space Exploration Coordination Group (ISECG) [ISECG, 2018]). Indeed, the Moon has become a major objective not only for the National Aeronautics and Space Administration (NASA) [NASA, 2020b] and the European Space Agency (ESA) [ESA, 2022a], but also for private actors, with several dozens of commercial and institutional missions already planned for the coming decade [NASA, 2020a]. Moreover, according to Euroconsult (an international consulting and analyst firm specialized in satellite applications, communications, and digital broadcasting), the number of missions planned for our natural satellite is expected to grow exponentially over the next decade. The number of missions is projected to increase by a factor of 5, with anticipated total expenses of 142.4 billion USD (nearly three times the budget of the previous decade), as illustrated in Fig. 1.1. This indicates that the lunar market will play a significant role in the future space economy [Euroconsult, 2023].

In the past years, communications and navigation of lunar missions relied almost entirely upon Direct-With-Earth (DWE) radio links (e.g., NASA's LRO mission, [Vondrak et al., 2010]). However, some missions adopt different approaches to satisfy the need for communication and navigation, such as Chang'e-4 [Li et al., 2021] and CAPSTONE [Cheetham et al., 2022], where a third satellite (dedicated or not) is utilized to guarantee the positioning, or LuGRE [Parker et al., 2022] and Lunar Pathfinder [Giordano et al., 2022] that exploit terrestrial GNSS side-lobe signals for the PNT of the spacecraft. On the one hand, the use of a relay satellite for each lunar user has two major disadvantages:

1. The necessity to design and build a dedicated satellite increases the overall cost of the mission.

2. The additional spacecraft still needs to rely on ground for the positioning and timing.

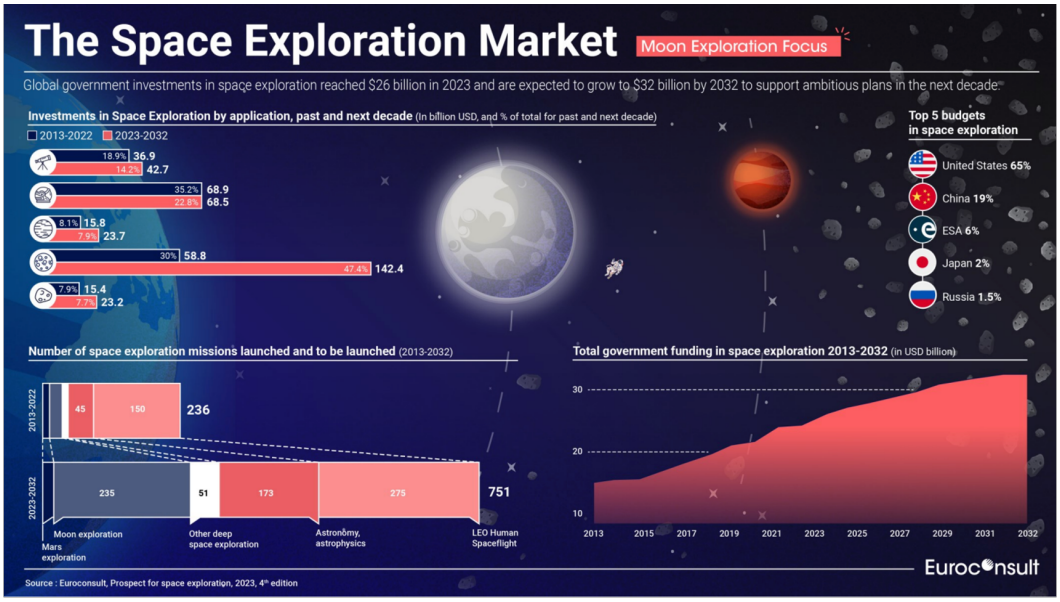

Figure 1.1. Euroconsult prevision for space exploration for the 2023-2032 decade with a comparison with the previous one (2013-2022) [Euroconsult, 2023]

Thus, the large number of lunar missions will still drastically increase the load on the ground infrastructure. On the other hand, even if the use of terrestrial GNSS signals would allow not relying on ground station support, the main drawback of this approach is the low positioning accuracy for the users in the cislunar space, mainly due to the low signal-to-noise ratio at Earth-Moon distance and the elevated Dilution Of precision (DOP) of the GNSS observations [Capuano et al., 2016]. Indeed, since the Earth-Moon distance is much greater than the orbit radius of GNSS satellites, the signals from these spacecraft reaching a user in cislunar space essentially originate from the same region of space, leading to an elevated DOP (see Eq. 1.1).

Conversely, implementing a Lunar Radio Navigation System (LRNS) would be a cost-effective approach to providing reliable communication and navigation services in support of the next generation of institutional and private lunar exploration missions. It would also enhance the performance of those missions currently under development [Giordano et al., 2021a]. Moreover, the ability to rely on a GNSS-like system is essential for missions that require near-real-time PNT services, which are particularly crucial for future manned missions on our natural satellite.

In this context, NASA and ESA have proposed LunaNet, envisioned as a network of cooperating networks (a "network of networks," similar to the terrestrial Internet) designed to provide communications, navigation, and other services to users on and around the Moon. LunaNet is built on a framework of mutually agreed-upon standards, protocols, and interface specifications that enable interoperability. This open and adaptable architecture is intended to allow for a wide range of lunar mission users to access services from diverse commercial and governmental providers. LunaNet Service Providers (LNSPs) can offer services such as communications, messaging, data transmission, and the distribution of position, navigation, timing, and situational awareness information [NASA and ESA, 2023].

As part of this concept, ESA has proposed the Moonlight initiative, which aims to deploy a Lunar Communication and Navigation Service (LCNS) through a constellation of small satellites (4-5 spacecraft) in Elliptical Lunar Frozen Orbits (ELFOs). These satellites will provide PNT services to platforms in cislunar orbits as well as users on the lunar surface. The chosen orbits offer not only extensive coverage of the Moon's southern polar region—a key area for several upcoming missions [Schönfeldt et al., 2020]—but also long-term stability, reducing the need for frequent orbit-keeping maneuvers [Grenier et al., 2022].

The main requirement of any satellite radio navigation system is to guarantee an accurate PNT service for its users. Similar to Earth-based GNSS systems, the performance of the final user (such as lunar rovers or probes) depends on ranging errors and the constellation's observation geometry. The individual ranging error is quantified as the User Equivalent Ranging Error (UERE). The components of the UERE can be further divided into the Signal-in-Space Ranging Error (SISRE) and the User Equipment Error (UEE) [Montenbruck et al., 2018]. The geometry factor affecting the final user positioning error is represented by the DOP, a dimensionless parameter. The User Navigation Error (UNE) can be expressed as:

$$UNE = DOP * UERE = DOP * \sqrt{SISRE^2 + UEE^2} \tag{1.1}$$

The DOP is a scalar indicator of the overall quality of the least squares solution, calculated as the square root of the sum of the variances of the estimated east, north, and up components of the receiver position, as well as the estimated receiver clock offset. Fundamentally, DOP values depend on the volume of the polyhedron formed by the receiver-satellite unit vectors: a larger volume corresponds to smaller DOP values. Key contributors to the UERE error budget include: broadcast satellite orbit error, broadcast satellite clock error, broadcast group delay, unmodeled ionospheric delay, unmodeled tropospheric delay, multipath effects, and receiver noise [Langley et al., 2017]. The SISRE parameter, a critical performance indicator for terrestrial navigation systems, can also be applied to evaluate user positioning performance for lunar navigation systems. The calculation of SISRE should follow the methodology outlined by [Montenbruck et al., 2018]:

$$SISRE = \sqrt{\left(w_1^2 R^2 - 2w_1 RT + T^2\right) + w_2^2 \left(A^2 + C^2\right)} \tag{1.2}$$

where w_1 and w_2 are constellation-specific weight factors for the radial and along/cross-track components, while R (radial), A (along-track), C (cross-track) and T denote the 'orbit errors' and 'timing errors' respectively.

However, the key performance parameter selected for the LunaNet service is slightly different from the one used for Earth-GNSS discussed earlier. It is the Signal-In-Space Error (SISE) defined as the instantaneous difference between the position, velocity, and time of a LunaNet node as broadcasted by that node's navigation message and the true satellite Position, Velocity, and Time (PVT) respectively expressed in the lunar reference system and the lunar time system standard [NASA and ESA, 2023]. This definition is independent of the orbital characteristics of each LunaNet node and sets an upper bound on the user-level error,

which results from projecting the SISE onto the user-satellite line of sight. This ensures that users can derive reliable navigation solutions when utilizing navigation messages from different LNSPs, including ESA's Moonlight LCNS. The SISE can be defined both for position and velocity as:

$$SISE_{pos} = \sqrt{(x-\bar{x})^2 + (y-\bar{y})^2 + (z-\bar{z})^2 + (ct-c\bar{t})^2} \tag{1.3}$$

$$SISE_{vel} = \sqrt{(\dot{x}-\dot{\bar{x}})^2 + (\dot{y}-\dot{\bar{y}})^2 + (\dot{z}-\dot{\bar{z}})^2 + \left(c\dot{t}-c\dot{\bar{t}}\right)^2} \tag{1.4}$$

where x, y, z, $\dot{x}$, $\dot{y}$, $\dot{z}$ are the true coordinates of the spacecraft at time t (in the lunar frame and coordinate time scale) with a clock drift $\dot{t}$ and $\bar{x}$, $\bar{y}$, $\bar{z}$, $\dot{\bar{x}}$, $\dot{\bar{y}}$, $\dot{\bar{z}}$, $\bar{t}$, $\dot{\bar{t}}$ are the broadcasted coordinates and time (and clock drift), where $\bar{t}$ includes the clock corrections within the navigation message and c denotes the speed of light. Although the SISE is nearly invariant with respect to the chosen reference frame (apart from relativistic transformations), it is better expressed in the reference frame and time scale adopted for the constellation. Given this definition, it is clear that the positioning (and velocity) accuracy of any satellite radio navigation system is related to three main factors:

1. The accuracy of the satellite ephemerides.
2. The accuracy in synchronizing the clocks across the constellation and to terrestrial time (e.g., UTC).
3. The accuracy in the realization of a body reference frame (in this case a lunar one).

These principles have driven the design of the ATLAS architecture of an Orbit Determination and Time Synchronization (ODTS) system, developed in the framework of the Moonlight project funded by ESA. It is important to note that we did not select a specific timescale for the LRNS, given that it does not affect the ODTS performance presented in this work, being based on two-way coherent measurements. Indeed, once a timescale has been selected from an operative point of view, it is straightforward to transform it from the Barycentric Dynamical Time (TDB, Temps Dynamique Barycentrique) that we used to perform the trajectory integration and orbit determination (OD).

During my Ph.D., I performed the orbit determination of the satellite constellation to evaluate the proposed system performance and validate this novel architecture. I analyzed the satellite positioning accuracy in different scenarios and with different assumptions to fully characterize the expected navigation message accuracy for the lunar end users of the PNT service. This trade-off analysis allows us to understand the needed requirements for the system architecture to obtain a certain positioning accuracy for the satellite of the constellation. The structure of the work is as follows. First, a detailed description of the system architecture is given. Then, I present the methodology of the orbit determination process and a brief description of the Python package to perform the OD simulations of the lunar satellite constellation. After that, the analysis of the baseline configuration of the architecture is presented. Then,

the validation of the system performance under different scenarios and assumptions is given.

Finally, during my visiting period in the Mission Analysis section at ESA/ESOC, I proposed and investigated the performance of a possible application of the LRNS constellation to Moon Transfer Orbit (MTO), enabling autonomous orbit determination for the analyzed satellite. To perform all these analyses I developed additional Python packages to complement the ESA software GODOT (General Orbit Determination and Optimisation Toolkit) allowing to handle and model radio-link definitions and computations and setup and perform OD.

Following this outline, Chapter 2 describes the novel ATLAS system architecture in terms of constellation geometry, ground station infrastructure, radio tracking system used, and signal structure for the navigation message. Chapter 3 reports the detailed models of the used radio measurements, the different media calibrations proposed together with their impact on the observables error budget, and the desynchronization observables with the associated time transfer techniques. In Chapter 4, the description of the orbit determination process is given. Then, chapter 5 presents the developed Python package to interface with the ESA software GODOT enabling the LRNS system analysis. The ODTS simulations for the baseline proposed architecture and the additional analysis and comparison of the performances in different scenarios are detailed respectively in chapters 6 and 7. Finally, chapter 8 presents the additional use case of the LRNS system that I proposed in combination with the GNSS to perform a MTO orbit determination. Conclusions are given in Chapter 9.

Chapter 2

Lunar Radio Navigation System Architecture

2.1 Architecture Outline

As described in the previous chapter, one of the key performance parameters for any satellite navigation system is the positioning accuracy of the satellites. This metric directly influences the expected quality of the PNT (Position Navigation and Timing) service for the end user. However, it is not the only important aspect of a satellite positioning system. Indeed, in the development of the ATLAS architecture, the main parameters guiding the LRNS (Lunar Radio Navigation System) design are:

1. Ephemeris and time transfer accuracy.
2. System and operational complexity, including ground and space segment requirements.
3. Technological maturity (including technology reuse).
4. Degree of autonomy.
5. Service availability.
6. Scalability (using an arbitrary number of satellites, ground stations, or pseudolites). In the proposed concept, the pseudolites are reference beacons on the lunar surface equipped with the same transceiver hosted onboard the satellites of the constellation, acting as 'satellites' whose ephemerides are perfectly known.

Other important aspects, such as the robustness of the configuration against failure modes and out-of-nominal performances, development time, and lifetime of the system have not been considered, as it is reasonable to neglect them in this preliminary phase of the project.
In principle, every architecture needs to support three phases:

1. Launch and Early Orbit Phase (LEOP).

2. Spacecraft emergencies.

3. Normal operations.

With no specific details available about the LEOP phase, and considering that the constellation could either be deployed from a carrier already in lunar orbit or each satellite could autonomously reach its lunar orbit from Earth, the focus is placed on normal operations, while ensuring full support for spacecraft emergencies.
The selection of the proposed architecture is guided by three key principles, in addition to the previously mentioned metrics:

1. Keep the architecture as simple as possible, while at the same time making it expandable to include new features.

2. Identify augmentations for future steps and improved performances.

3. Outline systems suited for rapid deployment, while at the same time able to meet predicted user needs for at least one decade or more.

The architecture is based upon a network of small ground antennas (diameter dish around 30 cm) dedicated to the support and tracking of the four satellites in ELFO orbits of the lunar constellation. The small antenna apertures are needed to have all the satellites of the constellation in common view thus exploiting the concept of Multiple Spacecraft per Aperture (MSPA). This approach enables the use of a novel data type, the Same Beam Interferometry (SBI) (described in chapter 3), in conjunction with standard radio tracking techniques (Doppler and ranging), complemented by ground GNSS signals received onboard [Iess et al., 2023].

Another relevant feature of the implementation of MSPA is the large gain in tracking time and the availability of ground support. In practice, all satellites would be tracked simultaneously, without the need for time-sharing inherent in a sequential approach. This nearly continuous contact between each satellite of the constellation and at least one ground station enables, in addition to the ODTS (Orbit Determination and Time Synchronization) functions, a quite significant data volume exchange across the radio link (telecommands, housekeeping, navigation message, etc.), despite the use of small ground antennas. Moreover, MSPA allows also a more frequent Time Transfer (TT), thus posing less stringent requirements on the onboard clock stability. The ground segment modulator (a component that modulates the transmitted signals to the spacecraft, see Section 2.2.1) and the ground segment receiver (a component that receives and demodulates the signal sent by the satellites, see Section 2.2.1) have to be properly upgraded to implement this MSPA approach, namely:

- the Code Division Multiplexing with Majority voting (CDM-M) scheme (with four spread spectrum (SS) signals) for the uplink signal generation.

- the Code Division Multiple Access (CDMA) receiver capable of processing in parallel (simultaneously) four downlink SS signals [Rovelli and Donà, 2016] (see Section 2.2.1).

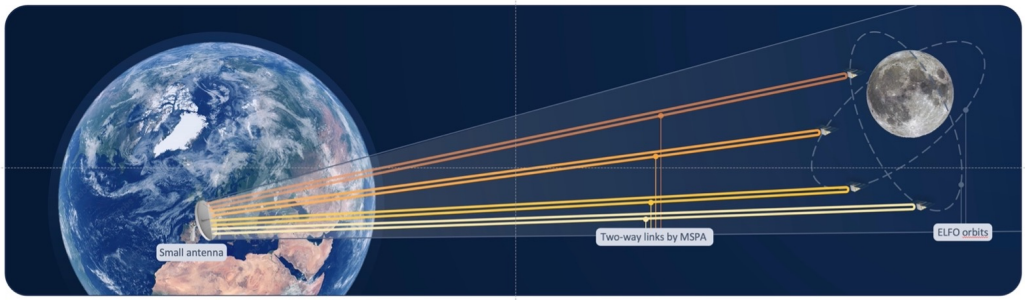

Figure 2.1. Proposed architecture for the LRNS with MSPA approach. This configuration allows to perform simultaneously TT&C operations, acquisition of Doppler, range and SBI measurements, and time transfer for all four satellites of the constellation [Iess et al., 2023]

There are no significant impacts of the MSPA approach for the onboard transponders, which shall support CDMA and Telemetry, Tracking, and Command (TT&C). Fig. 2.1 represents a schematic view of the proposed architecture described above.

The decision to adopt a dedicated network of small antennas for LRNS tracking not only ensures full operational independence from other networks (commercial or otherwise) but also performs well against the metrics outlined earlier. Specifically, using small antennas allows for easily scaling of the system incrementing the number of ground stations, while also containing the system's complexity. As for the placement of the proposed ground stations, it is suggested that they be located at the site of the European Space Tracking (ESTRACK) network. These Deep Space Antenna (DSA) locations offer the following advantages:

1. The availability of highly stable frequency standards, needed by the lunar network (e.g., H-masers).

2. An excellent positional accuracy in the International Terrestrial Reference Frame (ITRF) including its time variability due to plate motion (<3 cm - typical deep space antenna levels).

3. Good synchronization to the International Atomic Time (TAI, Temps Atomique International) and to the Coordinated Universal Time (UTC).

4. The capability to synchronize clocks at different ground station complexes using Very Long Baseline Interferometry (VLBI) observations (using the 35 m antennas) [Wang et al., 2019].

5. The availability of tropospheric and ionospheric path delay estimates from GNSS calibration data for the ESTRACK sites [Feltens et al., 2018] (which could technically be extended to other sites if similar data are available).

6. The availability of wet tropospheric delays from dedicated Water Vapor Radiometers (WVRs) if located close enough to the LRNS tracking antennas, even if this instrumentation is currently available only at the Malargüe site.

7. A generally dry site favorable to deep space tracking and about 120° space in longitude among the three ground station complexes (for continuous coverage).

Proximity to a large antenna could facilitate better coordination between the lunar and deep space networks for special operations, such as simultaneous 2-way and 3-way tracking, which is useful for troubleshooting and cross-checking measurements. Nonetheless, any site offering similar infrastructure and performance should be considered a viable option for the system. For practical purposes, and considering a minimum elevation mask of 15°, the addition of a fourth tracking site appears essential to ensure continuous visibility of the constellation (see Chapter 6).

2.2 Radio System Architecture

Even if I analyzed different configurations to determine the performance of the proposed LRNS, the baseline of the radio system architecture for the TT&C of the constellation during nominal operations and for the orbit determination and Time Synchronization (TS) is based on two main design choices that drive the LCNS performance, the signal structure definition and the ground and onboard hardware.

The first design choice is to adopt the K-band for the uplink and downlink signals, this key aspect of the baseline architecture differentiates this concept from other lunar navigation systems (e.g., [Stallo et al., 2023]). The use of K-band over the X-band is related to the fact that, even if the X-band technology is widely used in TT&C deep space and near-Earth communications, the frequency spectrum is more crowded and suffers a quite limited bandwidth allocation from the Space Frequency Coordination Group (SFCG) (<6 MHz). Instead, the K-band allows a broader frequency allocation (>6 MHz see [SFCG, 2023b]), thus resulting in:

- scalable system, with the possibility to easily increase the number of spacecraft of the LRNS.
- higher chip-rate for the ranging observations and therefore more accurate measurements and time transfer

Moreover, the K-band radio link has a greater immunity to ionospheric path delay effects on range and range rate. The second key characteristic of the proposed LRNS is the MSPA approach that allows us the use of the SBI in conjunction with the SS range and Doppler, thus relying on ground station for the ODTS instead of adopting an onboard approach based on GNSS observation (e.g., [Murata et al., 2022]). Finally, the choice to adopt the K-band instead of the Ka-band ensures the compliance with the frequency band allocation for communication in the lunar region recommended by the Space Frequency Coordination Group [SFCG, 2023a].

2.2.1 Ground Segment and Signal Structure

As said in the previous section, one of the main design choices of the architecture is to adopt a Code Division Multiplexing (CDM) scheme based on SS modulation. This allows us to allocate the same frequency band to the spacecraft of the four satellites of the constellation, saving spectral resources at the expense of additional design complexity for the ground station modem and the onboard transponder.

The implementation of the CMD technique in a MSPA scheme enables the simultaneous tracking, control, and synchronization of the entire constellation as shown in Fig. 2.1. However, the MSPA approach requires that the entire constellation is within the main lobe of the ground antenna, thus the constellation geometry drives the maximum size of the ground terminal given the band of the radio link. To optimize the antenna pointing and dimension, it is possible to adopt a minimum enclosing circle algorithm to find the maximum antenna dish dimension usable to track all the spacecraft simultaneously. Different implementations of the algorithm can be utilized. By predicting the spacecraft's position, the minimum enclosing circle can be computed at various time intervals. The antenna pointing will then track the center of the calculated circle, with the antenna dish sized appropriately according to the circle's radius. The analysis shows that a Half Power Beam-Width (HPBW) of about 3 degrees guarantees a 99% visibility of the entire constellation (see Chapter 6 for the analyzed spacecraft orbital parameters). This HPBW angle corresponds to a dish antenna diameter of 26 cm at the K-band. These small antennas are easily maintained and inexpensive, however they are more exposed to radiation disturbances from the surrounding environment. Therefore, it is necessary to adopt a resilient signal structure and, if possible, locate the ground station in electromagnetically clean sites.

In the initial deployment phase of the system, given the limited number of satellites (4-5), the ground network entails at least two small antennas per site, one used for nominal tracking operations and one for redundancy purposes. Moreover, to guarantee global coverage and to avoid short-tracking passes and poor visibility (low elevations) of the spacecraft orbiting the Moon, it is possible to consider additional tracking sites (at least one). This feature reduces the unavoidable visibility gap related to geometry conditions and the tracking elevation mask. If the three ESTRACK sites are used (see baseline configuration analyzed in Chapter 6), the additional station to assure global coverage must be in the Pacific region, e.g. Mauna Kea, Hawaii. The minimum elevation mask used for the ground operations and computation of the link budget is 15° degrees, even if it could be increased to 20° degrees with the addition of the fourth ground station site. Fig. 2.2 illustrates the data flow within the ground segment. Antennas at each site gather radio tracking observables and telemetry from the satellite constellation. This information is then transmitted to an operations center, where spacecraft ephemerides are calculated and time synchronization algorithms are executed. Finally, updated data is uploaded to the constellation to refresh the spacecraft's position and clock settings.

As mentioned earlier, the transmitted signals use SS modulation, a technique employed by GNSS systems ([Teunissen and Montenbruck, 2017]). This modulation allows for simultaneous signal transmission, improved time-delay resolution, and strong resistance to interference, particularly with longer SS sequences [Meurer and Antreich, 2017]. The Spread Spectrum modulation allows a signal generated with a certain bandwidth to be spread over a wider frequency band. This spreading operation is performed by modulating the original signal with a pseudo-random noise code, which is a binary ± 1 sequence of period L whose periodic autocorrelation function has peak value +L and all (L–1) off-peak values equal to –1. This code is then used in the 'despreading' operation at the receiver to retrieve

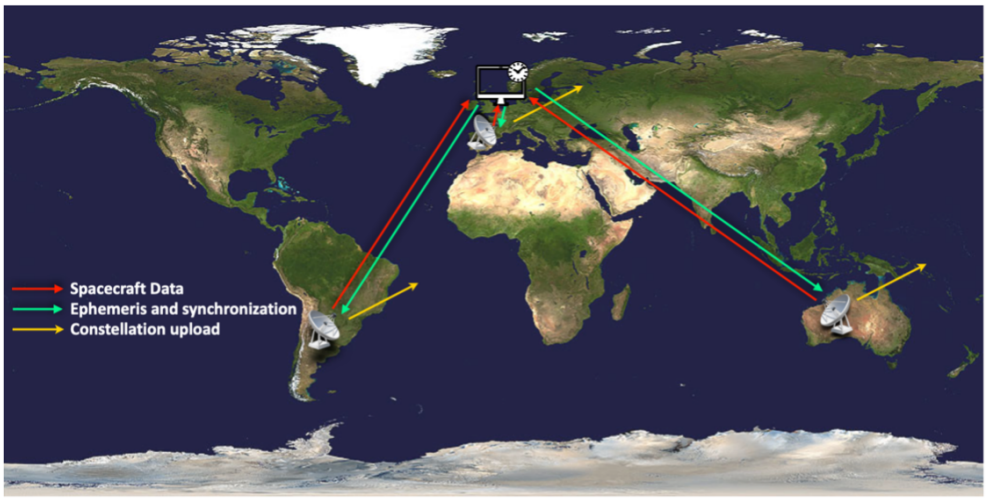

Figure 2.2. Ground segment data flow in the LRNS architecture

the original signal from the modulated one. The SS modulation is fundamental for CDMA, where multiple transmitted signals share the same communication channel, each assigned a unique code. This is how GNSS enables simultaneous communication with various satellites. In the proposed LRNS, this approach allows communication with all the satellites in the constellation simultaneously, by assigning a different pseudo-random noise code to each satellite for modulation and demodulation.

The signal structure proposed in [Iess et al., 2023] enables the transponder to operate in two configurations: coherent and non-coherent modes. This affects the capability to perform OD&TS functions in parallel or sequentially, influencing the duration of the tracking windows available for collecting observables from the ground stations.

2.2.2 Onboard Radio System

The onboard radio tracking system, depicted in Fig. 2.3, consists of:

- One 30 cm steerable Medium Gain Antenna (MGA) with two degree of freedom for nominal operation.
- Two LGAs for quasi-omnidirectional coverage when the MGA is not available, i.e. in LEOP or contingency phases.
- Two redundant K-band dual-mode transponders, with hot redundancy for the RX and cold redundancy for the TX. This means that during nominal operation, the redundant transponder unit uses only the RX module (TX module inactive), while the main transponder is fully active, utilizing both the TX and RX modules.
- Two Traveling-Wave-Tube Amplifiers (TWTA, 10W) in cold redundancy. This means that the backup TWTA remains inactive unless needed.

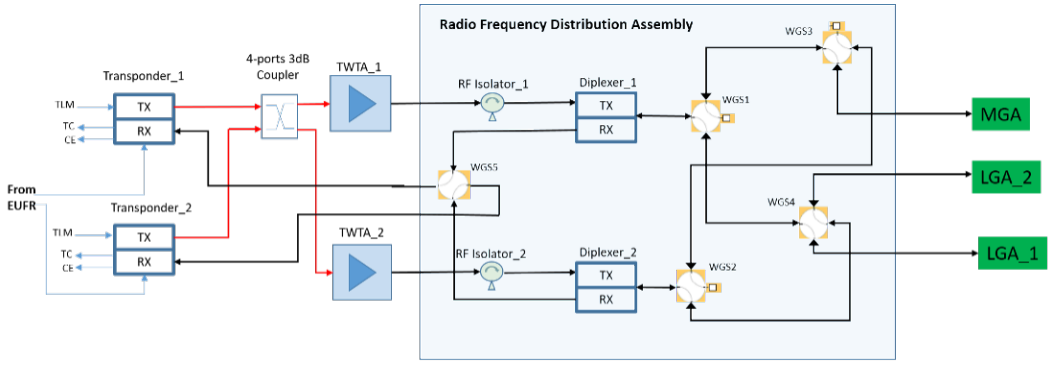

Figure 2.3. Onboard RF system configuration in K-band [Iess et al., 2023]

- The Radio Frequency Distribution Assembly (RFDA), including two diplexers and five switches for signal routing to/from the antennas.

- Waveguides (in black) to minimize the Radio Frequency (RF) path losses, while coaxial cables (in red) can be used on the transmitter side before signal amplification.

This configuration is robust given that the mission is not compromised in case of failure of one transponder or one TWTA.

Looking at Fig. 2.3, it can be observed that the inclusion of a coupler in the TX chain before the two TWTAs allows seamless cross-strapping between the transponders and the amplifiers. This configuration ensures that, in the event of a failure of either a transponder or a TWTA, both transponders can remain connected to both TWTAs, thus improving system reliability. Additionally, the RFDA assembly provides the following capabilities:

- Maintaining the nominal transponder connected to the MGA during regular operations, while the redundant transponder (RX-ON and TX-OFF, as described earlier for hot and cold redundancy in RX and TX) is connected to one of the two LGAs, remaining ready for telecommand (TC) demodulation.

- Ensuring each transponder is connected to one of the two LGAs in contingency scenarios, providing near-omnidirectional coverage for continuous contact with the ground station.

- Reducing RF losses and minimizing the impact on the link budget by using switches instead of couplers.

The K-band TT&C transponder interfaces with:

- The onboard computer sends demodulated telecommands and receives the telemetry data stream, which is then modulated and downlinked to the ground station.

- The Signal Generation Unit (SGU) for Pseudo-Noise (PN) code epoch time-stamping and frequency synchronization with the External Ultra-stable Frequency Reference (EUFR), as required for TT operation (see Chapter 6 for the proposed and analyzed onboard clocks).

The transponders are also equipped with an internal oscillator, typically an Oven Controlled Crystal Oscillator (OCXO), for TT&C operations when the EUFR is not required or available. However, synchronization of the transponder frequency with the EUFR is strongly recommended in SS mode to minimize the signal frequency range acquisition, which would otherwise be affected by the OCXO's frequency instability. Additionally, this synchronization is considered essential for asynchronous TT functionality.

2.3 Link Budget

The key design feature of the proposed architecture is the MSPA concept, which also enables the implementation of SBI (see Chapter 3). Given the relatively short Earth-Moon distance and the high directivity achievable at K-band, the antenna size is limited to approximately 26 cm. Despite this small size, it is sufficient to ensure adequate data rates for the radio links. A pointing strategy based on the minimum enclosing circle reduces pointing losses from the ground to less than 3 dB for 99% of the time, with an average of 1.3 dB.

Table 2.1 shows the link budget for nominal operations, calculated under conservative assumptions: a fixed link elevation of 15°, transmission power limited to 200 W from the ground and 10 W onboard, a maximum Earth-Moon slant range, and worst-case pointing losses. Additionally, a room-temperature Low Noise Amplifier (LNA) is assumed on the ground. Atmospheric attenuation statistic, cited from [DSN, 2015], refers to a deep space antenna site with a Cumulative Distribution (CD) factor of 0.9. This means that 90% of the time a particular weather effect (in this case atmospheric attenuation) is less than or equal to a given value. Vice versa, that specific effect is exceeded 10% of the time. Qualitatively, the weather conditions associated with selected cumulative distributions are described in [DSN, 2015] as follows:

- CD = 0.00: clear dry, lowest weather effect.
- CD = 0.25: average clear weather.
- CD = 0.50: clear humid, or very light clouds.
- CD = 0.90: very cloudy, no rain.
- CD > 0.95: very cloudy, with rain.

Choosing a dry site is crucial not only to minimize attenuation (which is non-negligible at K-band), but also to reduce tropospheric effects that degrade the quality of radiometric measurements, and to ensure an electromagnetically clean

environment. This is particularly important for small dishes, which are more susceptible to radiation interference from their surroundings. Transmission power from the ground can be easily increased by a factor of 2 or 3 (or more) if enhanced uplink performance is desired. However, onboard RF power is expected to be limited, as this architecture assumes a small satellite platform dedicated to navigation services, in line with the Moonlight concept. Considering the power and pointing requirements, a steerable MGA with a 30 cm dish has been selected for the spacecraft.

The carrier SNR for the uplink and downlink is 38 dBHz and 35 dBHz, respectively, for each satellite link in the constellation, including a 3 dB link margin, as per European Cooperation for Space Standardization (ECSS) standards. Uplink SNR is mainly constrained by the power-sharing loss introduced by CDM-M, which results in an 8.5 dB loss for 4 (or 5) spacecraft, as described in [Donà and Iess, 2017]. These losses would become prohibitively large if the constellation is expanded in the future. To mitigate this, the strategy would be to group 4 or 5 satellites and use additional ground antennas to simultaneously track each group. This would be a cost-effective solution given the small size of the ground terminals. The signal level obtained is considered sufficient for acquisition, provided that the onboard receiver can handle an acquisition window of $\pm$130 KHz. Due to MSPA, uplink pre-steering can only be based on the spacecraft-averaged Doppler shift and Doppler rate resulting from CDM-M. However, for the downlink, the ground station can independently adjust the frequency for each satellite (thanks to the CDMA channel), making pre-steering much more effective.

Telecommand (TC), telemetry (TM), and ranging SNR are calculated based on the signal modulation schemes suggested in [Donà and Iess, 2017]: Unbalanced-QPSK (UQPSK) with a power imbalance of 1:10 for the uplink, and Offset-QPSK (OQPSK) for the downlink. A ranging precision of less than 35 cm in two-way coherent mode can be achieved using a code rate of 24 Mcps, accounting for the jitter contribution from the uplink I-channel SNR and either the I- or Q-channel SNR for the downlink. The uplink format includes only the long PN code used for ambiguity resolution, which is coherently generated from the shorter code used for acquisition on the I-channel. For the downlink, however, only the long code is used for both acquisition and ambiguity resolution. TC and TM data rates are provided for a couple of potential coding schemes. The target Bit Error Rate (BER) is 10^{-5} for telecommands and 10^{-6} for telemetry. Notably, the MSPA concept maximizes data volume rather than data rate, allowing simultaneous and continuous communication with all spacecraft. With approximately 22 hours of tracking per day, the total downlink data volume from each satellite exceeds 110 Mbit/day.

In contingency scenarios, the performance of the small ground antenna becomes insufficient, and a dedicated larger dish, with a diameter of at least 13 meters, is required. In these cases, the MSPA concept is not needed, as the communication link is established with one satellite at a time, using the onboard LGA and standard modulation with a residual carrier, as recommended by the Consultative Committee for Space Data Systems (CCSDS) [CCSDS, 2021].

Table 2.1. Link Budget and bit rates for the architecture LRNS radio link configuration during nominal operations from [Iess et al., 2023]

	Unit	Uplink	Downlink
Frequency	**GHz**	**22.9**	**26.2**
Link Budget			
Ground TX antenna gain (0.55 efficiency)	dBi	33.3	-
Onboard TX antenna assembly gain (including waveguides and rotary joints)	dBi	-	34.7
TX RF Losses	dB	2.0	2.5
On-ground pointing loss	dB	3.0	0.5
TX power	dBW	23	10
EIRP	**dBW**	**51.3**	**41.7**
Free space losses	dB	231.8	233.0
Earth atmospheric losses (elev=15°, CD=90 %)	dB	1.5	1.5
Ground RX antenna gain (0.55 efficiency)	dBi	-	34.5
Onboard RX antenna assembly gain (including waveguides and rotary joints)	dBi	33.5	-
RX RF losses	dB	2.1	2.0
Onboard pointing loss	dB	0.5	3.0
Carrier Power	**dBW**	**-151.1**	**-163.3**
System Noise Temperature (at receiver input)	dBK	27.6	26.8
C/N_0	**dBHz**	**49.9**	**38.5**
CDM-M losses (4 users, Gold code)	dB	8.5	-
Multiple-Access Interference (MAI) loss	dB	-	1.0
Link margin	dB	3.0	3.0
S/N_0 for single satellite	**dBHz**	**38.3**	**34.5**
Telecommands/Telemetry			
Loss for $P_I = 10/11\ P_{TOT}$ (UQPSK)	dB	0.4	-
Demodulation loss	dB	2.0	2.0
Telecommands S/N_0 (I-channel)	dBHz	35.9	-
Telemetry S/N_0 (I and Q channels)	dBHz	-	32.5
Bitrate - LDPC(128, 64) (required E_b/N_0 = 4.7 @ BER = 1e-5)	**kbps**	**1.33**	**-**
Bitrate - LDPC(512, 256) (required E_b/N_0 = 3.3 @ BER = 1e-5)	**kbps**	**1.83**	**-**
Bitrate - CCV & R-S (r=1/2, l=5) (required E_b/N_0 = 2.5 @ BER = 1e-6)	**kbps**	**-**	**1.00**
Bitrate - LDPC(32768, 16384) (required E_b/N_0 = 1.0 @ BER = 1e-6)	**kbps**	**-**	**1.41**
Ranging			
Loss for $P_Q = 1/11\ P_{TOT}$ (UQPSK)	dB	10.4	-
Loss for OQPSK	dB	-	3.0
Demodulation loss	dB	1.0	1.0
S/N_0 (Q-channel)	**dBHz**	**26.9**	**31.5**

Chapter 3

Observable Quantities for ODTS

Satellite orbit determination depends on precise radiometric measurements of the spacecraft's position or velocity, obtained using ground-based instruments. These measurements are derived from the properties of a radio signal traveling between the spacecraft and the receiver. Tracking configurations are categorized based on the source of the reference signal and the number of intervening stations. In a one-way tracking configuration, the spacecraft generates the carrier signal onboard using an oscillator. This signal is then transmitted from the spacecraft and received by an Earth-based antenna. Conversely, in a two-way configuration, the ground station transmits a signal, which is received by an onboard transponder, coherently retransmitted back to the ground, and received by the same ground station.

For the proposed LRNS (Lunar Radio Navigation System), the primary observables are range and range rate (defined in [Moyer, 2003]), provided through a coherent, two-way radio link, as detailed in Chapter 2. Although not strictly necessary to meet the SISE (Signal-In-Space Error) satellite requirements, SBI (Same Beam Interferometry) improves the accuracy and consistency of orbit determination. Thus, SBI is a significant enhancement to our system architecture.

The synchronization among the clocks within the constellation and their alignment with the desired reference time scale are critical to meet the positioning requirements of the LRNS constellation in terms of SISE. To evaluate and predict clock behavior, desynchronization observables are essential.

The following sections will offer a basic overview of how these radiometric observations are measured, with a particular emphasis on the novel SBI observable. Additionally, the principal sources of measurement errors will be discussed. Finally, the proposed time transfer techniques for the LRNS will be presented together with the desynchronization observables that will be used to evaluate the TT contribution to the SISE

3.1 Range-rate Measurements

When a signal is transmitted from a source (S) to a receiver (O), the received signal will exhibit a frequency shift relative to the transmitted signal due to the relative motion between the two: this is known as the Doppler shift effect. The two-way

range rate is determined by measuring the Doppler shift of a radio carrier during its transmission and reception at a ground station. The relationship between the Doppler shift and range rate measurements is straightforward, and a simplified derivation is provided here (the detailed formulation is presented in [Moyer, 2003]). For instance, considering a one-way link from S to O, the monochromatic signal transmitted from S can be described as:

$$s(t) = Re\left[s_0 \exp\left[i\left(\omega_0 t + \phi_0\right)\right]\right] \tag{3.1}$$

the received signal will be delayed, attenuated and Doppler shifted with respect to $s(t)$:

$$s_A(t) = Re\left[s_{0A} \exp\left[i\left(\omega_0 t + \phi_0 - \boldsymbol{k}_A \cdot \left(\boldsymbol{r}_A(t) - \boldsymbol{r}_{sc}(t - \tau_A)\right)\right)\right]\right] \tag{3.2}$$

Where s_{0A} is the attenuated amplitude of the received signal, $\boldsymbol{k}_A$ is the wave vector of the electromagnetic signal at the receiver which takes into account also light-time and aberration, $\boldsymbol{r}_A$ is the position of the receiver in the inertial frame and $\boldsymbol{r}_{sc}$ is the position of the transmitter in the inertial frame (all quantities are referred to the Solar System barycenter), and, finally, τ_A is the light-time between the transmitter and the receiver. It is interesting to note that the term subtracted to the original phase is 2π times the number of wavelengths contained in the distance between S and O, accounting for Doppler shift and delay. The frequency of the received signal will be computed as the time derivative of its phase:

$$\Phi_A(t) = \omega_0 t + \phi_0 + \Psi_A(t) \tag{3.3}$$

where $\omega_0 t$ is the rapidly varying part, while $\Psi_A(t)$ is the slowly varying part due to orbital dynamics, defined as:

$$\Psi_A(t) = \boldsymbol{k}_A \cdot \left(\boldsymbol{r}_A(t) - \boldsymbol{r}_{sc}\left(t - \tau_A\right)\right) \tag{3.4}$$

Then:

$$f = \frac{1}{2\pi}\frac{d\Phi_A(t)}{dt} = f_0 + \frac{1}{2\pi}\frac{d\Psi_A(t)}{dt} \tag{3.5}$$

Thus, the frequency can be written as:

$$\begin{aligned} f &= f_0 - \frac{1}{2\pi}\frac{d\left(\boldsymbol{k}_A \cdot \left(\boldsymbol{r}_A(t) - \boldsymbol{r}_{sc}\left(t - \tau_A\right)\right)\right)}{dt} \\ &= f_0 - \frac{1}{2\pi}\boldsymbol{k}_A \cdot \frac{d\left(\boldsymbol{r}_A(t) - \boldsymbol{r}_{sc}(t - \tau_A)\right)}{dt} = f_0 - \frac{f_0}{c}\frac{d\rho}{dt} \end{aligned} \tag{3.6}$$

where c is the speed of light, ρ is the range, and its derivative is the range-rate. The Doppler shift and the relative frequency shift can be expressed as:

$$\begin{aligned} f - f_0 = -\frac{f_0}{c}\frac{d\rho}{dt} = -f_0\frac{d\tau_A}{dt} &\approx -f_0\frac{v_r}{c} \\ \frac{\Delta f}{f} = -\frac{d\tau_A}{dt} &\approx -\frac{v_r}{c} \end{aligned} \tag{3.7}$$

this formula shows that the relative frequency shift is the time derivative of the light-time τ_A. Thus, the connection between range-rate and Doppler shift is clearly expressed in Eq. 3.7. For a 2-way radio link, one must sum the uplink and downlink

contributions. In this case, the relative frequency shift is the time derivative of the Round-Trip Light Time (RTLT).

The integrated Doppler measurement determines the change in range of a spacecraft ΔR over a given interval (T_0, T_1) by monitoring the carrier phase change that results from the spacecraft's radial motion. For the 1-way Doppler:

$$\Delta R(T_0, T_1) = \int_{T_0}^{T_1} \dot{\rho} dt = \mp \frac{c}{f_{TX}} \int_{T_0}^{T_1} \Delta f dt \tag{3.8}$$

This measurement does not give an absolute value of range but it does give a very accurate measurement of the change in range over a given time interval.

It is clear from the previous formulation that range-rate computation requires the knowledge of Doppler received frequency; however, no tracking equipment can measure frequency directly. Instead, it can only measure phase and finite phase differences. The problem to obtain this approximated Doppler frequency is faced for example through the use of a Phase Locked Loop (PLL). A PLL is a device capable of producing a phase-coherent, less noisy replica of the incoming signal. A digital, open-lop implementation of a PLL is described below.

At the receiver, the signal $s_A(t)$ (expressing the real part of Eq. 3.2) is multiplied by a reference signal $S_r(t)$ whose frequency ω_r is as close as possible (ideally equal) to ω_0, the frequency of the incoming signal:

$$\begin{aligned} s_A(t)S_r(t) = s_{A0}S_{r0}\cos\left(\omega_0 t + \phi_0 + \Psi_A\left(t, \tau_A(t)\right)\right)\exp(-i\omega_r t) = \\ \frac{s_{A0}S_{r0}}{2}\Big\{ \exp\left[i(\omega_0 t + \phi_0 + \Psi_A(t, \tau_A(t)))\right] + \exp\left[-i(\omega_0 t + \phi_0 + \Psi_A(t, \tau_A(t))\right] \Big\}\exp(-i\omega_r t) = \\ \frac{s_{A0}S_{r0}}{2}\Big\{ \exp\left[i((\omega_0 - \omega_r)t + \phi_0 + \Psi_A(t, \tau_A(t)))\right] + \exp\left[-i((\omega_0 + \omega_r)t + \phi_0 + \Psi_A(t, \tau_A(t)))\right] \Big\} \end{aligned} \tag{3.9}$$

It is possible to low-pass filter the mixed signal to remove the second, high-frequency term. This can be accomplished by employing an integrator that acts as a low pass filter; expanding the slowly varying part Ψ_A at the first order about the center of integration $[t_i; t_i + \Delta t/2]$:

$$\Psi_A(t) = \Psi_A(t_i + \Delta t/2) + \dot{\Psi}_A(t_i + \Delta t/2)(t - t_i - \Delta t/2) \tag{3.10}$$

It is possible to write:

$$\int_{t_i}^{t_i+\Delta t} s_A(t)S_r(t)dt = \frac{s_{A0}S_{r0}}{2}\int_{t_i}^{t_i+\Delta t} \exp[i(\omega^- t + \Phi_i)]dt + \frac{s_{A0}S_{r0}}{2}\int_{t_i}^{t_i+\Delta t} \exp[i(\omega^+ t + \Phi_i)]dt \tag{3.11}$$

where:

$$\begin{aligned} \omega^- &= \omega_0 + \dot{\Psi}_A(t + \Delta t/2) - \omega_r \\ \omega^+ &= \omega_0 + \dot{\Psi}_A(t + \Delta t/2) + \omega_r \\ \Phi_i &= \phi_0 + \Psi_A(t_i + \Delta t/2) - \dot{\Psi}_A(t_i + \Delta t/2)(t_i + \Delta t/2) \end{aligned} \tag{3.12}$$

The second integral is the high-frequency part which is much smaller than the first one (and nearly zero), as the integrand function is rapidly oscillating. If the

knowledge of the signal dynamics is good enough or it is possible, based on the history of the signal, to program the frequency of the beat signal to be close enough to the received signal, namely $\omega_r \approx \omega_0$, the first integral could be computed as:

$$Z_i = \frac{s_{A0} S_{r0}}{2} \int_{t_i}^{t_i+\Delta t} \exp[i(\omega^- t + \Phi_i)] dt \approx \frac{s_{A0} S_{r0}}{2} \Delta t \exp(i\Phi_i) \tag{3.13}$$

this is true if $\omega^- \Delta t \ll 2\pi$. It is thus possible to find the amplitude and the phase of the input signal:

$$\begin{aligned} \Phi_i &= \arctan \frac{Im\,(Z_i)}{Re\,(Z_i)} \\ s_{A0} &= \frac{2\,|Z_i|}{\Delta t S_{r0}} \end{aligned} \tag{3.14}$$

So the reconstructed signal is:

$$s_A(t) = \frac{2\,|Z_i|}{\Delta t S_{r0}} \cos(\omega_r t + \Phi_i) \tag{3.15}$$

Finally, the average frequency on the interval is obtained by exploiting the phase of the subsequent time interval:

$$\begin{aligned} f &= \frac{1}{2\pi} \frac{d\Phi_A}{dt} \\ \bar{f}_i &= \frac{1}{2\pi} \frac{\Phi_{i+1} - \Phi_i}{\Delta t} \end{aligned} \tag{3.16}$$

3.2 Range Measurements

The integrated Doppler shift offers a precise measure of the spacecraft's range change over a specific time interval, but it does not provide an absolute range measurement. Instead, the absolute range is determined using the RTLT between the spacecraft and the ground station. In a coherent two-way system, the ground station transmits a modulation on the uplink carrier, which the spacecraft re-transmits back to the ground station. The spacecraft's transponder either demodulates the uplink ranging signal and re-modulates it onto the downlink for improved accuracy (regenerative ranging), or simply re-modulates the carrier without demodulation (transparent ranging). The RTLT of this signal cycle represents the range measurement. The ground station receives the ranging signal, which has been attenuated and phase-shifted, and from this, it calculates the time delay between the transmitted and received signals. For example, the uplink signal might be phase-modulated with a sinusoidal modulation:

$$s(t) = A \sin(\omega_c t + \theta_0 + m_{RNG} \cdot RNG(t)) \tag{3.17}$$

where

$$RNG(t) = \sin(w_{RNG} t + \theta(t)) \tag{3.18}$$

it is possible to rewrite it as:

$$\begin{aligned} s(t) = A \sin(\omega_c t + \theta_0) \cos(m_{RNG} \sin(\omega_{RNG} t + \theta(t))) + \\ A \cos(\omega_c t + \theta_0) \sin(m_{RNG} \sin(\omega_{RNG} t + \theta(t))) \end{aligned} \tag{3.19}$$

Expanding with the Jacobi-Anger identities and neglecting for simplicity higher components ($i > 2$), the result would be:

$$\begin{aligned} s(t) \approx AJ_0(m_{RNG})\sin(\omega_c t + \theta_0) + \\ 2AJ_1(m_{RNG})\cos(\omega_c + \theta_0)\sin(\omega_{RNG} t + \theta(t)) \end{aligned} \tag{3.20}$$

where J_i are the Bessel function of order i. The second term can be written as the sum of trigonometric functions, and the result would show a residual carrier with frequency equal to ω_c and two side-bands, with frequency $f_c - f_{RNG}$ and $f_c + f_{RNG}$. If the modulation of the signal is $A\cos(\omega t$, the modulation received at time t will be $B\cos(\omega(t - (\rho_u + \rho_d)/v_g)$, where v_g is the group velocity. By cross-correlating these two signals (uplink and downlink), the obtained result is:

$$\eta = \frac{1}{T}\int_{t_0}^{t0+T} A\cos(\omega t)B\cos\left(\omega\left(t - \frac{\rho_u + \rho_d}{v_g}\right)\right)dt \approx \frac{AB}{2}\cos\left(\frac{\omega}{v_g(\rho_u + \rho_d)}\right) \tag{3.21}$$

if $T \gg 1/\omega$; therefore:

$$\rho_u + \rho_d = \frac{v_g}{\omega}\left[\cos^{-1}\left(\frac{2\eta}{AB}\right) + 2\pi N\right] = \frac{\lambda}{2\pi}\cos^{-1}\left(\frac{2\eta}{AB}\right) + N\lambda \tag{3.22}$$

From this formulation, it is important to note that the range determination is ambiguous by an integer number of wavelengths $\lambda = (2\pi v_g)/\omega$. However, if an a priori estimate of the range is available, the ambiguity is resolved by using a tone with a wavelength larger than the range uncertainty. The simplest implementation of a ranging system entails the transmission from the ground station of a sequence of decreasing frequency: the low-frequency tones are used to eliminate the phase ambiguity, and the tone/code at the highest frequency defines the accuracy of the measurements. During the integration, the spacecraft is moving and it could also travel for thousands of kilometers since the integration time could last several minutes. A suitable strategy for example is the "Doppler rate aiding": Doppler measurements are continuously taken, and these observations could give information about the change of range in the time interval, therefore the phase of the replica of the transmitted tone stored on ground is modified based on the information brought by Doppler observations. Substantially, in this way, the ground station is artificially put in motion at the same speed as the spacecraft to preserve a constant distance between them and to make the measured range the same as the one at the start of the integration.

An alternative to the classical sequential ranging is represented by the pseudo-noise (PN) ranging, which consists of modulating onto the carrier a random-like binary code. The code is repeated after a predefined number of bits (code length). The signal is received and demodulated by the ground station and the phase shifting is determined by correlating the received code with a replica of the uplink code. The chip length provides the accuracy of the range determination while ambiguities are resolved by the code length. A brief explanation of the SS modulation is presented in Section 2.2.1, while the detailed description of the range observable is presented in [Moyer, 2003] and [Berner et al., 1999].

3.3 Same Beam Interferometry

Same Beam Interferometry (SBI), a radio interferometric technique used for orbit determination, was introduced by [Bender, 1994]. It involves recording and comparing the phases of two-way signals received from two spacecraft that are within the beamwidth of a single ground antenna. Originally, this method was proposed for a network of landers to study the internal structure of the Moon ([Bender, 1994]; [Gregnanin et al., 2012]) and Mars ([Gregnanin et al., 2012]). The SBI technique offers valuable insights into the relative motion of angularly close spacecraft and it retains information on the differential range between the two spacecraft, relative to the ground antenna.

As said before, the fundamental concept of SBI involves simultaneously observing two spacecraft from a single ground antenna and comparing the phases of the received carrier signals. This process typically utilizes a two-way configuration, enabling highly precise differential phase measurements with millimeter-level accuracy ([Gregnanin et al., 2012]). These observables provide line-of-sight information by measuring the difference in round-trip light time (i.e., range) between each spacecraft and the common ground station, thereby indirectly revealing the relative motion between the two spacecraft. The key advantage of this method is the extreme accuracy of phase measurements due to the cancellation of common noise sources, such as instabilities in the frequency standard and antenna deformations, and significantly reducing media noise, with only small residual effects caused by the non-zero angular difference (in azimuth and elevation) of the signal paths. Although SBI has never been implemented or demonstrated (because of the need to uplink two coherent carriers or CDMA signals from the same deep space antenna), the generation of the SBI observables is expected to be straightforward in a MSPA tracking configuration such as the one considered for ATLAS.

SBI is achieved by comparing (i.e., differencing) the phases of two-way signals, which requires defining three distinct epochs: the time t_1 when the ground station (g/s) transmits the signal, the time t_2 when the signal is received and re-transmitted by spacecraft (s/c) A and B (with a turnaround frequency ratio M), and finally, the time t_3 when the signal from both spacecraft is received at the same ground station. To develop the SBI observable model, the first step is writing the two-way phase for a spacecraft (either A or B), beginning from the reception time t_3 and tracing back the signal path, as illustrated in Fig. 3.1.

At any given time t_3, the measured phase difference between the two received signals, which arises from differences in their respective t_1, contains information about the spacecraft state vectors. The received phase from both spacecraft at a common reception time are compared, noting that the epochs $t_1(t_3)$ and $t_2(t_3)$ differ for spacecraft A and B and are functions of t_3. These epochs are computed within the OD software by solving the light-time problem for a given reception epoch for each spacecraft. Similarly, the values for uplink (up) and downlink (dn) travel times are expressed as functions of the considered reception time, denoted as $\tau_{up}(t_3)$ and $\tau_{dn}(t_3)$. For simplicity, this explicit dependence will be omitted in the following

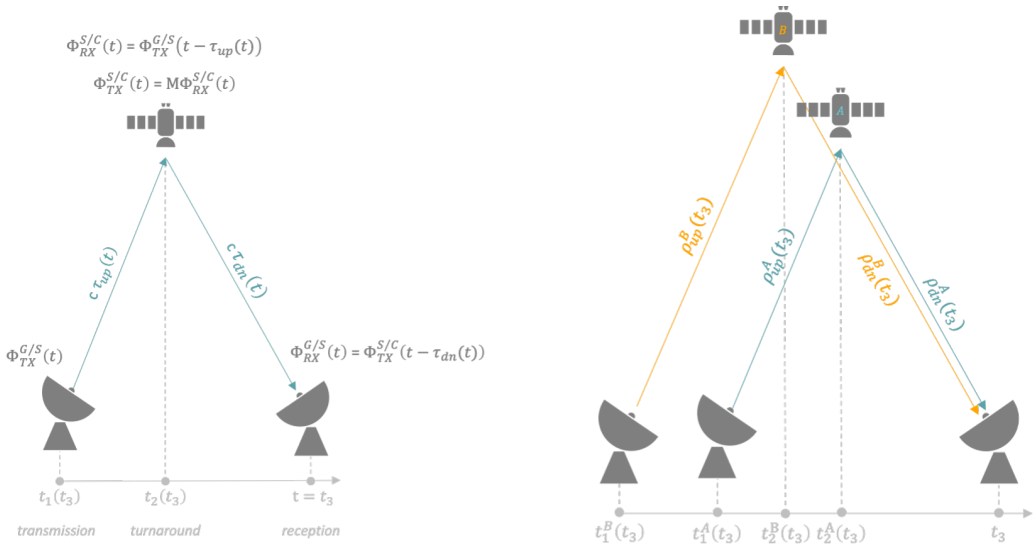

Figure 3.1. Phase definition in a two-way radio link for a single spacecraft (left) and SBI observable procedure for two generic spacecraft A and B (right) [Sesta et al., 2024].

notation, mentioning it only when necessary for clarity. Referring to the signal path in Fig. 3.1, the instantaneous phase of the received signal at the ground station for a reception time t_3 can generally be expressed as:

$$\Phi_{RX}^{G/S}(t_3) = M\Phi_{RX}^{S/C}(t_3 - \tau_{dn}) = M\Phi_{TX}^{G/S}(t_3 - \tau_{up} - \tau_{dn}) \tag{3.23}$$

This indicates that the received phase corresponds to the phase transmitted one round-trip light time earlier, multiplied by a constant, known as the turnaround ratio M. If the ground station transmits at a nominal frequency ω_0 with an initial phase offset ϕ_0, it is possible to rewrite Eq. 3.23 as:

$$\Phi_{RX}^{G/S} = M\omega_0(t_3 - \tau_{up} - \tau_{dn}) + M\phi_0 = M(\omega_0 t_3 + \phi_0 + \Psi_{RTLT}) \tag{3.24}$$

The phase term $\Psi_{RTLT} = -\omega_0(\tau_{up} + \tau_{dn})$ represents a quantity that changes very slowly over time due to the relative motion between the spacecraft and the ground station. This term corresponds to the spacecraft's two-way range ρ_{RTLT} at the t_3 time tag: $\Psi_{RTLT}(t_3) = -\omega_0/c(\rho_{up} + \rho_{dn}) = -k\rho_{RTLT}(t_3)$, where k is the wave vector and c is the speed of light. Eq. 3.24 models the total unwrapped phase value from the beginning of the tracking pass. The measured phase is obtained at the ground station using a PLL that reconstructs the unwrapped phase (averaged over a count time), with an ambiguity corresponding to the integer number of cycles since the initial spacecraft position relative to the ground station. This ambiguity must be accounted for in the model; otherwise, a bias would appear in the OD residuals when the spacecraft trajectories are corrected. Therefore, Eq. 3.24 must be modified as follows:

$$\Phi_{RX}^{G/S} = M(\omega_0 t_3 + \phi_0 + \Psi_{RTLT}) - 2\pi N \tag{3.25}$$

where N is an integer, different for spacecraft A and B.

Fig. 3.1 illustrates the concept behind the SBI observable $y_{SBI}(t_3)$, which is defined as the difference between Eq. 3.25 calculated for spacecraft A and B. Assuming both spacecraft use the same transponding ratio (enabled by CDMA) and that the ground station transmits at the same nominal frequency (enabled by CDM-M), it can be expressed as follows:

$$y_{SBI}(t_3) = M(\Psi^B_{RTLT} - \Psi_{RTLT}A) - 2\pi(N^B - N^A) = \frac{M\omega_0}{c}(\rho^A_{RTLT} - \rho^B_{RTLT}) - 2\pi K \tag{3.26}$$

where K represents the unknown difference in the integer number of cycles between spacecraft A and B at the start of the tracking pass. Consequently, the SBI observable corresponds to the difference in the two-way range between spacecraft A and B, scaled by a constant factor. However, it includes an initial ambiguity that must be resolved within the formulation of the OD problem. Essentially, a phase bias, which remains constant throughout each tracking pass, needs to be added to the list of parameters to be determined.

3.4 Error sources for radiometric observables

Numerous sources of error impact the measurements collected by ground equipment. The accuracy of the parameters estimated through the Precise Orbit Determination (POD) fit is directly related to the weight assigned to the observables (see Chapter 4) which depends on their noise levels. The primary noise categories affecting the quality of radiometric data, and consequently the accuracy of the estimation, include instrumental noise, systematic errors, and propagation noise. Instrumental noise refers to random errors introduced by ground-based antenna equipment and onboard transponders. Systematic errors arise from unmodeled or inadequately described effects in the dynamical or observation model, such as unmodeled accelerations, uncertainties in Earth orientation, station locations, or Earth tides. These errors can also result from calibration biases. Propagation noise is caused by random fluctuations in the refractive index of the transmission medium, leading to variations in the signal's velocity and direction, causing phase instability [Asmar et al., 2005]. The main sources of propagation noise include the effects of the Earth's troposphere, as well as the dispersive impact of the Earth's ionosphere.

The effect commonly referred to as tropospheric delay is not solely caused by the troposphere. It involves atmospheric layers ranging from the troposphere to the stratosphere, with the stratosphere contributing only about 20% of the total effect. The propagation delay can be expressed as:

$$\delta\rho = 10^{-6} \int N ds \tag{3.27}$$

where ds is a differential length along the path and N is the refractivity, expressed as:

$$N = (n-1)10^6 = N_d + N_w \tag{3.28}$$

n is the refraction index. The effect is caused by two different components of the refractivity, N_d known as the dry component, and N_w which is the wet component.

The dry component accounts for 90% of the overall effect and assumes that atmospheric gases behave according to the ideal gas law and that the atmosphere is in hydrostatic equilibrium. The wet component, on the other hand, is more challenging to assess due to the variability in partial water vapor pressure, though specialized instruments like water vapor radiometers can help address this issue. A widely used expression for these indices is provided by [Smith and Weintraub, 1953]:

$$\begin{aligned} N_d &= 77.6 \left(\frac{P}{T}\right) \\ N_w &= 3.73 \times 10^5 \frac{\tilde{e}}{T^2} \end{aligned} \tag{3.29}$$

the previous expression is valid for frequencies under about 30 GHz. P, T, and $\tilde{e}$ are respectively the pressure in mbar, the temperature in K, and the partial water vapor pressure expressed in mbar, all evaluated at the surface. This effect depends on the elevation angle of the radio link. To account for this dependence, mapping functions are defined to relate the zenith delay to any other elevation angle. A general description of the tropospheric delay can be expressed as:

$$\Delta\rho_t(El) = \tau_d m_d(El) + \tau_w m_w(El) \tag{3.30}$$

where τ is the delay experienced at the zenith direction, $m(El)$ is the mapping function adopted whose value varies with the elevation angle, and the subscripts d and w refer to the dry and the wet components. The simplest mapping function m is:

$$m(El) = \frac{1}{\sin(El)} \tag{3.31}$$

Other mapping functions are defined based on the signal's spectral region. In optical wavelengths, the troposphere acts as a dispersive medium, so the delay expression depends on the signal's wavelength. However, in radio frequencies, the stratosphere and troposphere are electrically neutral and treated as non-dispersive media. For radio frequencies, more complex and precise mapping functions than Eq. 3.31 are available, such as the Niell model of the tropospheric mapping function ([Niell, 1996]), in which the tropospheric zenith delays are related to delays at arbitrary elevation angles.

Another source of error is the delay caused by the ionosphere. This atmospheric region, located primarily above 80 km altitude, contains charged particles. Fluctuations in the ionosphere's refractive index are influenced by free electrons, with electron concentration increasing with altitude due to stronger solar radiation, peaking around 300 km, then decreasing as atmospheric density drops. The electron density profile also varies with season and time of day. This effect is negligible for optical wavelengths but is dispersive for radio frequencies, meaning the delay depends on the signal's frequency:

$$\delta t = \frac{\alpha_e}{f^2} \tag{3.32}$$

where α_e is proportional to the Total Electron Content (TEC). The term α_e is positive for group delays (e.g., pseudorange) and negative for carrier phase. Since

the ionospheric delay is dependent on frequency, transmission of signals at different frequencies allows removal of the ionosphere, at least to an acceptable level for orbit determination applications. Although the linear combination increases the measurement noise compared to the single-frequency measurement, the removal of the systematic effects associated with ionospheric variability is essential for high-accuracy applications.

A commonly used figure of merit for assessing the stability of a frequency standard is the Allan Deviation (ADEV) ([Barnes et al., 1971]). It is a time-domain metric that measures fluctuations in fractional frequency as a function of the averaging time (τ_{av}). The observables are represented by a time series, y(t), of fractional Doppler fluctuations, which reflect the frequency difference between the received and reference signals, divided by the nominal frequency of the Doppler link:

$$y(t) = \frac{\Delta f(t)}{f_0} \tag{3.33}$$

The Allan variance can be computed as:

$$\sigma_y^2 = \frac{1}{2}\left\langle (\bar{y}_{i+1} - \bar{y}_i)^2 \right\rangle \tag{3.34}$$

Where:

$$\bar{y}(t, \tau_{av}) = \frac{1}{\tau_{av}} \int_t^{t+\tau_{av}} y(t')dt' \tag{3.35}$$

The error budget for Doppler/range-rate observables can be defined in terms of this parameter (see Chapter 6 for the detailed error budget).

The ranging jitter due to thermal noise (random noise) depends on the available SNR (see Table 2.1), both in the uplink and downlink. For a SS ranging system the jitter is obtained from the following expression of the chip tracking loop [Holmes, 1982]:

$$\frac{\sigma}{T_C} \cong \sqrt{\frac{N_0 B_L}{2S}\left(1 + \frac{2N_0 B_P}{S}\right)} = \sqrt{\left[\frac{N_0}{S}\right]_{eq} \frac{B_L}{2}} \tag{3.36}$$

In chip, where:

$$\left[\frac{S}{N_0}\right]_{eq} = \frac{\frac{S}{N_0}}{1 + \frac{2N_0 B_P}{S}} \tag{3.37}$$

Is the equivalent signal power over noise power spectral density, T_C is the chip length ($T_C = \frac{1}{chiprate}$), B_P is the pre-detection bandwidth and B_L is the loop bandwidth. B_P is conservatively taken as 8 times the symbol rate. For the K-band link we assumed B_P = 28.8 kHz (assuming a TC bit rate of 1.8 kbps and a code rate of r=1/2) for the onboard transponder and B_P = 11.2 kHz (assuming a TM bit rate of 1.4 kbps and a code rate of r=1/2) for on-ground receiver. In the downlink, the pre-detection bandwidth is derived from the TM symbol rate in one branch, which is assumed half of the total symbol rate derived from the link budget.

When the onboard loop bandwidth is much narrower than the on-ground loop bandwidth, the uplink and downlink jitters sum up as the square root of their

squared values. Under this unlikely condition, the overall end-to-end (E2E) one-way ranging jitter can be computed as [CCSDS, 2014]:

$$(\sigma_{rng})_{E2E} \approx \frac{c}{2} T_C \sqrt{\left(\frac{\sigma}{T_C}\right)_U^2 + \left(\frac{\sigma}{T_C}\right)_D^2} \tag{3.38}$$

in meter where c is the speed of the light. In a more realistic case, when the onboard loop bandwidth is much larger than the on-ground one, the overall end-to-end one-way ranging jitter is independent of the onboard loop bandwidth and can be written as [CCSDS, 2014]:

$$(\sigma_{rng})_{E2E} = \frac{c}{2} T_C \sqrt{\frac{B_{L_D}}{2}\left(\left[\frac{N_0}{S}\right]_{eq_U} + \left[\frac{N_0}{S}\right]_{eq_D}\right)} \tag{3.39}$$

in meter, where the onboard transponder has a loop bandwidth of $B_{L_U} = 5$ Hz, while for the ground receiver a value of $B_{L_D} = 0.1$ Hz (considering ranging observables every 10 seconds, see Chapter 6).

Differently from range-rate measurements, range observables are generally affected by a significant bias, generated both by the ground and onboard electronics and antennas. Both can be calibrated with very good accuracy using dedicated hardware. The transponder group delay can be monitored with accuracies of <0.1 ns utilizing a calibration circuit embedded in the unit. This is the case of the BepiColombo KaT, a Ka-band transponder that is part of the MORE scientific investigation ([Cappuccio et al., 2020]). The two-way group delay of the ground electronics can also be calibrated with similar accuracies, as demonstrated by [Cappuccio et al., 2020] for ESA's deep space station DSA-3 (Malargüe, Argentina).

3.4.1 Media Calibration System

The media propagation effect is one of the most relevant for the radiometric measurement error. Thus, a key factor for the observation model is the media calibration system adopted for the ground observations. It can provide either a model or measurements of the ionospheric and tropospheric (both dry and wet) path delays, with the latter approach (actual calibrations) typically outperforming empirical models, at the price of an increased system complexity and larger costs. Different types of media calibration systems exist in support of orbit determination of interplanetary spacecraft and can be equally used for the LRNS constellation.

Given that the ionospheric path delay is a dispersive noise contribution, it can be greatly reduced by adopting a higher frequency as seen in Eq. 3.32. At the K-band the peak of the zenith path delay is ~4 cm and approximately 10 times larger at the X-band. To calibrate the ionospheric delay it is possible to use either the ionospheric empirical model or GNSS dual frequency calibrations data mapped along the line-of-sight between the ground antenna and each tracked spacecraft. In the first category belongs the NeQuick software available online, which is a simple and real-time modeling tool to get about 50% of the overall ionospheric path delay calibrated, working

better at mid-latitudes [European GNSS (Galileo) Open Service, 2016]. Much better ionospheric calibrations can be obtained with GNSS dual frequency data. These are typically provided by third parties as the Jet Propulsion Laboratory (JPL), but ESA has worked to get an in-house internal service provided by the ESOC (European Space Operations Centre) Navigation Support Office ([Feltens et al., 2018]). In any case, for a LRNS constellation, what matters is the availability of these calibrations in almost near real-time. The adaption of the already existing software codes (needed to process GNSS dual frequency data for their ingestion in the orbit determination process of interplanetary probes) to speed up the availability of ionosphere calibration products looks like an easy task. However, in the early phase of LRNS deployment, one can anyhow rely on NeQuick software.

A similar discussion can be made about the troposphere path delay calibration. The dry troposphere at each tracking site can be suitably calibrated using weather data (P, T) and modeling the atmosphere assuming a hydrostatic equilibrium as shown in Eq. 3.29. A high-precision barometer has been successfully used to produce dry tropospheric path delays during the Cassini radio science experiment along the zenithal direction. The zenith path delay can then be mapped along the line-of-sight using a simple mapping law such as Eq. 3.31, providing excellent approximation for elevations >20°-30°. The wet troposphere path delay is more difficult to calibrate, mostly due to the high variability of the water vapor density along the line-of-sight (due to its poor mixing). The better way to calibrate the wet path delay is to use precision WVR. Alternatively, delta-tropospheric calibrations (differences from delays computed with (P, T) measurements) can be made available via GNSS calibration data ([Feltens et al., 2018]). For the tropospheric media calibrations service, the ESA Navigation Support Office produces once per day a file containing 48h time series of Zenith Wet Delays (ZWDs) and Zenith Total Delays (ZTDs) for each ESTRACK site, with a time interval of 24h. In this case, the current code needs to be modified to produce output metadata every 2 hours (instead of 24 hours).

Due to the different levels of complexity to get accurate media calibrations (both in terms of costs and implementation effort), it is possible to follow three sequential steps for the implementation of the LRSN media calibration system:

1. Phase 1 - Initial deployment:
    - Ionosphere: Nequick model.
    - Troposphere: Barometer calibration for the dry troposphere.
2. Phase 2 - First Augmentation:
    - Ionosphere: GNSS dual frequency data.
    - Troposphere: GNSS delta-tropospheric calibration.
3. Phase 3 - Second Augmentation:
    - Ionosphere: GNSS dual frequency data.
    - Troposphere: use of Water Vapor Radiometer (WVR).

These three phases correspond to a different calibration level and accuracy for radiometric data, implying a different error budget for each phase. This different noise level has been considered for numerical simulations and results are reported in Chapter 6 for phases 2 and 3. It is important to note that for each phase of the media calibration system, it is assumed that the previous one is fully operational. This means that, for example, the barometer is needed and used both in Phase 2 and Phase 3.

The baseline configuration used for the architecture (see Chapter 6) is the Phase 3 implementation, thus the simulated calibration errors are:

- The tropospheric path delay, considering 95% calibration of the wet component obtained with a dedicated WVR. It allows an accuracy of up to 0.5 cm ([Linfield et al., 1996]; [Lasagni Manghi et al., 2023]).
- The ionospheric path delay, considering a 90% calibration achieved with GNSS dual frequency data ([Liu et al., 2021]).

The media calibration errors have been added to the simulated range measurements as systematic effects (see Chapter 6 for details on the numerical simulation setup).

3.5 Time Transfer and Clock Desynchronization

In the proposed architecture, the ground stations and the spacecraft perform ground-to-space time transfer by exploiting the two-way radio link. An important difference between terrestrial GNSS and the proposed LRNS is the nearly complete independence between the OD process and the clock offset estimation, attained thanks to the use of two-way observables that do not involve by any means the onboard clocks. The time synchronization accuracy across the lunar constellation relies on three main factors:

- The ground-to-space time transfer accuracy.
- The accuracy and stability of the on-board satellite clocks.
- The desynchronization between different ground stations of the tracking network.

The potentially detrimental effect of the desynchronization between different ground stations is largely mitigated by the MSPA approach. Indeed, a single ground station (or multiple stations of the same complex employing the same frequency standard) can simultaneously perform ground-to-space time transfer with the whole constellation, keeping the time of the constellation internally consistent. In addition, the clocks at different ground stations can be synchronized by exchanging clock offset information immediately before and after a station handover. Accuracies in the range of 1-5 ns can be attained in the ground-to-space time transfer with the method proposed below. If clock comparisons are carried out immediately before and immediately after the handover by the two intervening ground stations and the constellation spacecraft, also the clocks of the ground network can be internally

synchronized to the same level of accuracy (1-5 ns). Binding the network time to TAI/UTC can be performed via GNSS clock synchronization. Note however that the user positioning in the lunar environment requires only a good synchronization within the constellation, which is not necessarily a synchronization to TAI/UTC.

Any assessment of time desynchronization between distant clocks requires comparing their readings at the same coordinate time. This process involves applying relativistic transformations between proper time τ (the actual time recorded by each clock) and coordinate time t. However, for simplicity, we present only a basic formulation, assuming that proper and coordinate times are effectively equivalent. In practice, relativistic transformations are applied as deterministic corrections in operational scenarios. With this simplification, the primary consideration is the finite speed of light.

In the proposed architecture, the ground-to-space time transfer can be performed with two methods. The first approach is the TT-Async-Mode, which relies on two-way asynchronous/non-coherent links between an Earth tracking station and each satellite of the lunar constellation. This method needs the onboard transponder working in non-coherent mode and it is conceptually similar to the Two-Way Satellite Time and Frequency Transfer (TWSTFT) ([Howe et al., 1989]) used on Earth in the generation of the UTC timescale ([Arias et al., 2011]). On Earth TWSTFT, a geostationary satellite is indeed used as a relay for the signals to close the links (in both directions) between two distant ground stations without reciprocal visibility. However, when the two terminals are mutually visible, it is possible to directly establish a two-way asynchronous link. The main advantage of this TT method is that it can be considered virtually immune from orbital errors, at the cost of interrupting radiometric data acquisition (need to switch the operation mode of the onboard transponder from coherent to non-coherent) and a different signal structure with respect to the coherent mode one. Thus, the number of clock comparisons performed during a tracking pass is limited.

Fig. 3.2 shows the world lines and the scheme of the asynchronous links along with all the relevant epochs involved in the desynchronization measurement. The station ground clock generates a signal at t_1, transmitted from the antenna at t_2 after a certain delay in the TX channel mostly due to cables and electronics. The signal reaches the satellite antenna at t_3. Then, after another delay in the satellite RX channel, the signal reaches the satellite time comparator at t_4, where the on-board desynchronization observable $\Delta\tau^B = t_5 - t_4$ is produced. In this scheme the epoch at which the onboard SGU, clocked by the EUFR, generates a signal for downlink transmission is t_5, as in the uplink process. This signal is transmitted from the on-board antenna at t_6 after a delay in the spacecraft TX channel, and it reaches the ground antenna at t_7, where, after another delay in the ground RX channel, it reaches the station time comparator at t_8. Finally, the observable quantity $\Delta\tau^A = t_1 - t_8$ is generated at the Earth tracking station.

Given the formulation by [Duchayne et al., 2009] and [Delva et al., 2012], combining the observables from the two asynchronous links, the desynchronization

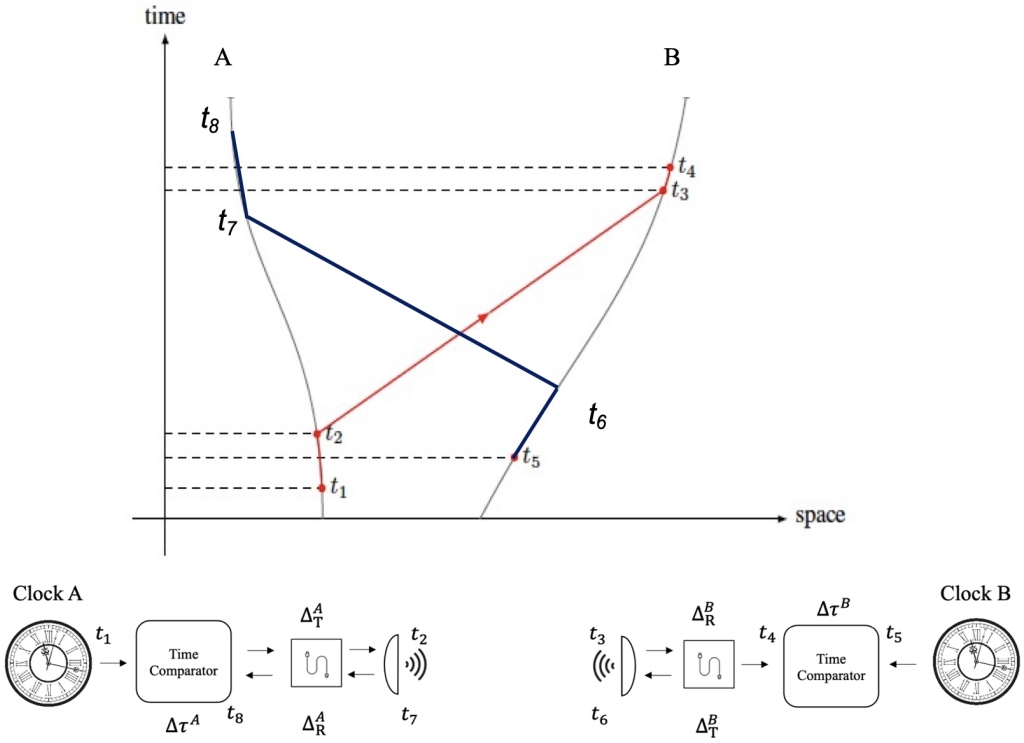

Figure 3.2. World lines and scheme for the asynchronous time transfer method. The two observable quantities, measured onboard and on ground, are $\Delta\tau^B = t_5 - t_4$ and $\Delta\tau^A = t_1 - t_8$. The other terms represent onboard and ground delays ($\Delta_T^A, \Delta_R^A, \Delta_T^B, \Delta_R^B$) in the TX and RX path, and propagation delays (T_{23}, T_{67}) [Iess et al., 2023].

equation between the two clocks may be written as:

$$t^B(t) - t^A(t) = -\frac{1}{2}\left[(\Delta\tau^B - \Delta\tau^A) + (\Delta_T^A - \Delta_R^A) + (\Delta_R^B - \Delta_T^B) + (T_{23} - T_{67})\right] \tag{3.40}$$

where $\Delta_T^A, \Delta_R^A, \Delta_T^B, \Delta_R^B$ represent the onboard and ground delays in the TX and RX path, while T_{23}, T_{67} are the propagation delays, according to Fig. 3.2.

This shows that the clock desynchronization between ground and space clocks is the average of the two measured observables corrected for the differential delays due to electronic and propagation delays (including geometric path delays and additional effects due to Earth's troposphere and ionosphere). If $t_1 \approx t_5$, the path reciprocity ensures most errors cancel out in the differentiation procedure, including errors in OD.

The overall uncertainty of the time transfer with the TWSTFT method can be preliminarily assumed below the 1 ns level (and likely ~0.3 ns could be achieved if periodic calibrations take place at both segments), in line with the uncertainties reported in Circular T by the Bureau International des Poids et Mesures (BIPM) [BIPM, 2023].

The second method is the TT-Sync-Mode. This method relies on two-way coherent measurements, and it aims at exploiting the performances of PN ([CCSDS, 2022])/SS ([CCSDS, 2011]) ranging systems for time transfer purposes. In any two-way coherent radiometric measurement, solving for the light-time solution requires to consider three distinct epochs:

- t_1: the epoch of signal transmission from ground.
- t_2: the epoch of signal reception onboard the satellite.
- t_3: the epoch of signal reception on ground.

The onboard clock provides direct access to measurements of t_2 while the ground clock measures t_3. Then, both $\hat{t}_1$ and $\hat{t}_2$ can be computed by solving backward for the light-time solution ([Moyer, 2003]) through the OD process, where the two-way ranging observable represents a measure of the Round-Trip Light Time (RTLT $= t_3 - t_1$). In this scenario, the ground-to-space clock desynchronization can be therefore inferred as:

$$desync(t) = \hat{t}_2(t) - t_2(t) = \left(t_3(t) - \frac{\rho_{23}(t)}{c}\right) - t_2(t) \tag{3.41}$$

where $\hat{t}_2(t)$ is the onboard time derived from the OD solution through ρ_{23}/c, the one-way light time solution (in the downlink leg), while $t_2(t)$ are the readings of the onboard clock.

In both approaches, the onboard time-stamping operations are triggered by a Code Epochs (CE) signal, activated by a specific chip of the SS signal. Then the recorded epoch is sent to the ground in the telemetry stream. On the ground, a similar time-tagging operation is triggered by the received code epoch signal and the epoch t_3 provides $\hat{t}_2$ through the OD process, while telemetry data about t_2

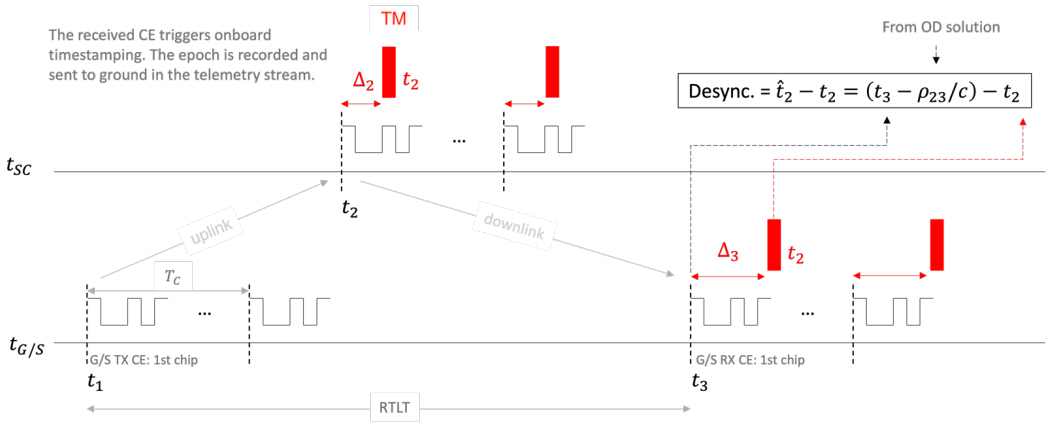

Figure 3.3. Scheme for time synchronization with the two-way coherent approach. The delays Δ_2 and Δ_3 are introduced by data encoding/decoding in the Telemetry (TM) transmission and may even exceed the code repetition period [Iess et al., 2024].

is downloaded by the satellite. Finally, these data are compared to obtain the desynchronization. Fig. 3.3 shows the scheme for the two-way coherent time transfer method.

The proposed Truncated Maximum Length (TML) sequence for the uplink spread spectrum code has a length of $256 \cdot (2^{10} - 1) = 261888$ chips ([Iess et al., 2023]). With a chip rate of approximately 24 Mcps, the chip duration ~41.6 ns, and the code repetition period is T_{TML}~10.9 ms. When using this method, two key factors must be carefully considered: the ability to resolve code ambiguity and the accurate association of the CE arrival with the time-stamping operation performed by the clock assembly. Data encoding and transmission through the telemetry channel may introduce a delay Δ_2 (same can happen when the telemetry data are downloaded by the satellite Δ_3) which, depending on the encoding method used, could even cause to exceed T_{TML}. However, this delay is largely deterministic and can be easily corrected during post-processing. Consequently, it is possible to reconstruct the delays associated with encoding and transmission, ensuring that each TML frame on the ground can be unambiguously associated with the relevant CE.

The main advantage of this novel technique ([Iess et al., 2023]; [Iess et al., 2024]) is that it can be performed in parallel with nominal ground tracking operations. The desynchronization accuracy depends on both OD performances along the Line Of Sight (LOS), i.e., accuracy in one-way light time computation and on the precision of the time-stamping operations. The Lunar Orbiter Laser Altimeter (LOLA) laser altimeter of the Lunar Reconnaissance Orbiter has achieved a time-stamping precision of about 0.5 ns ([Bauer et al., 2017]), while numerical simulations show an OD accuracy along the line-of-sight better than 3 cm (see Section 6.7), corresponding to 0.1 ns. Therefore, a conservative estimate of the desynchronization accuracy attainable with this method is at the 1 ns level.

Chapter 4

Orbit Determination Problem

4.1 Fundamentals of Orbit Determination

Every space mission relies on precise knowledge of the spacecraft's trajectory, which is essential for mission operations, such as planning maneuvers and performing the scientific objectives of the mission. Given the state X_0 of a spacecraft at a time t_0, if the dynamical model that defines the differential equations governing its motion is known, it is possible to integrate these equations to obtain the trajectory, namely the spacecraft state at any time. However, in an actual scenario, the spacecraft's initial state is not exactly known. Moreover, not only certain physical constants affecting the motion are known only approximately, but also the forces acting on the spacecraft are approximately modeled. Such errors will cause the actual motion to deviate from the predicted one, so the integrated trajectory will deviate from the real one.

To improve the accuracy of the spacecraft's trajectory, namely the spacecraft state at a time $t > t_0$, the Precise Orbit Determination (POD) process uses radiometric observables to provide a refined estimate of the spacecraft's dynamical state X_i at a given time t_i, i.e., the set of parameters required to predict the future motion of the system [Tapley et al., 2004]. The solve-for list is often extended to include additional dynamic and measurement model parameters to improve prediction accuracy. Ground stations, whose precise locations on Earth are required, collect observables Y_i related to the spacecraft's state through a specific non-linear relation:

$$Y_i = G(X_i, t_i) + \epsilon_i \tag{4.1}$$

where the general state vector X_i is governed by the following differential equations:

$$\dot{X} = F(X, t) \tag{4.2}$$

When the number of measurements m equals the number of components in the unknown state vector n, it might seem appropriate to use an iterative root-finding algorithm, such as the Newton-Raphson method, to solve this non-linear system of equations. However, the problem is underdetermined: the measurements are always subject to random and systematic errors with associated statistical properties, meaning the total unknowns include both the state vector components and the

measurement errors $(n + m)$, while the only available information consists of the m measurements. In typical operational scenarios, the number of measurements significantly exceeds the number of state variables $(n \gg m)$. The purpose of the POD is not to determine the spacecraft's exact motion but to provide the best estimate of the trajectory that most closely aligns with the observational data.

Once a trajectory estimate has been established, the subsequent motion and corresponding observation values can be predicted. In the orbit determination procedure, the process of predicting the state of a vehicle is referred to as "generating an ephemeris". An ephemeris for a space vehicle is a table of its position and velocity components as a function of time. However, the predicted values will deviate from the true values due to the following factors:

1. Errors or inadequacy of the dynamical model.
2. Measurement noise, limiting the accuracies of the observations.
3. Errors in the numerical procedure (including truncation and round-off errors).

As a consequence, the state determination must be repeated. It is virtually impossible to propagate the state of a spacecraft for a very long time without incurring serious discrepancies. The time interval between updates depends on the accuracy of the dynamical model, the quality of the observations, and the needs of the user.

4.2 Linearization Procedure

In the general orbit determination problem, both the dynamics and the measurements involve significant nonlinear relationships:

$$\dot{\boldsymbol{X}} = F(\boldsymbol{X}, t), \quad \boldsymbol{X}(t_k) \equiv \boldsymbol{X}_k \tag{4.3}$$

$$\boldsymbol{Y}_i = G(\boldsymbol{X}_i, t_i) + \epsilon_i; \quad i = 1, \ldots, l \tag{4.4}$$

Where $\boldsymbol{X}_k$ is the unknown n-dimensional state vector at time t_k, and $\boldsymbol{Y}_i$ for $i = 1, ..., l$ is a p-dimensional set of observations that are to be used to obtain a best estimated of the unknown value of $\boldsymbol{X}_k$, i.e. $\hat{\boldsymbol{X}}_k$. In general, $p < n$ and $m = p \times l \gg n$. This formulation of the problem is characterized by:

1. The inability to observe the state directly.
2. Nonlinear relations between the observations and the state.
3. Fewer observations at any epoch than there are state vector components $(p < n)$.
4. Errors in the observations represented by ϵ_i.

The problem of determining the best estimate of the state of a spacecraft, whose initial state is unknown, from observations influenced by random and systematic errors, using a mathematical model that is not exact, is referred to as the problem of state estimation or orbit determination problem (ODP) (see [Tapley et al., 2004]).

If the relations between the state vector and observation vector were linear, then, there are several powerful techniques from the field of linear estimation theory which come to help in the orbit determination problem.

If a reasonable first guess reference trajectory $\boldsymbol{X}^*$ is available, which, in the period of interest, is sufficiently close to the true one $\boldsymbol{X}$, then the true trajectory can be expanded in Taylor's series about the reference one at each point in time. Finally, eliminating higher order terms, the equations end up being expressed in terms of deviations of the state from the first guess reference trajectory $\boldsymbol{X}^*$, obtaining a set of linear differential equations with time-dependent coefficients. Applying the same procedure to the observations' equation, it is possible to obtain a linear relation between the observation deviation and the state deviation. Thus, the OD problem equations become:

$$\dot{\boldsymbol{X}}(t) = F(\boldsymbol{X}, t) = F(\boldsymbol{X}^*, t) + \left[\frac{\partial F(t)}{\partial \boldsymbol{X}(t)}\right]^* [\boldsymbol{X}(t) - \boldsymbol{X}^*(t)] + O_F[\boldsymbol{X}(t) - \boldsymbol{X}^*(t)] \quad (4.5)$$

$$\boldsymbol{Y}_i = G(\boldsymbol{X}_i, t_i) + \epsilon_i = G(\boldsymbol{X}_i^*, t_i) + \left[\frac{\partial G}{\partial \boldsymbol{X}}\right]_i^* [\boldsymbol{X}(t_i) - \boldsymbol{X}^*(t_i)]_i + O_G[\boldsymbol{X}(t_i) - \boldsymbol{X}^*(t_i)] + \epsilon_i \quad (4.6)$$

where $[\ \ ]^*$ indicates that this quantity is computed on the reference trajectory, obtained from the integration of the differential equation of motion of the spacecraft, with initial conditions specified by $\boldsymbol{X}^* t_0$. O_F and O_G indicate the higher order terms in the equations. The deviations can be defined as:

$$\boldsymbol{x}(t) = \boldsymbol{X}(t) - \boldsymbol{X}^*(t) \quad (4.7)$$

$$\boldsymbol{y}_i = \boldsymbol{Y}_i - \boldsymbol{Y}_i^* \quad (4.8)$$

Expressing respectively the deviation between the true trajectory and the reference one, and the difference between the observed observables (e.g., radiometric data acquired at the ground station) and the computed observables, namely the value resulting from computing the observable using Eq. 4.1 with the components of the reference state. Following this reasoning, it is possible to write:

$$\dot{\boldsymbol{x}}(t) = \dot{\boldsymbol{X}}(t) - \dot{\boldsymbol{X}}^*(t) \quad (4.9)$$

Using these deviation definitions, the Eq. 4.5 and Eq. 4.6 can be re-written in a more convenient way neglecting the higher order terms (O_F and O_G):

$$\dot{\boldsymbol{x}}(t) = A(t)\boldsymbol{x}(t) \quad (4.10)$$

$$\boldsymbol{y}_i = \tilde{H}_i \boldsymbol{x}_i + \epsilon_i \quad (i = 1, ..., l) \quad (4.11)$$

Where:

$$A(t) = \left[\frac{\partial F(t)}{\partial \boldsymbol{X}(t)}\right]^* \quad (4.12)$$

$$\tilde{H}_i = \left[\frac{\partial G}{\partial \boldsymbol{X}}\right]_i^* \quad (4.13)$$

Given these relations, the estimation problem that has to be dealt with is now a linear estimation problem, described by a set of linear equations in terms of deviations from a reference trajectory, where:

$$\boldsymbol{x}_i = \boldsymbol{X}(t_i) - \boldsymbol{X}^*(t_i) \tag{4.14}$$

$$\boldsymbol{y}_i = \boldsymbol{Y}_i - G(\boldsymbol{X}_i^*, t_i) \tag{4.15}$$

The solution of the linear system described in Eq. 4.10 can be expressed as:

$$\boldsymbol{x}(t) = \Phi(t, t_k)\boldsymbol{x}_k \tag{4.16}$$

Where $\Phi(t, t_k)$ is the state transition matrix, namely the matrix multiplying the initial state's deviation to provide the state's deviation at any given time. This matrix represents the partial derivatives of the state deviation vector's components with respect to the components of the initial conditions vector:

$$\Phi(t, t_k) = \frac{\partial \boldsymbol{x}(t)}{\partial \boldsymbol{x}_k} \tag{4.17}$$

At this point, it is desirable to use the state transition matrix to express all observations in terms of the state at a single epoch to reduce the number of unknown state vectors from $l \times n$ to n. Using Eq. 4.16, it is possible to express Eq. 4.11 as:

$$\boldsymbol{y}_1 = \tilde{H}_1 \Phi(t_1, t_k)\boldsymbol{x}_k + \epsilon_1 \tag{4.18}$$

$$\boldsymbol{y}_2 = \tilde{H}_2 \Phi(t_2, t_k)\boldsymbol{x}_k + \epsilon_2 \tag{4.19}$$

$$\vdots \tag{4.20}$$

$$\boldsymbol{y}_l = \tilde{H}_l \Phi(t_l, t_k)\boldsymbol{x}_k + \epsilon_l \tag{4.21}$$

now this equation contains $m = p \times l$ observations and only n unknown components of the state. If $\epsilon_i, i = 1, ..., l$ is zero, any linearly independent n of Eq. 4.18 can be used to determine $\boldsymbol{x}_k$.

With these definitions it is possible to describe the statement of the orbit determination problem: given an epoch t_k, the state propagation equations and the observations-state relationships:

$$\boldsymbol{x}(t) = \Phi(t, t_k)\boldsymbol{x}_k \tag{4.22}$$

$$\boldsymbol{y} = H\boldsymbol{x}_k + \boldsymbol{\epsilon} \tag{4.23}$$

find the best estimate of $\boldsymbol{x}_k$. Where:

$$\boldsymbol{y} \equiv \begin{bmatrix} \boldsymbol{y}_1 \\ \vdots \\ \boldsymbol{y}_l \end{bmatrix}; \quad H \equiv \begin{bmatrix} \tilde{H}_1 \Phi(t_1, t_k) \\ \vdots \\ \tilde{H}_l \Phi(t_l, t_k) \end{bmatrix}; \quad \boldsymbol{\epsilon} \equiv \begin{bmatrix} \epsilon_1 \\ \vdots \\ \epsilon_l \end{bmatrix} \tag{4.24}$$

where $\boldsymbol{y}$ is an $m \times 1$ vector, $\boldsymbol{x}_k$ is an $n \times 1$ vector, $\boldsymbol{\epsilon}$ is an $m \times 1$ vector and H is an $m \times n$ mapping matrix, with $m = p \times l$ total number of observations. If p or l is sufficiently large, the essential condition $m > n$ is satisfied. However, the problem of having m equations in $m + n$ unknowns persists. The least squares criterion gives conditions on the m observation errors that allow a solution for the n state variables $\boldsymbol{x}_k$ at the given reference time t_k [Tapley et al., 2004].

4.3 Weighted Least Squares Solution

The least squares method seeks to find the best estimate of $\boldsymbol{x}_k$ by minimizing a cost function, specifically the sum of the squares of the residuals. Here, *residuals* refers to the differences between observed observables and calculated values. The use of the squared residuals ensures that the cost function can only be zero if all residuals are zero; in contrast, using the sum of the residuals alone could lead to a zero value due to the cancellation of positive and negative residuals.

One of the major shortcomings of the simple least square solution is that all observation errors are treated equally. However, it is not negligible that some data could be more accurate than others. Thus it is necessary to adopt a method to weigh observation errors differently when the accuracy of observations varies (e.g., some data could be noisier due to bad weather conditions, or the tracking could be made from two ground stations whose characteristics are different).

To address this limitation, the Weighted Least Squares (WLS) method is used: each observation vector $\boldsymbol{y}_i$ (for $i = 1, ..., l$) is assigned a corresponding weight matrix w_i. Typically, the observation matrices are normalized so that a weight close to one indicates high importance, while a weight of zero implies the observation is neglected. If the observations at different epochs are uncorrelated, the weight matrices are diagonal.

Under these assumptions, given the linear observation-state Eq. 4.23, with weight matrix W, the WLS method's purpose is to find the estimate of $\boldsymbol{x}_k$ capable of minimizing the sum of the squares of the weighted observation errors; hence, the cost function to be minimized is:

$$J(\boldsymbol{x}_k) = \frac{1}{2}\boldsymbol{\epsilon}^T W \boldsymbol{\epsilon} = \sum_{i=1}^{l} \frac{1}{2}\epsilon_i^T w_i \epsilon_i \tag{4.25}$$

using Eq. 4.23 $J(\boldsymbol{x}_k)$ can be expressed as:

$$J(\boldsymbol{x}_k) = \frac{1}{2}(\boldsymbol{y} - H\boldsymbol{x}_k)^T W (\boldsymbol{y} - H\boldsymbol{x}_k) \tag{4.26}$$

A necessary condition for a minimum of $J(\boldsymbol{x}_k)$ is that the first derivative with respect to $\boldsymbol{x}_k$ is zero:

$$\frac{\partial J}{\partial \boldsymbol{x}_k} = 0 = -(\boldsymbol{y} - H\boldsymbol{x}_k)^T W H = -H^T W (\boldsymbol{y} - H\boldsymbol{x}_k) \tag{4.27}$$

This expression can be rearranged to obtain the so-called normal equation:

$$(H^T W H)\boldsymbol{x}_k = H^T W \boldsymbol{y} \tag{4.28}$$

where the matrix $H^T W H = N$ is referred to as the normal matrix. If the normal matrix is positive definite, it will be possible to define its inverse, and in this case, the solution can be expressed:

$$\hat{\boldsymbol{x}}_k = (H^T W H)^{-1} H^T W \boldsymbol{y} \tag{4.29}$$

The matrix $(H^T W H)^{-1} = P_k$ is known as the covariance matrix of the estimation error associated with $\hat{\boldsymbol{x}}_k$ (if $W = R^{-1}$, where R is the observation noise covariance matrix, it is the minimum variance estimate case, see [Tapley et al., 2004]). P_k is an $n \times n$ matrix, which is positive definite, because it is the inversion of a positive definite matrix, and symmetric, as it is easy to see from its definition. The fundamental importance of this matrix is due to:

- The connection between its rank and the parameters' observability: to have the possibility to invert P_k, it has to be $m \geq n$. If all parameters are observable, then P_k is full rank.
- The fact that it is related to the accuracy of the estimate $\hat{\boldsymbol{x}}_k$; in general the larger the magnitude of the elements of the matrix, the less accurate the estimate.

When the WLS filter reaches convergence, the residuals show a normal distribution. The Weighted Least Squares (WLS) correction with a priori information is given by [Tapley et al., 2004]:

$$\hat{\boldsymbol{x}}_k = (H^T W H + \bar{P}_k^{-1})^{-1}(H^T W \boldsymbol{y} + \bar{P}_k^{-1}\bar{\boldsymbol{x}}_k) \tag{4.30}$$

where $\bar{\boldsymbol{x}}_k$ and $\bar{P}_k$ represent respectively the a priori estimate and its associated covariance matrix at the given time t_k.

Chapter 5

Python Interface to GODOT

The numerical simulations performed for this Ph.D. thesis, from the analysis of the ground station visibility to the ODTS (Orbit Determination and Time Synchronization) performance of the architecture and the positioning uncertainty for the MTO (Moon Transfer Orbit), were done using the ESA GODOT software. GODOT is an astrodynamics library for analysis and operations of space missions. GODOT was developed by ESA/ESOC and is used for mission analysis and in-flight operations [ESA, 2022b]. It is a generic, extensible system for practically any space mission.

GODOT is written in `C++` and exposed to `Python` thanks to `pybind11`. During my visiting period at ESA/ESOC I exposed the GODOT observation module from `C++` to `Python`. Moreover, to enable the OD analysis of different mission scenarios among which the LRNS constellation, the Radio Science Laboratory `Python` interface to GODOT was developed. This `Python` package allows to extend the functionalities of GODOT and it can:

- Allow effortless setup of a complete OD environment, i.e., both simulation and estimation phases.
- Provide an accurate model for the spacecraft dynamics.
- Provide a broad range of observable models.
- Save log files to enable further offline processing.

These functionalities allowed by the easy extensibility of the GODOT core software create a user-friendly interface to the software without the need for the users to study in detail the underlying toolkit.

5.1 Package Structure

The `Python` package is called `rsl` (Radio Science Laboratory) and its dependencies and structure are presented in Fig. 5.1, in particular, its modules are the following:

- `config`: in GODOT all the information about a certain mission scenario, such as the spacecraft trajectory, the gravity fields of the planets and their

ephemerides, the reference frames used, are all defined inside two configuration files the so-called `universe` and `trajectory` files (in `yaml` or `json` format). This module extends these configuration dictionaries with useful methods to easily get and set information.

- `trajectory`: adds functionalities that interact with the trajectories. This module allows to:
  - Propagate a state covariance matrix over time.
  - Interfacing with `spiceypy` ([Annex et al., 2020]), write an integrated trajectory into a SPICE kernel ([Acton, 1996]; [Acton et al., 2018]), and then to load it back in estimation for comparison.
- `dynamics`: includes spacecraft dynamical models to be used in GODOT integrator, i.e. Solar Radiation Pressure (SRP) acceleration, stochastic piece-wise constant acceleration, RTN (Radial, Tangential, Normal) empirical acceleration. Moreover, given the shape module (see the next list item), it is possible to include Albedo, Infrared emission, and Thermal Recoil Pressure accelerations without accounting for the complexity of the spacecraft shape.
- `shape`: allows the definition of a complex spacecraft shape, composed of spacecraft shape elements. It includes different spacecraft components (e.g., box, antenna dish, cylinder). Thanks to this module, the SRP computation is performed for each element, accounting for appropriate geometry. As mentioned before, it can be expanded to compute Albedo and Infrared emission accelerations.
- `observables`: provides the definition of observable quantities and the collection of them both for synthetic observed observables and computed observables. The difference between the two lies in whether the computation includes the partial derivatives with respect to the desired parameters or not. It can be easily expanded with additional observable models. Moreover, it is possible to interact with the collection to easily filter out, cut, and match different subsets of observables according to their key characteristics, such as spacecraft and ground station involved, observable type, acquisition epoch, and so on. This feature simplifies radiometric data analysis and handling.
- `batchFilter`: Provide a least-square estimation filter (QR decomposition [Gentleman, 1975]), to be used with the associated computed observable collection presented before. The solution, both the estimate and the associated covariance can be printed and saved to a file for more processing.
- `show`: includes different plotting capabilities, namely 2D/3D trajectory representation, satellite ground track, ground station - spacecraft elevation, and residual visualization.
- `calibrations`: allows to handle media calibration contribution for different ground stations and targets. Given a certain set of media calibration data, it allows to compute the tropospheric wet and dry and the ionospheric path

delay. It is associated with a mapping function to evaluate the path delay along a certain station-spacecraft direction (as explained in Chapter 3). This module allows us to take media calibration information and convert it into a suitable GODOT object to be used in the observable computation.

- `converters`: allows to read, handle, and convert different file formats to the respective `Python` object handled by the package. In particular, this module is capable of:
  - Read TRK-2-23 media calibration files [Machuzak et al., 2008] to be used for data analysis and to be converted into dedicated media object (input of the `calibrations` module).
  - Process ESTRACK TTCP (Tracking Telemetry and Command Processor [BAE Systems, 2023]) tracking data (e.g., Doppler and Range measurements at the ground station) and convert them in a collection of observed observables (`observables` module) to be used in the OD estimation process by the batch filter (`batchFilter` module).
  - Interfacing with `spiceypy`, read SPICE attitude kernel (`ck`) and select the desired base and target reference frame to create the reference frame attitude in a usable GODOT format.

  The functionalities of this module are fundamental to utilize GODOT with actual radiometric observables for flying spacecraft, as shown in [Cappuccio et al., 2024]. Indeed, the usage of actual radiometric data (generated and read in TTCP format) required the knowledge of the ground station media calibration that allow to compensate the media effect of the collected data. Moreover, the knowledge of the spacecraft attitude allows us to improve the dynamical model of the satellite, i.e. computation of non-gravitational acceleration such as SRP.

- `utils`: provides a set of utility functions for the user's common tasks and supports other user-defined functionalities.

- `units`: enables unit support when defining new physical quantities. The module simply converts input numbers to SI (International System) units.

This `Python` package has been developed and deployed with CI/CD integration on GitLab to autonomously perform the testing and deployment of the package and the associate documentation to be easily installed by the users once GODOT has been installed. However, it is not publicly available yet.

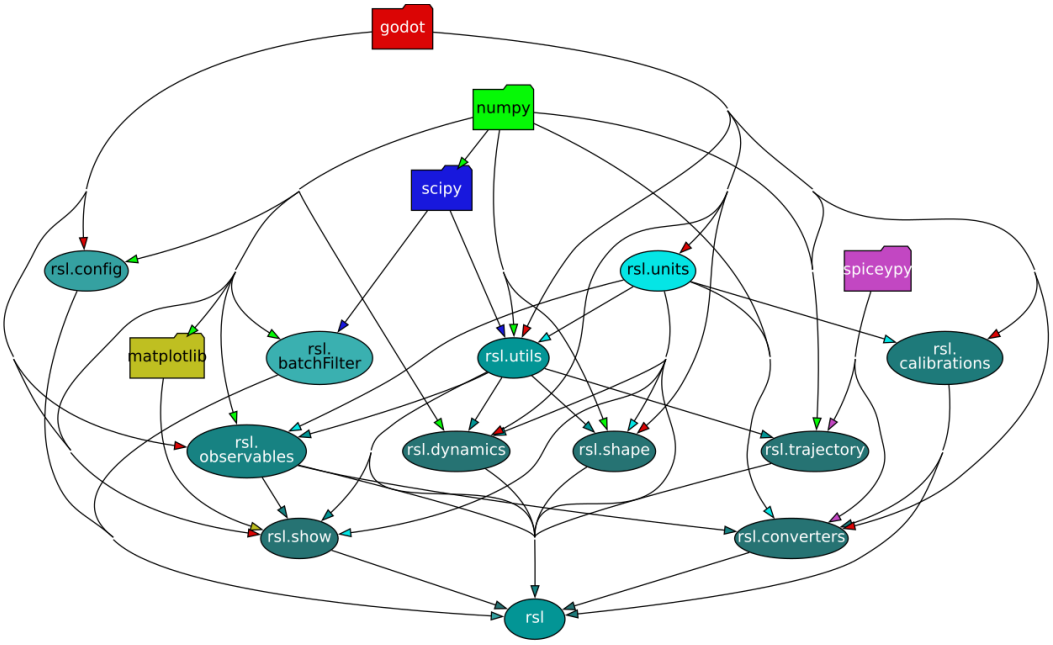

Figure 5.1. `rsl` `Python` package structure and external dependencies

Chapter 6

LRNS Baseline Architecture Performance

The numerical simulations of the LRNS (Lunar Radio Navigation System) are based on generating synthetic data, namely range, Doppler, and SBI (Same Beam Interferometry) observables. To compute the simulated observable a realistic setup has been built, see Table 6.1, described in detail in the following paragraphs. Then a simulated trajectory (reference trajectory) is propagated according to the selected orbital parameters for the LRNS constellation (see Section 6.1.1). The dynamical model used to obtain the reference trajectory is based on several adjustable parameters (see Section 6.2). Using an observation model, the observed observables are generated from the propagated reference trajectories.

These measurements also contain noise whose statistical properties are those expected according to the link budget presented in Chapter 2 (see Section 6.3). The synthetic observables are processed following a standard OD (Orbit Determination) procedure, namely a propagated trajectory obtained from perturbed initial conditions and dynamical model parameters, to simulate unknown accelerations and mismodeling in the spacecraft dynamics. This trajectory (different from the 'true' one) yields the expected value of the observables (computed observables). The estimated parameters are corrected using the iterative procedure outlined in Chapter 4, to minimize a cost function (the weighted sum of squares of the residuals). Once the parameters have been estimated, it is possible to integrate the estimated trajectory and propagate it for an additional day, after the end of the observation arc, to study the ephemerides aging, see Section 6.6 for the details. Then using the reconstructed orbit it is possible to estimate the time synchronization contribution (see Section 6.5) and evaluate the SISE according to Eq. 1.3 and Eq. 1.4. Finally, the performance of the LRNS architecture is determined thanks to a Monte Carlo analysis, presented in Section 6.6, to take into account different possible scenarios and obtain more reliable results for the expected accuracy for the future lunar user.

The proposed MSPA (Multiple Spacecraft Per Aperture) architecture relies on two-way coherent observations. By this, the performances of the OD process and the evolution of the orbital error contribution to the SISE (Signal-In-Space Error) are almost completely decoupled from the behavior and performances of the clocks

onboard the satellites of the LRNS constellation. The nearly complete decoupling of the orbit determination and time transfer problem is a key distinctive element of the proposed architecture. All the numerical simulations presented in this work have been carried out with the orbit determination software GODOT, developed by ESA [ESA, 2022b], enhanced with the additional Python module presented in Chapter 5.

Table 6.1. Main assumptions for the LRNS baseline architecture numerical simulation setup

Dynamical model			
Gravity	Monopole for Sun, Earth, the Moon and Solar System planets		
	Spherical harmonics for Earth and the Moon		
Solar Radiation Pressure	Spacecraft shape typical of small satellites (see Section 6.3)		
Observation model			
Ground Stations	ESTRACK sites (Cebreros, Malargüe, New Norcia)		
Observation Arc Duration	4 days tracking window (shifted for the Monte Carlo Analysis, see Section 6)		
Observations	*Doppler*	*Range*	*SBI*
Noise (see Section 6.3)	~0.45 mHz (~0.005 mm/s)	~33 cm	~1.30 mm
Count Time	60 s	10 s	60 s

6.1 Constellation Geometry

6.1.1 Space Segment

In the initial deployment phase, the proposed lunar constellation is composed of 4 satellites on different ELFO orbits, with the orbital parameter reported in Table 6.2, in line with the ones used for the Moonlight project [Melman et al., 2022]. These highly elliptical orbits allow the coverage of the southern polar region of the Moon for a long time (similar to the Molniya orbits used by GLONASS, the Russian satellite navigation system), as shown in Fig. 6.1, which is the principal zone for the future lunar exploration mission. Furthermore, the orbital parameters are selected to achieve a stable ('frozen') orbit with respect to third-body perturbations from the Earth. This approach minimizes propellant consumption for station-keeping maneuvers to maintain the desired trajectory efficiently.

The relative distance and angle between each pair of satellites are reported in Fig. 6.2 and Fig. 6.3 given that these values are fundamental for the SBI error budget as explained in Section 3.3 and shown in Section 6.3. Moreover, Fig. 6.4 shows the relative angle of the four spacecraft with respect to the centroid of the constellations seen from Earth. This quantity assumes particular relevance in a MSPA architecture, as the one proposed, given that it allows sizing of the ground antenna dimension to

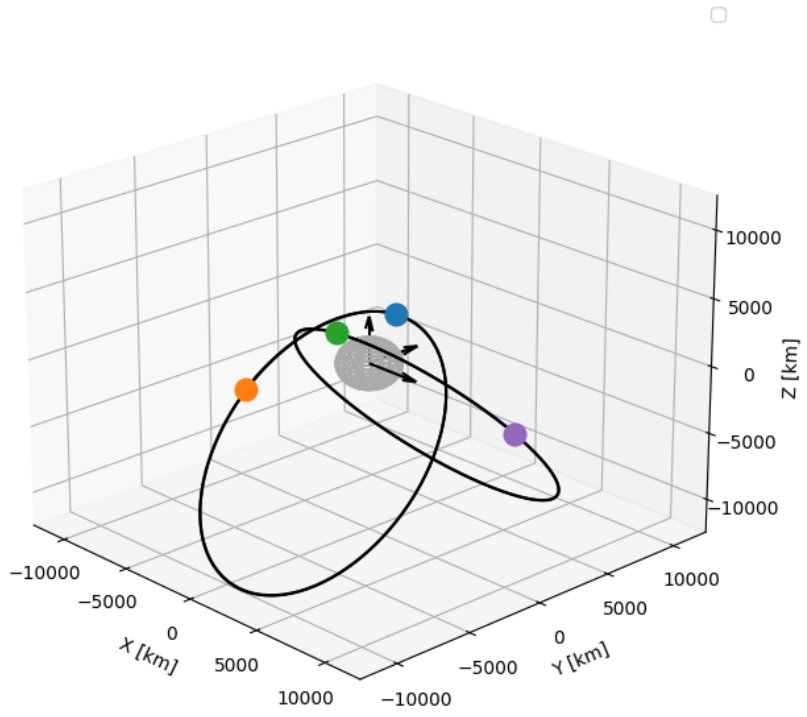

Figure 6.1. Orbital geometry at reference epoch for the LRNS constellation in a Moon-centered inertial reference frame (axes indicated by black arrows). The colored points are the four spacecraft: 1 in blue, 2 in orange, 3 in green, and 4 in purple.

Table 6.2. ELFO Keplerian parameters of LRNS satellites defined in the Moon-fixed frame as defined by the IAU [Archinal et al., 2011], at the initial epoch. The four satellites are located on two different orbital planes, at different true anomalies.

Orbital Parameter (Moon-fixed IAU frame)	ELFO constellation
Semimajor axis	9750.73 km
Eccentricity	0.6383
Pericenter	3526.84 km
Apocenter	15974.62 km
Orbital period	24 h
Inclination	52.12° | 55.20°
Right Ascension of the Ascending Node (RAAN)	354.89° | 184.35°
Argument of pericenter	98.10° | 82.21°
True anomaly	0° | 118° | 0° | 123.42°
Initial epoch	01-June-2026 00:00 TDB

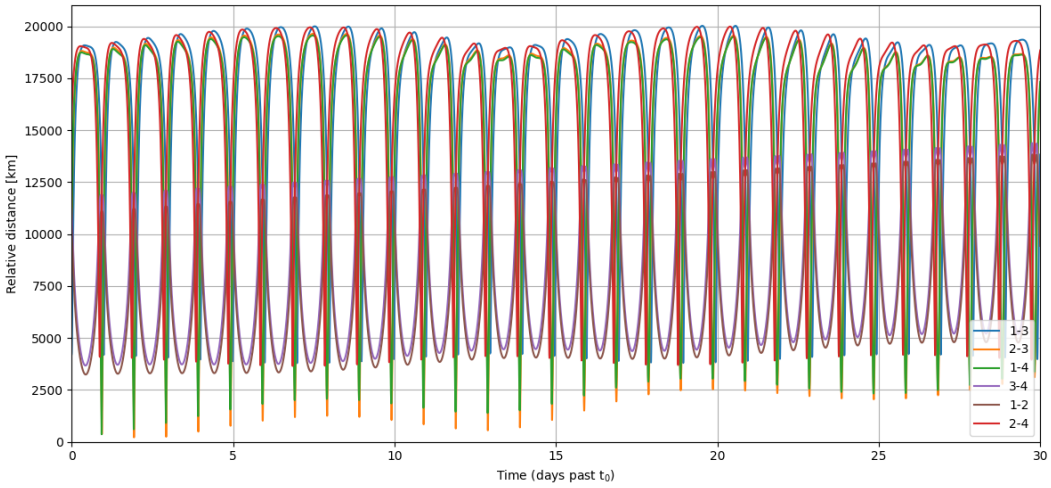

Figure 6.2. Relative distance between pairs of satellites, for the ELFO constellation.

enable the simultaneous tracking of all the satellites from the ground stations.

6.1.2 Ground Segment

Concerning the ground segment, as said in Chapter 2, the small antenna dishes are located close to ESTRACK stations, namely Cebreros (Spain), New Norcia (Australia), and Malargüe (Argentina). The primary rationale behind choosing these three tracking sites is the utilization of pre-existing infrastructure, even though their distribution across the Earth's surface is suboptimal and cannot ensure uninterrupted constellation visibility at a minimum elevation of 15°. The maximum visibility gap spans approximately ~6 hours. This is visible in Fig. 6.5, which shows the constellation visibility over 30 days, to cover entirely the Earth-Moon relative geometry evolution. An additional fourth station located, for example, at Manua Kea (Hawaii) would fill the large longitude gap (about 151°) between Malargüe and New Norcia, enabling continuous tracking as shown in Fig. 6.6. However, Fig. 6.6

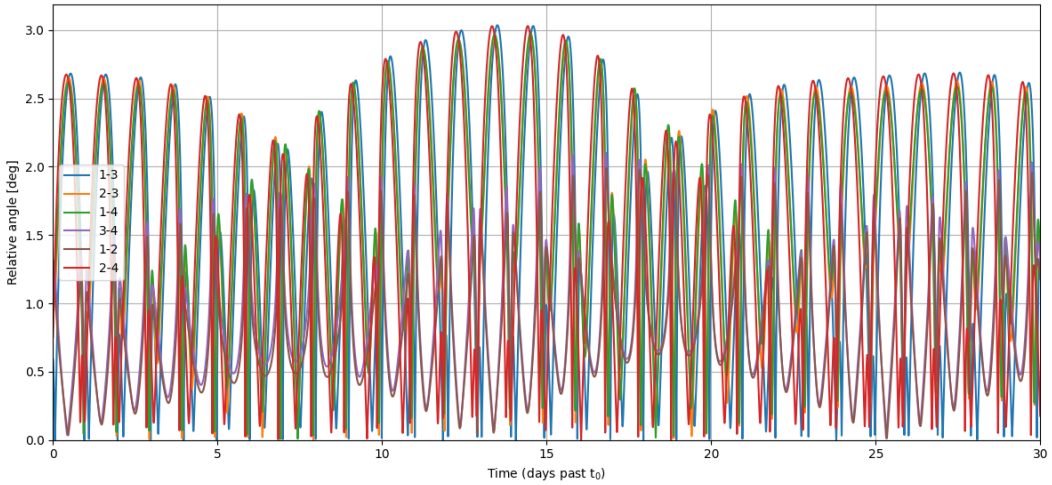

Figure 6.3. Angular separation, as seen from Earth, between satellite pairs, for the ELFO constellation. The HPBW of the antennas is ~3.6 deg. 3 dB pointing losses are included in the link budget, see Section 2.3.

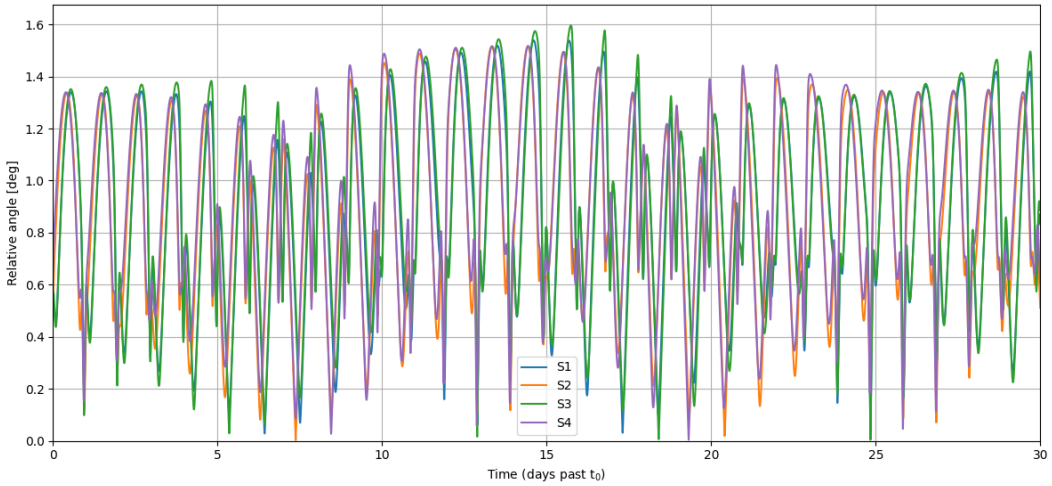

Figure 6.4. Relative angle of the spacecraft with respect to centroid of the ELFO constellation, as seen from the Earth. The HPBW of the antennas is ~3.6 deg. 3 dB pointing losses are included in the link budget, see Section 2.3.

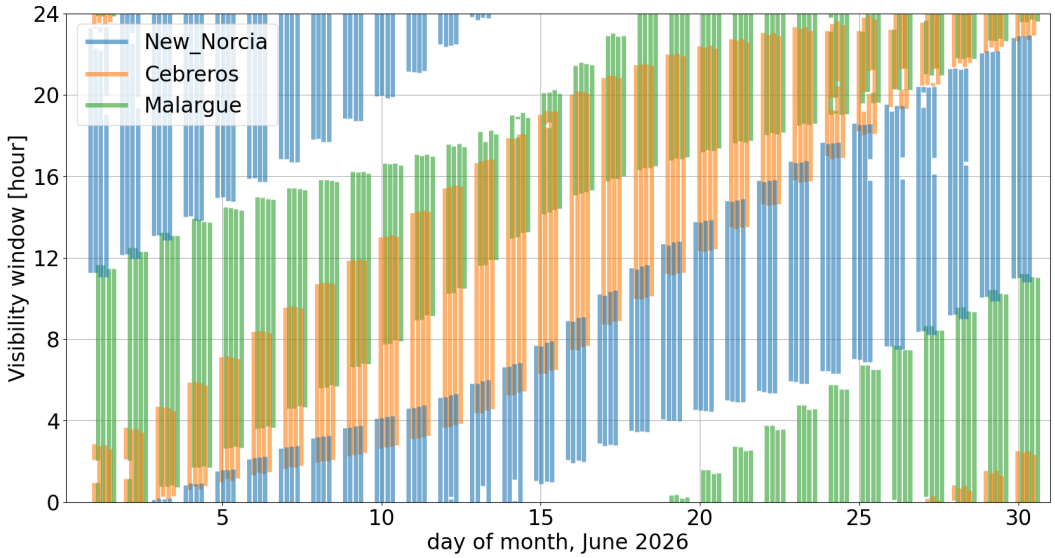

Figure 6.5. Ground station visibility of the LRNS constellation from each of the three ESTRACK sites for a 30-day period (June 2026) with minimum elevation 15° and taking into account the Moon occultations. For each day the 4 light-colored bars represent the visibility for the different satellites of the constellation from each ground station (according to the color). The visibility windows are expressed as hours after midnight, UTC, each day.

still shows short gaps (~1 hour) in the plot, they are related to the Moon occultation of the LRNS constellation.
A change in the station locations while preserving their number and relative longitude would not modify substantially the orbit determination results, since the visibility pattern (thus the amount and the data acquisition times) remains largely unchanged. The visibility and observation elevation among ground stations will vary slightly throughout the year, depending on their location in the northern or southern hemisphere and the Moon's position relative to the ecliptic plane. For simplicity, assuming the Moon lies on the ecliptic plane, ground stations in the northern hemisphere will observe the LRNS at higher elevations during the summer months and lower elevations during the winter. This trend is reversed for ground stations in the southern hemisphere. Occasionally a spacecraft may enter simultaneously in the Field Of View (FOV) of two ground stations. However, each spacecraft can establish a single 2-way radio link at a time, so the observables are established from the ground station having the highest elevation.

6.2 Dynamical Model

The dynamical model of the spacecraft, which is used in the first step of the numerical simulation to generate a reference trajectory, may be perturbed in the estimation phase to mimic the mismodeling of poorly known quantities, as occurring in a realistic orbit determination process. The dynamical model of the spacecraft in the simulation phase includes:

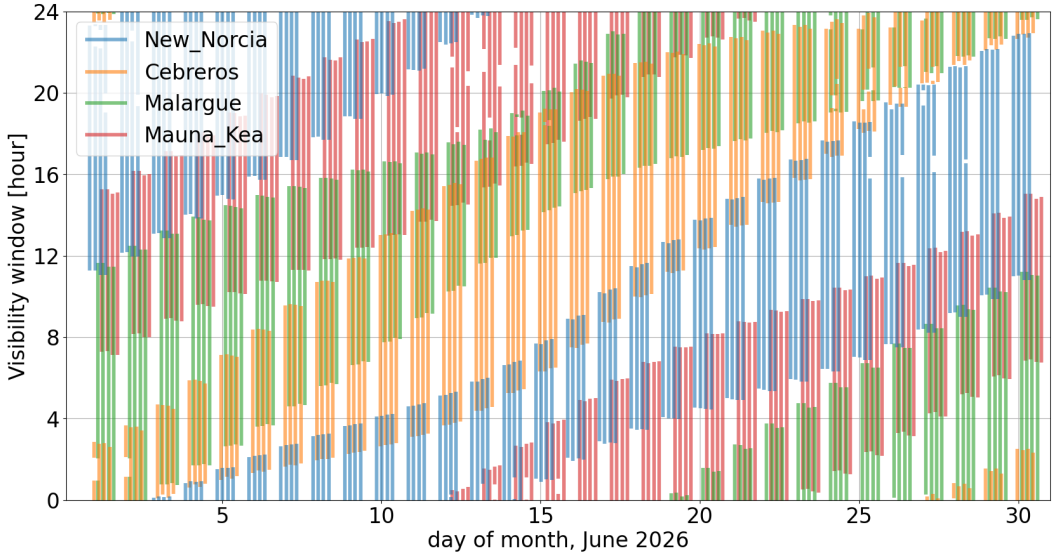

Figure 6.6. Ground station visibility of the LRNS constellation from each of the three ESTRACK sites plus the Mauna Kea station for a 30-day period (June 2026) with minimum elevation 15° and taking into account the Moon occultations. For each day the 4 light-colored bars represent the visibility for the different satellites of the constellation from each ground station (according to the color). The visibility windows are expressed as hours after midnight, UTC, each day.

- The gravitational monopole accelerations due to the Sun, Earth, the Moon, and Solar System planets.
- The spherical harmonics coefficients of the Moon, up to degree and order 120 [Lemoine et al., 2014].
- The spherical harmonics coefficients of the Earth, up to degree and order 12 [Lemoine et al., 2019].
- The non-gravitational acceleration due to the SRP acting on the satellites.

The relative magnitude of the considered accelerations has large variability, for example, at the orbit pericenter, the Moon gravitational monopole contributes for 3.9×10^{-1} m/s^2, the degree 20 lunar spherical harmonics acceleration is about 2.3×10^{-11} m/s^2 and the solar radiation pressure acceleration is about 4×10^{-8} m/s^2. The uncertainties in the gravity fields of the Earth and the Moon are too small to have a significant impact on the LRNS dynamics. Other sources of non-gravitational accelerations, such as the lunar and terrestrial albedo and their infrared emission, as well as the spacecraft anisotropic thermal emission, have not been included in the model due to their small magnitude when compared to the SRP modeling accuracy derived from realistic assumptions. However, the simulations implicitly consider the impact of incorrect modeling of these accelerations on the final covariance matrix. This is done by including random accelerations in the list of estimated model parameters (see later).

A spacecraft shape is required to model the non-gravitational accelerations. In the absence of a consolidated design of the satellites, it is reasonable to assume typical values for the smallsat class, both in terms of mass and volume. Moreover, each satellite may be represented as two plates and a sphere, similar to a box-wing model used for the Galileo satellites [Bury et al., 2019]. The first plate models solar arrays (total area of 1.5 m^2), pointed toward the Sun, the second plate represents the antenna dish (area of 0.1 m^2) constantly pointed toward the Earth, and the sphere (radius of ~0.34 m) models the satellite bus. A solar panel with an area of 1.5 m^2 could in principle generate an onboard power of 515 W (25% efficiency), largely sufficient to cope with power requirements during normal operations. The estimated power needed due to the radio frequency system is about 90 W (also including the transponder and the clock). The hypothesized solar panel area provides a substantial margin for the power consumption of other subsystems. Therefore, the spacecraft shape used for calculating the SRP acceleration is a reasonable assumption for this mission scenario. The thermo-optical properties of these elements have been chosen to match the ones of the Galileo satellites bow-wing formulation [Li et al., 2019]. The mass of each spacecraft has been set to 230 kg, thus producing an area-over-mass ratio of ~0.0085 m^2/kg, corresponding to an average solar radiation pressure acceleration of about 4×10^{-8} m/s^2. This area-to-mass ratio is roughly 2.5 times smaller than for the Galileo satellites.

In any OD process, inaccuracies of the dynamical model due to missing or poorly modeled accelerations unavoidably introduce biases in the estimated model parameters [Bury et al., 2020]. For example, it is difficult to accurately model the SRP acceleration action on the spacecraft (generally, the errors are larger than 2% of the central value, see [Park et al., 2012]). Therefore, we have assumed a mismodeling of the SRP acceleration of about 5%. To simulate a realistic OD process, the first-guess trajectory adopted in the estimation phase should differ from the one used to generate the synthetic data, reflecting inaccuracies in the dynamical model. To this aim, we generated the first-guess trajectories considering a 5% error in the SRP acceleration (it corresponds to an error of about 2.0×10^{-9} m/s^2). In particular, this difference in the SRP acceleration was obtained with a mismodeling in the spacecraft shape, namely a 7% in the satellite bus area and a 50% in the antenna area. In the estimation step, empirical accelerations are included in the dynamical model, to be estimated to compensate for the erroneous representation of the SRP. Although different formulations can be used, for this analysis an empirical piecewise-constant accelerations model was adopted. The three components of this acceleration in the International Celestial Reference Frame (ICRF) with an update-time of 4 hours are estimated, for a total of 18 estimated parameters for each satellite orbit (24 hours orbital period).

In the early phase of the project, additional simulations were conducted using another set of empirical accelerations in the RTN frame, described by the following expression for the acceleration along each axis:

$$a_i = p_i + c_i \cos\theta + s_i \sin\theta \tag{6.1}$$

where p, c and s are the parameters to be estimated and θ is the spacecraft true anomaly. The RTN toward the Moon is defined with the R-axis pointing from the

Moon toward the spacecraft, the N-axis is along the orbit normal (parallel to $r \times v$ where r and v are respectively the spacecraft position and velocity vector), and the T-axis completes the right-handed frame (velocity is generally mostly along this axis). The two acceleration formulations yield similar results, using a comparable number of parameters to be estimated for both setups (e.g., empirical coefficients per orbit). This outcome is reasonable, given that only non-gravitational acceleration included in the simulation is the SRP. Note that the effects of albedo and thermal infrared emission from the Moon, that are not considered in this analysis (negligible with respect to the SRP), might be better represented by a different empirical acceleration formulation.

6.3 Observables Error Budget

As said before, the synthetic measurements also contain noise and to simulate realistic noise statistical properties an error budget for the radio-tracking observables has been done. The error budget for the proposed architecture is computed based on the recent data collected by BepiColombo, reported in [Iess et al., 2021], and on the findings in the ESA study "ASTRA: Interdisciplinary study on enhancement of end-to-end Accuracy for Spacecraft Tracking Techniques" [Iess et al., 2014].

Each error source in the Doppler error budget has spectral properties and a different relationship with the integration time. The ADEV of each intervening noise source scales differently from, e.g., 1000 s to 60 s. By this, it is not possible to derive the total Root Sum Square (RSS) value at 60 s integration time from the one at 1000 s. Often the ADEV at 1000 s is used to show a Doppler error budget. Since in the numerical simulations an integration time of 60 s is used, Table 6.3 shows the Doppler error budget computed at 60 s integration time for the K-band radiolink. It is possible to convert the error in term of ADEV σ_y into a frequency error Δf (or a range-rate error $\dot{\rho}$) to be used by the OD software for the estimation:

$$\sigma_y \approx \left(\frac{\Delta f}{f}\right)_{RMS} \approx \frac{2\dot{\rho}}{c} \tag{6.2}$$

The end-to-end range error budget is reported in Table 6.4 and computed using the equations and considerations reported in Section 3.4 together with the link budget presented in Table 2.1. It is important to note that even if the use of a WVR would improve the tropospheric calibration of the zenith wet delay to 0.5 cm [Linfield et al., 1996], it has been assumed a more conservative value of 2 cm, in line with the accuracies provided by the radiometer installed at DSA-3 [Lasagni Manghi et al., 2023] and en elevation angle of 30°. Moreover, Table 6.4 shows relatively large values for the station location (3 cm), since VLBI observations cannot be used with small dishes. This value is compatible with positioning via laser metrology from a fiducial point ([Estler et al., 2002]), assuming that the proposed antenna is located close to a large deep space tracking antenna included in the VLBI network or a GNSS station.

Table 6.3. Doppler error budget for the ATLAS architecture, expressed as ADEV at 60 s integration time [Iess et al., 2023].

Allan Deviation @ 60 s, two-way coherent, K-band	
Media	
Ionosphere	3.2×10^{-15}
Troposphere	1.2×10^{-14}
RSS Media	$\mathbf{1.2 \times 10^{-14}}$
Space Segment	
Transponder	6.0×10^{-15}
RFDA	1.6×10^{-15}
Steerable antenna assembly	8.6×10^{-15}
Spacecraft Structure	4.0×10^{-15}
RSS Space Segment	$\mathbf{1.1 \times 10^{-14}}$
Ground Segment	
H-maser frequency standard	4.1×10^{-15}
Ground station electronic	1.7×10^{-15}
Ground antenna (mechanical)	8.0×10^{-18}
Station location	6.4×10^{-17}
Earth Orientation Parameters (EOP)	3.2×10^{-17}
Earth solid tides	4.0×10^{-17}
RSS Ground Segment	$\mathbf{4.4 \times 10^{-15}}$
Total RSS	$\mathbf{1.7 \times 10^{-14}}$ **(~0.45 mHz)**

Moreover, in this analysis, the media calibration errors have been added to the simulated ranging measurements as systematic effects. In the synthetic data simulation, for each tracking pass we approximated the tropospheric zenith path delay with a parabola whose coefficients are extracted randomly to obtain a zenith path delay profile ranging between 3.0 – 5.1 cm, in line with [Iess et al., 2014]. Then, we mapped the zenith path delay according to the station elevation at each observation epoch and added the uncalibrated percentage of the path delay to the synthetic measurements. Instead, the computation of the ionospheric path delay was performed with the NeQuick ionospheric model [European GNSS (Galileo) Open Service, 2016], and, similarly, the uncalibrated portion was added to the simulated range data.

[Gregnanin et al., 2012] evaluated the performance of a Ka-band system capable of measuring the differential phase between two landers with an accuracy of less than a fraction of a wavelength ($\leq$ 0.1 mm). The configuration considered in the cited paper involved a network of three lunar landers spaced approximately 1000 km apart. Since the primary errors in SBI are, to a first approximation, proportional to the angular separation between the spacecraft, the expected accuracy for the proposed constellation is lower (given that the maximum distance is around 20000 km looking at Fig. 6.2), around 1.3 mm, primarily due to incomplete cancellation of tropospheric and ionospheric path delays.

The SBI error budget is evaluated with the same assumptions used for the link

Table 6.4. Range error budget for the ATLAS architecture, expressed as distance error sampled at 10 s [Iess et al., 2023].

Range (1-σ two-way @ 10 s) K-band (24 Mcps)	
Contribution	Value (cm)
Media	
Ionosphere (bias+scintillation)	0.4
Troposphere (bias)	2.0
RSS Media	**2.0**
Space and Ground Segment	
Station group delay calibration	3.0
Spacecraft group delay calibration	1.5
Station location	3.0
Earth Solid Tides	1.8
EOP	3.0
RSS GS+SC	**5.7**
Jitter	**32.7**
Total RSS	**33.3**

budget (see Section 2.3). Note that for SBI, the end-to-end error budget is strongly dependent on the angular separation since residual media and platform errors, the two dominant error sources, are proportional to this quantity. The reported values for media errors are an order of magnitude evaluation based on the same approach used for the Delta-Differential One-way Ranging (DDOR) error budget in [CCSDS, 2021], where average values for GNSS tropospheric and ionospheric calibrations are assumed. Should a WVR be available at the ground site, the residual tropospheric path delay can be significantly reduced. Note that media errors depend also on the tracking elevation (an average pass elevation of 30° is assumed in Table 6.5).

6.4 Batch Filter Parameters

In the orbit determination process, the orbital filter processes the observables and estimates the model parameters, for this analysis the estimated parameters for each OD arc (see Section 6.7) are reported in Table 6.6. It is important to note that the empirical acceleration parameters have a nominal value equal to zero, thus their estimated value should compensate for the introduced dynamical mismodeling. These accelerations are assumed to be uncorrelated between each 4-hour batch interval (white-noise statistics). Their a priori uncertainty, based on the expected mismodeling of the spacecraft dynamics, is 2.0×10^{-9} m/s^2. The choice of a larger a priori value than the expected mismodeling will result in inflated covariances for the estimated parameters but will not significantly impact the estimation errors, which are the primary performance metrics analyzed in this study. The estimation error, and more importantly the SISE, are primarily influenced by the dynamical mismodeling (see Section 6.7) rather than by the a priori uncertainty of the empirical accelerations used in the orbit determination process.

Table 6.5. SBI budget for the ATLAS architecture with 60 s integration time [Iess et al., 2023].

Same Beam Interferometry (SBI)		
Quantity	**Unit**	**Value**
Carrier frequency	GHz	26.25
Max distance between satellites	km	20000
Integration time	s	60
Instrument phase ripple	deg	0.5
Station location uncertainty	cm	3.0
EOP uncertainty	cm	3.0
Elevation (average)	deg	30
Tropospheric path delay (residual @ zenith, mostly wet)	cm	1.0
Angular separation (average)	deg	2.0
Ionospheric path delay (residual @ zenith, K-band)	cm	0.4
Error Budget		
Space and Ground Electronics	**mm**	**0.06**
Thermal noise	mm	0.04
Frequency stability	mm	0.04
Differential phase shift (on-board electronics)	mm	0.02
Residual Media	**mm**	**1.30**
Troposphere	mm	1.21
Ionosphere	mm	0.48
Platform	**mm**	**0.03**
Station location	mm	0.02
EOP	mm	0.02
RSS Total	**mm**	**1.30**

The biases in the observables' model for range and SBI have been included to account for errors in the calibration of the station and the transponder delay and to mitigate the uncalibrated media effects. In the proposed architecture, given the small dimension of the dish, the geometric delay of the antenna is smaller and more stable with respect to deep-space antennas. Regarding the station and transponder delay calibration system, the same approach used for BepiColombo is straightforward to be implemented for LRNS as well. Thus, it is possible to estimate a single (and constant) range bias for each station (including transponder delay, station delay, and uncalibrated media contributions) during each observation arc, in agreement with the results of BepiColombo's MORE radio science experiment ([Cappuccio et al., 2020]; [Iess et al., 2021]). While it's theoretically possible to resolve the phase ambiguity in the SBI observables (see Section 3.3), achieving a post-processing absolute phase measurement to within about 10% of a wavelength, a more conservative approach is used. This involves including a constant phase bias for each tracking pass and station in the list of parameters to be estimated.

Table 6.6 reports an elevated a priori uncertainty for the spacecraft position and velocity, which means that the spacecraft state at the beginning of each OD process

is unconstrained to its a priori value. Thus, it is a pessimistic scenario: no a priori information on the LRNS constellation is known (see Section 6.7).

Table 6.6. List of the parameters estimated by the OD filter (for each OD arc) with the associated a priori values and uncertainty.

Parameter	A priori value	A priori uncertainty
Spacecraft position	Reference trajectory perturbed by 1 m (1-σ) on each component	1 km
Spacecraft velocity	Reference trajectory perturbed by 0.1 mm/s (1-σ) on each component	1 km/s
Solar arrays total area	1.5 m^2	0.1 m^2
Empirical accelerations parameters	0.0 m/s^2	2×10^{-9} m/s^2
Range biases (one per station)	0.0 m	10 m
SBI biases (one per spacecraft pair, per tracking pass, per station)	0.0 m	100 m

6.5 Time Transfer Contribution

The clock error contribution to the overall SISE is due to the instability of the onboard clocks and the inherent inaccuracies of the time synchronization process. The entity of the former is based on the spectral characteristics of the candidate clocks: USO (Ultra Stable Oscillator), MiniRAFS (miniaturized Rubidium Atomic Frequency Standard), and RAFS. A stochastic noise realization of each clock is simulated based on the discretized ADEV using the method of [Timmer and Koenig, 1995].

The desynchronization contribution is simulated and evaluated for the two-way synchronous time transfer as this method is expected to provide more pessimistic results than using the TWSTFT, which is not affected by the OD contribution. During the satellite tracking window, desynchronization measurements (see Eq. 3.41) can be collected from two-way coherent ranging measurements. These observables can be used to extrapolate the clock behavior, under the following relation:

$$\Delta\tau_s = \sum_{i=0}^{D} \Delta\tau_s^{(i)} (\tau - \tau_0)^i \tag{6.3}$$

for D=2, this represents the combination of a clock offset $\Delta\tau^{(0)}$, a clock drift $\Delta\tau^{(1)}$ (frequency bias) and a clock quadratic term $\Delta\tau^{(2)}$ (a frequency drift). These clock correction parameters shall be included in the navigation message transmitted to the end user. For present purposes, one is interested in calculating the SISE clock

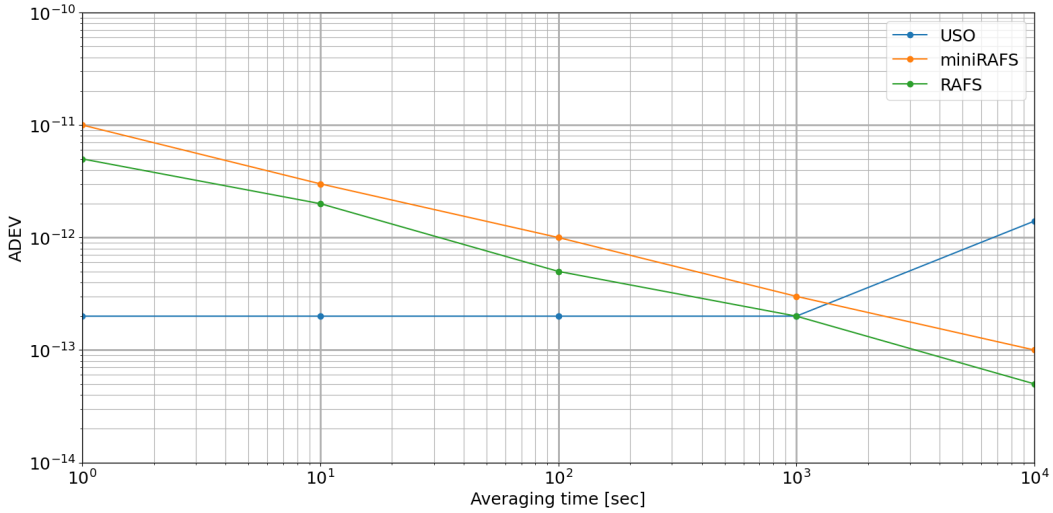

Figure 6.7. Frequency stability in term of ADEV of the USO (blue line), miniRAFS (orange line) and RAFS (green line) as a function of the averaging time. The ADEV at different timescales is a typical value for each technology [Sesta et al., 2024].

contribution, given by the fit obtained by $\Delta\tau_s$ applied during the propagation interval. The onboard clock model fit is performed over a data set acquired during a single tracking pass (up to 6 hours max) so that the overall process can be repeated three times per day.

The frequency stability of the proposed clocks for the LRNS constellation is reported in Fig. 6.7 as a function of the averaging time ([Orolia, 2023b], [Orolia, 2023a], [Accubeat, 2021]). Notice that the USO has both the best short-term stability and the worst long-term stability among the three considered clocks (the rubidium clock curves are detrended, meaning that they are obtained by removing a linear frequency drift and a constant bias).

6.6 Monte Carlo Analysis Setup

To assert the performance of the LRNS constellation reliably, the orbit reconstruction has been analyzed under different relative geometries, namely multiple scenarios covering a full sidereal month. A Monte Carlo-like analysis has been performed by changing the constellation's initial condition epoch by 1 hour, recursively over 30 days, resulting in a total of 577 cases, as shown in Fig. 6.8. In each arc, for the OD process, the observables are collected over a 4-day tracking window to estimate the filter parameters, this duration has been selected to optimize the computation time for this analysis while obtaining a good trajectory reconstruction, meaning that the additional data does not improve the arc OD in a significant way. However, during the operational orbit determination cycle once the constellation has been deployed, it is possible to utilize more data to slightly improve the OD accuracy, selecting an OD arc duration feasible with the time constraints of the nominal operations.

Figure 6.8. Sequence of arcs for the Monte Carlo simulation [Iess et al., 2023].

This Monte Carlo-like analysis allows us to determine the LRNS performances across most possible configurations. Therefore, lunar users can refer to these results to predict their PNT accuracy during the mission. Estimating the spacecraft trajectories in each OD arc is performed without a priori information from the previous one, meaning that the covariance matrix is not propagated between different arcs. Since the navigation message broadcasted from the LRNS will have a certain update time, the trajectories are integrated for an additional day, without collecting further data, to assess how the accuracy of the satellites' ephemerides uploaded in the navigation message decreases over time, to validate the system architecture, establish its performance, and suggest a reliable update frequency of the navigation message.

The Monte Carlo-like analysis varying the initial reference epoch allows us to assess the OD performances under different conditions:

- Orbit orientation with respect to the Earth, varying between an edge-on and a face-on configuration. In the first configuration (orbit edge-on), the spacecraft moves with respect to the Earth, and the information content in range and Doppler measurements is large. In the last case (orbit face-on), the orbital plane is nearly perpendicular to the tracking direction, thus range and Doppler measurements are less effective in providing information on the spacecraft dynamics.
- Station visibility and tracking periods, as shown in Fig. 6.5.
- Earth-Moon-Sun relative geometry (i.e., a different relative attitude).
- True anomaly along the orbit.
- True anomaly at the last data point in the arc (i.e., the point where ephemerides aging starts).

Summarizing what was said in the previous section of this chapter, for each OD arc to obtain realistic OD performance, the following factors are considered:

- The random part of the noise (Gaussian noise from error budget considerations) is added to the simulated observables (see Section 6.3).
- The range observables also account for systematic media calibration errors (see Section 6.3).

- A mismodeling in the spacecraft dynamics between simulation and estimation is introduced (different spacecraft shape for the SRP acceleration, namely a mismodeling in the antenna dish area and the bus radius, see Section 6.2).
- The initial state of the satellite at each arc is affected by a randomly varying perturbation (Gaussian, with a standard deviation of 1 m in position and 0.1 mm/s in velocity), thus for each 1-hour shift, a different realization of the error is produced. The initial mistakes of the state vector components are small as they are assumed to be derived from the full orbital fit of the previous arc (see Section 6.4). Indeed, the initial perturbations are compatible with the estimated position and velocity errors in the reconstructed OD arc (see Section 6.7.1).

6.7 Results

6.7.1 Single Arc Orbit Determination Performance

The numerical simulations show that on average it is possible to obtain an accurate state determination, below 1 m for position and below 0.1 mm/s for velocity, processing a 4-day batch of data. Fig. 6.9 shows the root sum of square (RSS) of state uncertainties and orbital errors, both in terms of position and velocity, for the four satellites, in a randomly selected arc. These trends are consistent over the analyzed period, mainly because the most notable variations are driven by the pericenter and apocenter passes, given the high eccentricity of the orbits, rather than by other geometrical conditions. The RSS of positioning accuracies are defined as:

$$RSS_p = \sqrt{\sigma_x^2 + \sigma_y^2 + \sigma_z^2} \tag{6.4}$$

$$RSS_v = \sqrt{\sigma_{v_x}^2 + \sigma_{v_y}^2 + \sigma_{v_z}^2} \tag{6.5}$$

where σ_x, σ_y and σ_z are the formal uncertainties of the spacecraft positions over time in the ICRF, centered around the Moon and σ_{v_x}, σ_{v_y} and σ_{v_z} are the formal uncertainties of the spacecraft velocities over time in the same reference frame. The orbital error is the difference between the reference and the estimated satellite orbit:

$$\delta p = \sqrt{(x - \bar{x})^2 + (y - \bar{y})^2 + (z - \bar{z})^2} \tag{6.6}$$

$$\delta v = \sqrt{(v_x - \bar{v}_x)^2 + (v_y - \bar{v}_y)^2 + (v_z - \bar{v}_z)^2} \tag{6.7}$$

where x, y, z, v_x, v_y and v_z are the position and velocity coordinates estimated after the OD process, while the bar indicates true (i.e., simulated) values. The vertical solid black line represents the last data point epoch. The curve values after the black line show the ephemerides aging, which is, as previously stated, one of the main components of the SISE. The periodic behavior both in the uncertainty and the estimation error in the satellite position (left side plot) are closely related to the very eccentric orbit, with minimum values attained during periselene passes, where the orbit determination is more accurate given the much stronger gravity gradient. In Fig. 6.9, it is possible to note that in some intervals the errors are larger than

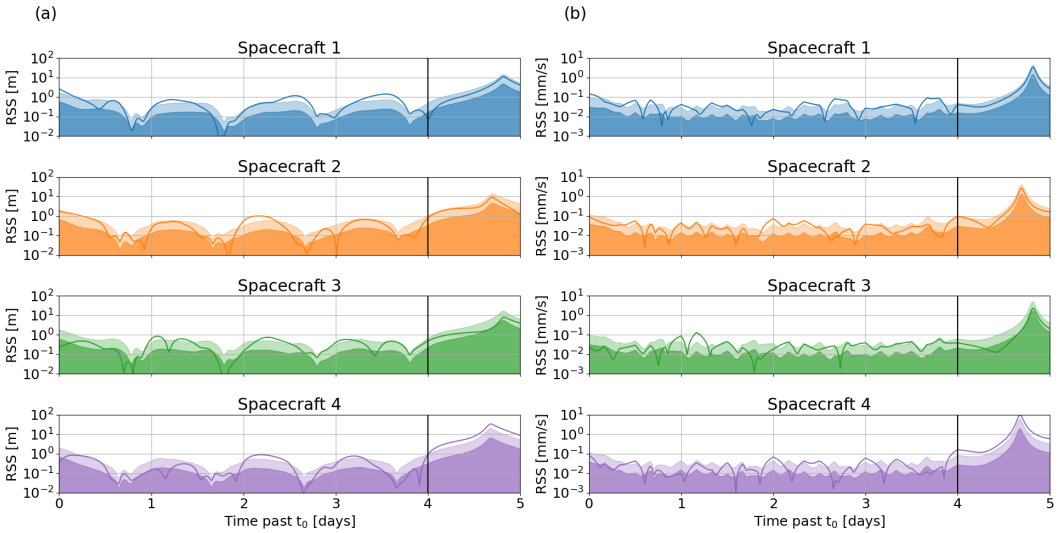

Figure 6.9. RSS of position (a) and velocity (b) accuracy for the four spacecraft in a randomly selected OD arc. The dark shaded area indicates the 1-σ accuracy, while the light color area is for the 3-σ, and the color solid line shows the estimation error. The vertical black line indicates the epoch of the last tracking data point. The right side of the solid black line shows the orbital error evolution (ephemerides aging) [Sesta et al., 2024].

the 3-σ formal uncertainty. This behavior is caused by the bias introduced on the range measurements and the dynamical model mismodeling, which have not been fully compensated in the estimation process.

In the numerical simulation, the uncertainty and error have been computed in different reference frames, namely ICRF (Moon-centered) and Radial-Transverse-Normal (RTN) with respect to the Moon and the Earth, as shown respectively in Fig. 6.10, Fig. 6.11, Fig. 6.12 for one of the spacecraft of the constellation. The RTN toward the Earth (or Moon) is defined with the R-axis pointing from the Earth (or Moon) toward the spacecraft, the N-axis is along the orbit normal (parallel to $r \times v$ where r and v are respectively the spacecraft position and velocity vector), and the T-axis completes the right-handed frame (velocity is generally mostly along this axis).

As shown in the figures, the accuracies are comparable across the three directions in the first two reference frames. However, in the last frame, the radial direction is significantly more accurate than the other two. In this frame, the spacecraft position and velocity are determined with the best accuracy along the Earth-spacecraft (radial) direction, more than a factor of 10 better than in the two orthogonal directions (at the centimeter level). This is because this direction is close to LOS, along which the radiometric observables provide most of the information. The positioning accuracy along the LOS is especially important to evaluate the performance of the synchronous time transfer as shown in Eq. 3.41 where the dependence of the desynchronization observables from the ρ_{23}, obtained from the OD process, is clear.

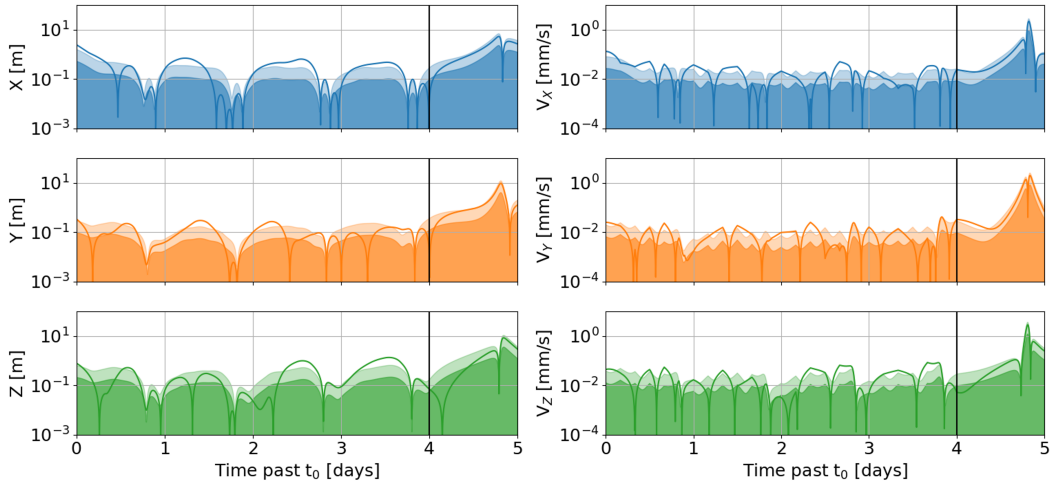

Figure 6.10. Position (left) and velocity (right) accuracy in X, Y, Z (ICRF, centered on the Moon) for one of the spacecraft in a randomly selected OD arc. The dark shaded area indicates the 1-σ accuracy, while the light color area is for the 3-σ, and the color solid line shows the estimation error. The vertical black line indicates the epoch of the last tracking data point. The right side of the solid black line shows the orbital error evolution (ephemerides aging).

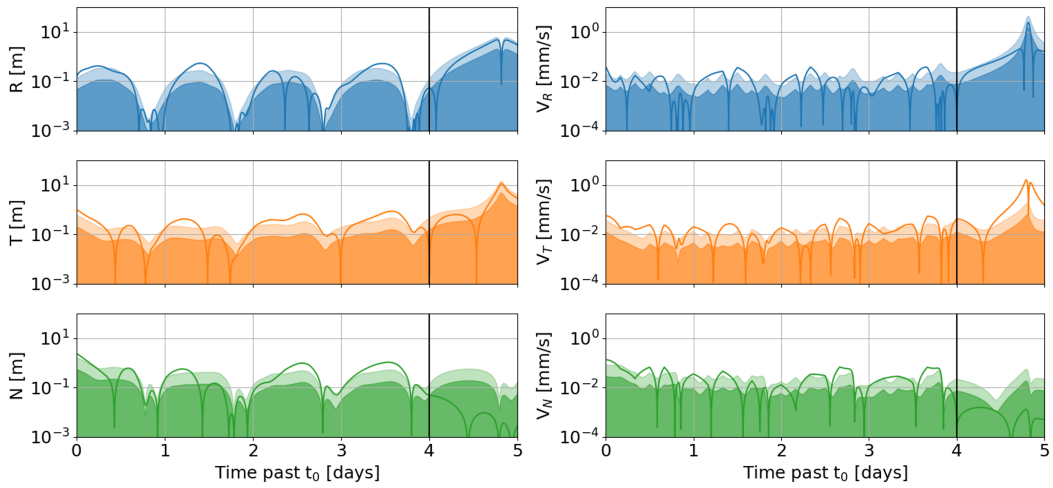

Figure 6.11. Position (left) and velocity (right) accuracy in R, T, N (RTN to the Moon, centered on the Moon) for one of the spacecraft in a randomly selected OD arc. The dark shaded area indicates the 1-σ accuracy, while the light color area is for the 3-σ, and the color solid line shows the estimation error. The vertical black line indicates the epoch of the last tracking data point. The right side of the solid black line shows the orbital error evolution (ephemerides aging).

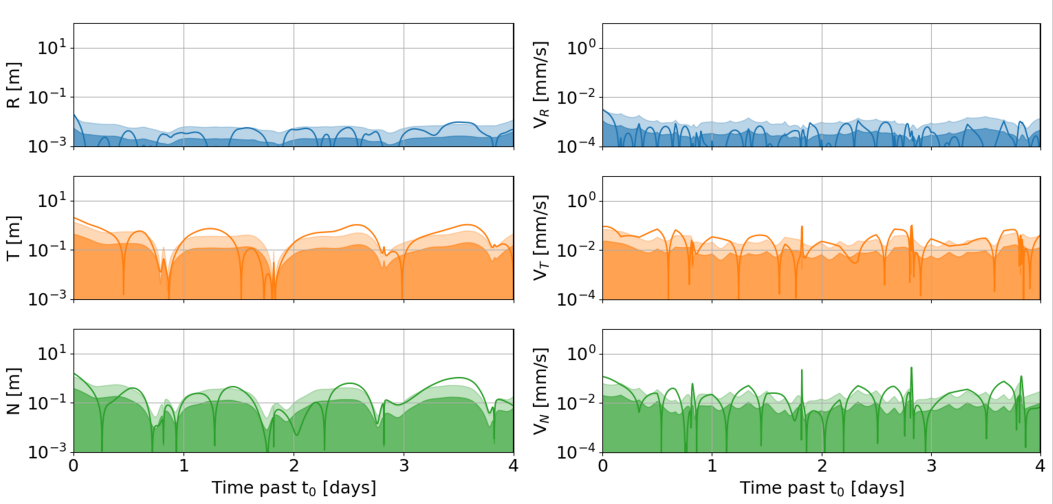

Figure 6.12. Position (left) and velocity (right) accuracy in R, T, N (RTN to the Earth, centered on the Moon) for one of the spacecraft in a randomly selected OD arc. The dark shaded area indicates the 1-σ accuracy, while the light color area is for the 3-σ, and the color solid line shows the estimation error.

6.7.2 Monte Carlo Outcome and SISE

In the Monte Carlo analysis, the state uncertainty and error have been collected for all the cases to produce relevant statistics. Fig. 6.13 shows histograms of orbital accuracy and errors for the LRNS constellation for the different data arcs selected in the analysis. Panels (a) and (b) of the figure show the Root Mean Square (RMS) of, respectively, the position uncertainty and the estimation error computed within the OD arc, for all the different cases. The histogram bars represent the percentage of cases where the RMS position accuracy and error are inside the range of values reported in the x-axis, over a 4-day observation arc. It is important to stress that the RMS value cannot be used to infer the estimation error at the end of the arc, given that it is an averaged value over the whole arc. Rather, it is an indication of how well the orbital fit performs under varying orbital geometries and tracking periods.

Another relevant parameter is the distribution of the error at the last data point of each arc for each spacecraft of the constellation since it represents the starting point for the aging of the ephemerides. This quantity is reported in Fig. 6.14 as a function of the corresponding spacecraft true anomaly at the last data epoch, with colors indicating the Sun-Probe-Earth (SPE) angle and the red line representing the median (50^{th} percentile) performed every 70 points. The lower density near the periselene is related to the higher spacecraft velocity in that region so fewer arcs end in that region. Given that the results represent the accuracy at the last data point, they are obtained without accounting for the ephemerides aging.

Looking at the median reported in Fig. 6.14, the position error at the last data point decreases up to a factor 6 (on average) if the spacecraft is close to the periselene. Indeed, here the gravity gradient is larger, thus the position and velocity change

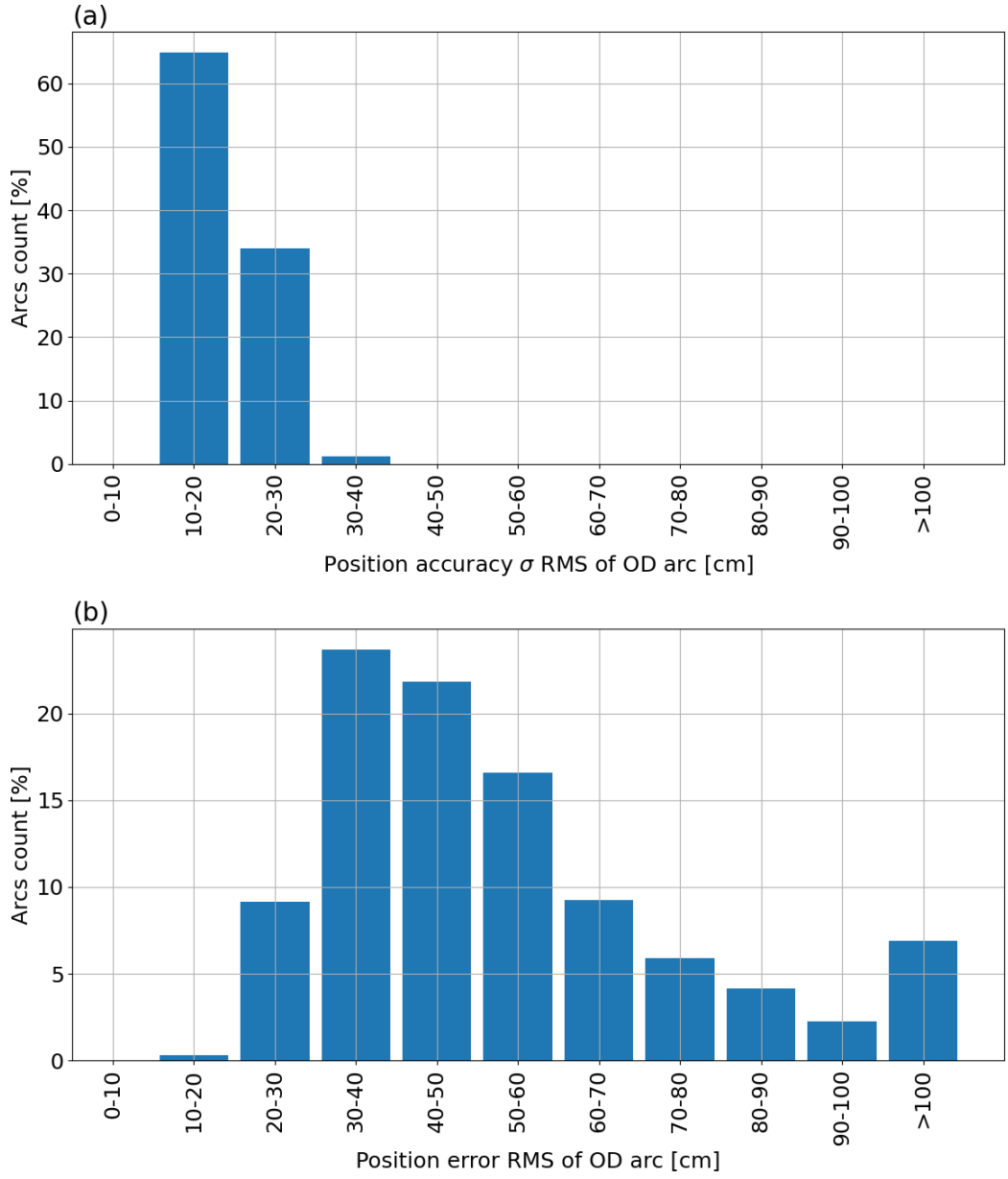

Figure 6.13. Histogram of the RMS value of position accuracy (a) and position error (b) as a function of the arc count percentage for the baseline case. The RMS value is computed from the orbital fit over a 4-day arc [Sesta et al., 2024].

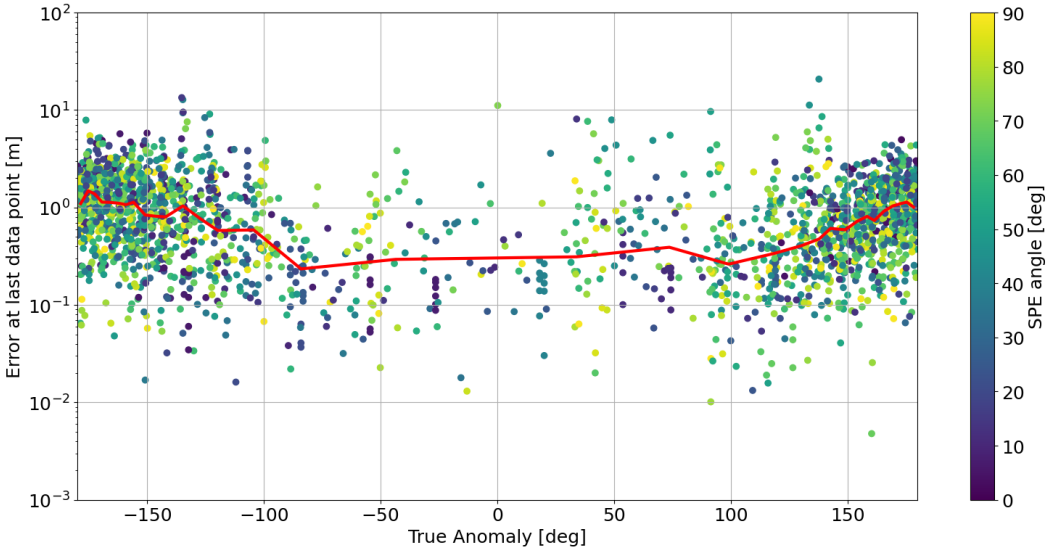

Figure 6.14. Distribution of the error in the last data point acquired in each arc as a function of the corresponding satellite true anomaly and Sun-Probe-Earth angle (colormap). The red line represents the median (50^{th} percentile) performed every 70 points [Sesta et al., 2024].

rapidly, allowing a more accurate determination of the orbit.

The simulations do not show any obvious relation between the position error and the spacecraft orbit plane angle, that is, the angle between the satellite orbital momentum and the spacecraft-Earth direction (close to the Line Of Sight). Moreover, as shown in Fig. 6.14, the Earth-Sun-spacecraft relative geometry does not impact the results during the analyzed month, and no significant trend is expected on a yearly scale. Finally, also the dependency on the angle between satellite orbital momentum and the Sun-spacecraft direction has been investigated, finding no clear evidence of any strong correlation. This is mainly because other geometrical conditions are less influential than the variations caused by the pericenter and apocenter passes, given the high eccentricity of the ELFOs.

The constellation ephemerides determined in the OD process must be uploaded in the navigation message through a proper orbit representation method, usually, there are three options:

1. Keplerian elements with corrections.
2. Cartesian position and velocity series.
3. Polynomials such as trigonometric, Chebyshev, or Lagrange polynomial.

Any of these ephemeris representations are characterized by a certain deviation from the estimated spacecraft trajectory and shall contribute to the space components of the SISE defined in Eq. 1.3 ([Cortinovis et al., 2023]). However, [Iess et al., 2024] have analyzed different ephemeris representation techniques, showing that Chebyshev polynomials offer high accuracy and simplicity of the formulation for the lunar orbiter

broadcast ephemerid representation in high-eccentric orbits. With an appropriate selection of the numbers of coefficients (11 coefficient, thus a degree 10 polynomial) and time update (more frequently close to the periseline given the faster dynamics), it is possible to reach an error in the ephemeris representation in the order of a few cm. In particular, if each navigation message refers to an orbital span of one hour, using an approximation with Chebyshev polynomials of degree 10 (11 coefficients), the 95^{th} percentile of the orbital fit error is smaller than 11 cm. Therefore, it is possible to neglect this contribution to the SISE as shown below.

As said before, the OD contribution to the SISE is related to the ephemerides aging, since the navigation message received by the lunar user contains the satellite state prediction, thus propagated forward from the reference state used for the OD, and so its accuracy decreases. This deterioration is strictly related to the uncertainties in the spacecraft dynamical model. Of course, if the knowledge of the non-gravitational accelerations acting on the spacecraft is improved, the increasing trend of the error will be slower.

In the Monte Carlo-like analysis, the estimated covariance matrix and error of the satellite state have been numerically propagated forward and the information on the trajectory error as a function of the time past the last data point has been collected for all the analyzed cases. To obtain the SISE, this contribution adds to those due to the clock desynchronization, also expressed as a function of the time past the epoch of the last data point. The selected clock for the baseline architecture configuration is the miniRAFS, whose frequency stability used for the time synchronization process is reported in Fig. 6.7 as a function of the averaging time.

Fig. 6.15 shows the SISE position performance for the proposed LRNS satellite constellation as a function of the Age Of Data (AOD) defined as the elapsed time between the generation of a navigation message by the ground segment and its usage at user level ([European GNSS (Galileo), 2021]). The solid lines in Fig. 6.15 represent the SISE due to both OD and clock contribution, while the dashed lines consider only the ephemerides aging. The blue, orange, and green curves refer, respectively, to the mean value, the value corresponding to the 95% percentile and the 99% percentile, computed over all simulated arcs, spacecraft, and clock realizations. The shaded areas are obtained considering the minimum and maximum value of the SISE among the 4 spacecraft at each aging time, this representation allows us to understand the variability related to the SISE computed for the full constellation for the 3 curves. The 99% case has a large uncertainty due to the limited number of simulated cases associated with that percentile: the obtained ephemeris aging only excludes the worst ~6 arcs (1% of the 577 cases). The main contribution to the SISE position is due to the orbital term: the ephemeris aging.

This behavior is different for the SISE velocity, shown in Fig. 6.16, where the clock contribution is more relevant, almost at the same order of magnitude than the OD one, especially for high AOD.

As said before, the SISE is defined as a function of the AOD, thus it does not consider the epoch at which the last observables are collected. The update of the ephemerides is only related to the navigation message generation time. The SISE evolution as a function of time reported in Fig. 6.15 and Fig. 6.16 should drive the

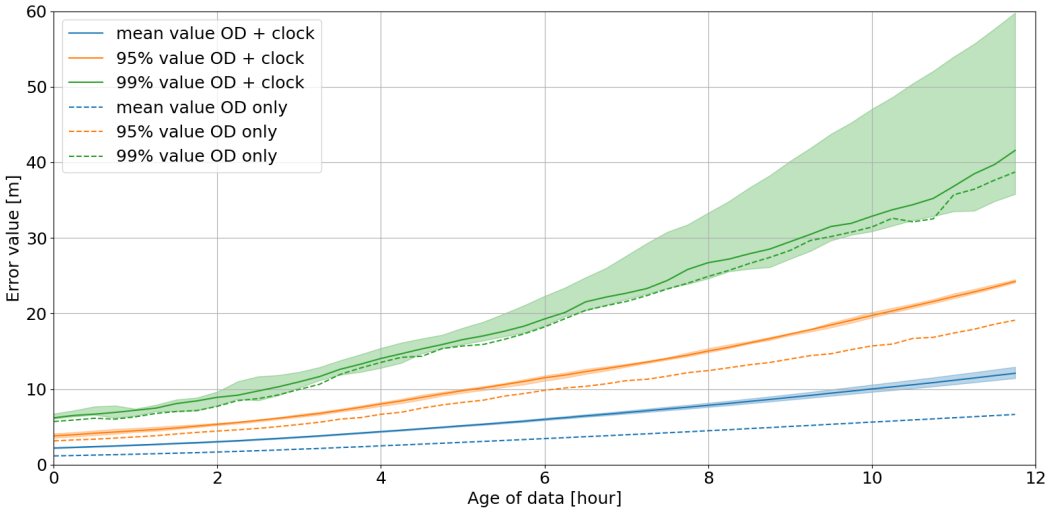

Figure 6.15. Evolution of SISE position as a function of the aging time and considering miniRAFS as onboard clocks. The solid lines represent the SISE due to both OD and clock contribution, while the dashed lines report only the OD contribution. The blue curves show the mean value, the orange ones the 95% value, and the green ones the 99% value of all the simulated arcs (and clock realizations). The shaded areas are obtained by evaluating the mean, 95%, 99% value of the SISE for each spacecraft and then getting the maximum and minimum value of the mean, 95%, 99% value of the SISE among the 4 satellites at each age of data [Sesta et al., 2024].

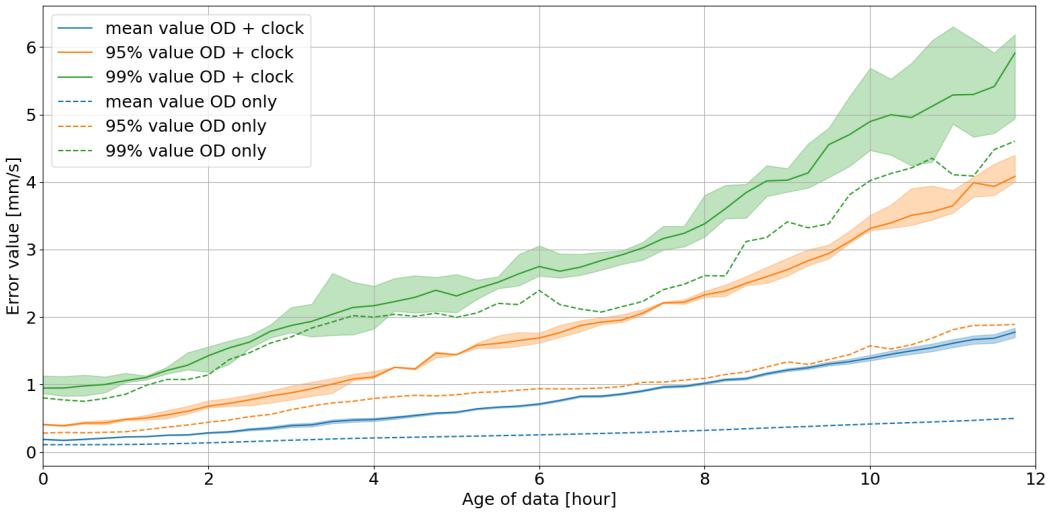

Figure 6.16. Evolution of SISE velocity as a function of the aging time and considering miniRAFS as onboard clocks. The solid lines represent the SISE due to both OD and clock contribution, while the dashed lines report only the OD contribution. The blue curves show the mean value, the orange ones the 95% value, and the green ones the 99% value of all the simulated arcs (and clock realizations). The shaded areas are obtained by evaluating the mean, 95%, 99% value of the SISE for each spacecraft and then getting the maximum and minimum value of the mean, 95%, 99% value of the SISE among the 4 satellites at each age of data.

choice of the frequency update of the navigation message to ensure the required performance of the LRNS constellation and the associated desired positioning performance of its future lunar users, which is related to the accuracy of the navigation message (as shown by the equations presented in Chapter 1).

Chapter 7

LRNS Supplementary Analysis

7.1 Additional Scenarios

The proposed LRNS (Lunar Radio Navigation System) architecture has been analyzed in different scenarios to evaluate the effect of the different system design choices on the PNT (Position Navigation and Timing) performance of the lunar constellation. In the additional scenarios that have been studied, the main differences are:

1. The adoption of different onboard clocks for the satellites of the constellation, namely the USO and the RAFS presented in Section 6.5.

2. The SBI (Same Beam Interferometry) technique is not implemented, and only Doppler and SS ranging data are collected during the observation arcs and processed in the orbit determination filter.

3. Water Vapor Radiometer calibrations of the wet tropospheric path delay are replaced by a GNSS-based calibration ([Tondaś et al., 2020]; [Dousa and Vaclavovic, 2015]). We assumed 80% calibration of the wet path delay (systematic effect). We changed the observables error budget accordingly obtaining the following measurement noise (same count time as the baseline configuration):

   - Doppler: ~1.31 mHz at 60 s.
   - Range: ~33.4 cm at 10 s.
   - SBI: ~5.0 mm at 60 s.

4. A fourth station at Mauna Kea (Hawaii) is included, to avoid visibility gaps and enable continuous visibility from the ground.

5. An improved dynamical model is adopted, the mismodeling of the SRP acceleration decreases from 5% to 2.5%. The empirical accelerations have the same batch interval but an a priori uncertainty of 1.0×10^{-9} m/s^2.

In the first case, changing the onboard clock and selecting one with lower (USO) or higher (RAFS) long-term frequency stability affects the desynchronization error, especially for longer Age Of Data (AOD). In the third scenario, the SISE (Signal-In-Space Error) increases due to the degraded media calibration level. Instead, the

fourth case implies a better performance for the system, given that radiometric observables are collected in larger quantities and with more continuity. Note that for the second case, the tracking system remains the same, and the only difference lies in the data analysis procedure. Finally, the last scenario implies an improvement of the ephemeris aging due to the decreased dynamical mismodeling. The comparison between these different scenarios is reported in Table 7.1, considering the miniRAFS as the onboard clock for the satellites of the constellation if not reported otherwise.

Table 7.1. Comparison in terms of position between the different scenarios changing the architecture hypothesis, considering the miniRAFS as the onboard clock for the spacecraft of the LRNS constellation if not specify otherwise.

$SISE_{pos}$ cases	**Mean error RMS value in OD arc**	**Time to reach $SISE_{pos}$ = 20 m (AOD)**		
		Mean value	95% value	99% value
Baseline	0.62 m	> 12 h	~10 h 7 min	~6 h 13 min
OD only	//	> 12 h	~12 h	~6 h 23 min
With RAFS	//	> 12 h	~12 h	~6 h 22 min
With USO	//	~10 h 16 min	~4 h 54 min	~2 h 56 min
No SBI	0.68 m (+10%)	> 12 h	~10 h 29 min	~6 h 46 min
No WVR	0.77 m (+24%)	> 12 h	~9 h 25 min	~6 h 1 min
With 4^{th} station (continuous coverage)	0.42 m (-32%)	> 12 h	~11 h 9 min	~4 h 57 min
Improved dynamical model	0.48 m (-23%)	> 12 h	~11 h 36 min	~7 h 10 min

Table 7.1 shows that given the higher long-term frequency stability of the RAFS, the desynchronization contribution to the SISE is almost negligible. At the same time, the SISE increases significantly for the USO, especially at longer time scales, due to the poor long-term stability of this clock as seen in Fig. 6.7. As expected, the error in the recovery of the trajectory increases if the SBI observables or the WVR are not used; on the contrary, the error is reduced if an additional station is considered or a better dynamical model is used, as shown from the mean RMS value in the Table 7.1. Concerning aging, the above three assumptions do not show significant variations, mainly because the aging of the ephemeris is largely driven by the inaccuracies in the dynamical model and the highly eccentric orbits. Indeed, the last scenario shows the largest improvement of the SISE performance maintaining the same onboard clock.

It is possible to note that using the SBI does not significantly change the OD performance. This is mainly related to the fact that the phase ambiguity is not solved (see Section 3.3) with the adopted ranging system accuracy. As a result, it is necessary to introduce a bias parameter for each spacecraft pair and ground station for each tracking pass, as shown in Table 6.6, thus degrading the performance of the SBI measurements. However, it is important to note that the SBI observables can

be generated without additional hardware at the ground station, directly from an open-loop receiver using MSPA, and their usage still improves the OD solution. The improvement in the OD solution brought by the SBI is due to its capacity to cancel out a significant portion of the common noise in the observables (see Section 3.3). This leads to more accurate measurements, enhancing the OD accuracy, particularly along the Line Of Sight direction, and consequently reducing also the OD error contribution to the time synchronization. As said before, note that the 99% values in Table 7.1 have large uncertainties due to the limited number of simulated arcs, given this reduced number of cases for the statistic, there is a large uncertainty in the value as seen from Fig. 6.15.

The same analysis has been performed for the SISE velocity obtaining the result reported in Table 7.2. In this scenario, the same considerations apply to the orbit reconstruction uncertainties of the different cases. However, the $SISE_{vel}$ aging behavior is different: the clock contribution is more relevant than the OD one. Table 7.2 shows that the improvement in the orbit reconstruction and ephemeris aging (better dynamical model) or a worsening (no WVR) does not affect significantly the $SISE_{vel}$, because it does not influence the evolution of the desynchronization error, which is mainly related to the clock frequency stability. Indeed, while the OD accuracy along the Line Of Sight affects the desynchronization measurement used to fit the clock model, it does not influence the clock behavior over time which will drift from the model one according to its ADEV. This aspect is also evident when looking at the performance difference between the scenario using the miniRAFS (baseline) and the one with RAFS (higher long-term frequency stability), with USO (lower long-term frequency stability) or the OD only case.

Table 7.2. Comparison in terms of velocity between the different scenarios changing the architecture hypothesis, considering the miniRAFS as the onboard clock for the spacecraft of the LRNS constellation if not specify otherwise.

$SISE_{vel}$ cases	**Mean error RMS value in OD arc**	**Time to reach $SISE_{vel}$ = 1 mm/s (AOD)**		
		Mean value	95% value	99% value
Baseline	0.049 mm/s	~7 h 54 min	~3 h 43 min	~44 min
OD only	//	> 12 h	~7 h	~1 h 15 min
With RAFS	//	> 12 h	~6 h 51 min	~1 h 14 min
With USO	//	~7 h 22 min	~48 min	– (start > 1 mm/s)
No SBI	0.052 mm/s (+6%)	~7 h 15 min	~3 h 31 min	~38 min
No WVR	0.058 mm/s (+18%)	~6 h 59 min	~3 h 29 min	~1 h 32 min
With 4^{th} station (continuous coverage)	0.039 mm/s (-20%)	~7 h 56 min	~3 h 37 min	~1 h 51 min
Improved dynamical model	0.035 mm/s (-29%)	~8 h 5 min	~3 h 41 min	~1 h 12 min

7.2 Effect of Orbital Maneuvers

During the mission lifetime, the LRNS satellites will perform several orbital maneuvers to maintain the nominal orbits and assure the PNT services to lunar users. The presence of maneuvers affects the ability to accurately recover the orbits of the spacecraft, given that the dynamical coherence of the orbit suffers a sharp change, and additional parameters must be estimated. During these operations, the LRNS users experience a degradation or interruption of service. There are two possible approaches to deal with this problem in the orbit determination process:

1. Restart the orbit determination process after the maneuvers.
2. Include the maneuvers in the OD process and estimate associated Δv parameters.

In both cases, it is necessary to estimate the recovery time of the LRNS system, that is the time interval to return to the nominal positional accuracy of the spacecraft. In the second approach, the one that is analyzed in this work, it is not necessary to restart the OD process, but the orbital maneuvers must be included in the satellite trajectory propagation and estimated by the OD filter. To assess the impact of a maneuver for ephemeris aging, it is possible to compare the positioning uncertainties when a maneuver is included or not.

The numerical simulations are performed in the baseline scenario described before, but now, they are done by considering the orbital maneuvers. Four different cases are simulated to analyze how the location of the maneuver (in terms of true anomaly, θ) affects the OD performance inside one 4-day observation arc (maximum one maneuver per spacecraft):

1. All 4 spacecraft of the constellation perform a maneuver at a given epoch (pessimistic scenario):
   (a) Two spacecraft will be at the pericenter.
   (b) Two spacecraft will be close to 120° true anomaly.
2. Only the spacecraft pair at the pericenter ($\theta = 0°$) at the given epoch performs the maneuver.
3. Only the spacecraft pair at θ ~120° at the given epoch performs the maneuver.
4. The maneuver is performed by two satellites at the apocenter ($\theta = 180°$).

In the estimation process, the orbital maneuvers have been included at a fixed epoch, with an a priori uncertainty of 6 mm/s on each component. Then, the ratio between the OD position formal uncertainty with and without the maneuvers (defined as the uncertainty scaling factor in Table 7.3) is measured at different aging times. Given the fixed epoch of the maneuvers, it is necessary to gradually shift the 4-day observation arc to obtain an increasing time interval between the maneuvers and the end of the OD arc (start of the age of data). In this way, it is possible to estimate the recovery time, which can be defined as the amount of data collected

after the maneuvers (expressed as hours) needed to obtain a degradation of the position accuracy smaller than 20%, as reported in Table 7.3. For each case, the results are obtained as the mean between the uncertainty scaling factors of the spacecraft that performs the maneuvers.

The analysis shows that if the maneuvers occur near the periselene, the recovery time of the positioning uncertainty decreases, since the OD reconstruction significantly improves thanks to the larger gravity gradient. Indeed, the time interval to reach a scaling factor smaller than 1.2 (i.e., a degradation of 20%) goes from 2 hours (case 2) to 6 hours if the maneuver is done near/at the aposelene (case 1b, 3, and 4). It is interesting to note that, if the maneuvers happen near the periselene, an hour of data is enough to obtain a good orbit reconstruction (a degradation factor of ~1.5) even in the pessimistic scenario (case 1a). Not surprisingly, the results reported in Table 7.3 (values for AOD at 2 and 6 hours) show that the performance degradation is almost independent of the age of data since the trajectories evolution after the last data point is strictly related to the dynamical model, which is the same in all cases. Note that in Table 7.3 results of cases 1a and 1b are not reported given that they are similar respectively to cases 2 and 3.

Given that the main objective of the LRNS constellation is to offer PNT service to lunar users at the Moon South pole and that the orbit apocenter is above this region, the most likely scenario for the spacecraft maneuvers is case 2, namely maneuver at the pericenter (out of the predicted service region [Moonlight Team, 2024]). The improved performance in this scenario is due to two key factors. First, the maneuver is performed at the orbit pericenter, where any orbital variations have a greater effect, making them easier to reconstruct during the OD process. Second, the data used to reconstruct the orbit after the maneuvers are close to the periselene, which, as previously noted, allows for better OD reconstruction due to the stronger gravity gradient.

Table 7.3. Impact of the orbital maneuvers on the ephemerides aging as a function of the amount of data collected. It is important to note that for each case the values reported in the table are the mean of the scaling factors of the satellites performing the maneuver.

Amount of data collected after maneuver	**Uncertainty scaling factor, $\sigma_{man}/\sigma_{no\_man}$**								
	AOD = 0 h			AOD = 2 h			AOD = 6 h		
	Case 2	Case 3	Case 4	Case 2	Case 3	Case 4	Case 2	Case 3	Case 4
1 hour	×1.43	×6.97	×3.19	×2.04	×11.4	×6.99	×2.80	×12.4	×10.5
2 hour	×1.13	×2.63	×1.41	×1.12	×3.02	×1.81	×1.11	×3.06	×2.09
4 hour	×1.16	×1.42	×1.24	×1.20	×1.36	×1.34	×1.27	×1.29	×1.30
6 hour	×1.05	×1.09	×1.08	×1.04	×1.07	×1.08	×1.04	×1.07	×1.06

Chapter 8

LRNS Secondary Users: Moon Transfer Orbit Scenario

The availability of a LRNS (Lunar Radio Navigation System) constellation around the Moon is beneficial not only for its primary users at the South Pole but also for a series of secondary ones. During my visiting period in the Mission Analysis section at ESOC, I have proposed and analyzed the application of the LRNS for a Moon Transfer Orbit (MTO). This future lunar constellation can be used with the GNSS to enable autonomous onboard orbit determination during Earth-Moon transfer orbit, reducing drastically the ground station support thus decreasing the mission cost. The possibility of collecting pseudo-range observations from the LRNS allows us to solve different problems related to the GNSS-only orbit determination for high altitude and especially for lunar transfer close to the arrival already presented in Chapter 1, namely (repeated here for clarity purposes):

1. Reduce the DOP (Dilution Of precision) related to using the pseudo-range observable coming from the GNSS due to the elevated distance between the spacecraft and the constellation. For this reason, all the observations come from almost the same direction in the FOV of the spacecraft, thus the elevated DOP. This additional constellation (LRNS) will solve this problem given that these additional observations are coming from a different direction in space.

2. Improve the orbit determination accuracy in the final part of the lunar transfer thanks to the more accurate pseudo-range observations coming from the LRNS given the higher signal-to-noise ratio and the more favorable geometry.

This on-board orbit determination approach allows us to avoid relying on the ground station's infrastructure thus reducing the mission costs and requirements, especially considering the high number of missions planned towards the Moon. Thus it is possible to analyze the performance of the proposed OD (Orbit Determination) approach in terms of positioning uncertainty along the transfer orbit. For such a scenario positioning uncertainty is paramount to design and execute the orbital maneuvers to reach the desired lunar target orbit. The simulation for this analysis was performed with the ESA/ESOC flight dynamics software GODOT [ESA, 2022b] enhanced with an additional python module which I developed to handle and model the radio links between the spacecraft during the transfer and the GNSS and LRNS. In this scenario,

a covariance analysis is performed to assess OD positioning uncertainty. In contrast, previous simulations of LRNS performance analyzed state errors by introducing dynamical mismodeling and systematic observation errors. This is because, for the LRNS architecture, the key performance parameter for system validation is the SISE (Signal-In-Space Error). Consequently, analyzing the estimation error, its temporal evolution, and the associated statistics is essential. However, in the scenario analyzed in this section, the focus is on evaluating the improvement achieved by using the LRNS in conjunction with the GNSS. For this purpose, a covariance analysis is sufficient to achieve the objective.

It is important to note that for this scenario the spacecraft in the transfer orbit is a secondary user for both the GNSS and LRNS, indeed both satellite navigation constellations are going to be pointed towards the respective principal body (Earth and Moon) to provide PNT (Position Navigation and Timing) service to the surface users.

8.1 Simulation Setup

The proposed scenario for the analysis is a small satellite lunar transfer targeting a low lunar circular polar orbit, similar to the lunar trailblazer mission by NASA ([Ehlmann et al., 2022]).

8.1.1 Orbit Geometry

The desired arrival orbit is a low circular lunar polar orbit (100 km altitude) and the lunar transfer orbit (time of flight of 4 days) is shown in Fig. 8.1 together with the GNSS, LRNS and Moon trajectories in the ICRF. The Galileo and Global Positioning System (GPS) orbits are defined through the Two-Line Element (TLE), while the LRNS constellation is the one described as baseline (see Table 6.2). The analyzed transfer trajectory starts from launcher separation up to before the lunar orbit insertion maneuver, and 1 day after launcher separation a Trajectory Correction Maneuver (TCM) is applied to target the desired low circular lunar polar orbit.

8.1.2 Radio Link Description

The assumption is that the spacecraft mounts on board a space-born GNSS receiver, such as the WeakHEO ([Capuano et al., 2016]) or the NaviMoon ([Giordano et al., 2021b]), to collect pseudo-range observations from both GPS and Galileo satellites. Since the future receiver for the LRNS satellites and the associated navigation message are still under definition, it is possible to assume them to be similar to the ones of the GNSS. Moreover, an omnidirectional antenna (0 dB gain) mounted on the target spacecraft is assumed to avoid strict pointing requirements and to provide a conservative estimate of the system's performance, also considering the need to acquire the signal from both the navigation constellation (GNSS and LRNS).

The assumption of employing GNSS signals is to use the L1 and E1 frequencies for the GPS and Galileo satellites. Given the lack of information regarding the

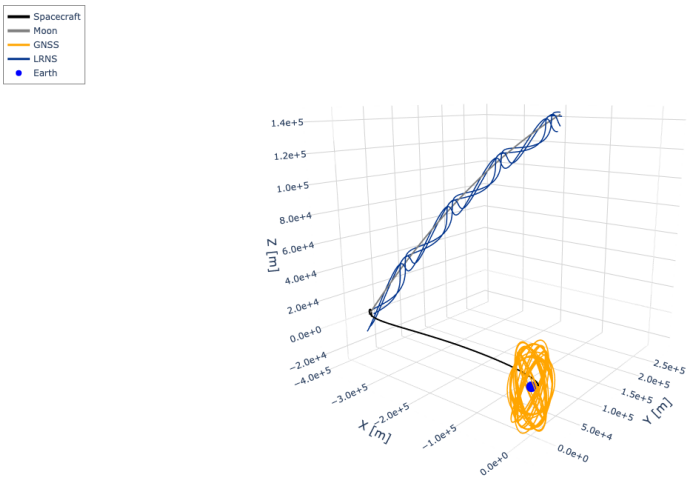

Figure 8.1. Orbital geometry for the Moon transfer trajectory and the GNSS, LRNS and Moon orbits during the transfer in an inertial reference frame (Earth-centered).

Galileo side-lobes power and the realistic transmission antenna pattern outside the main lobe ([Delépaut et al., 2020]), it is possible to assume adopting the GPS ones ([Marquis and Reigh, 2015]) also for the ESA satellite navigation constellation. Moreover, for the LRNS constellation it is assumed the same antenna pattern of GPS and that the frequency band to communicate from the lunar orbiters to the lunar surface users is the S-band (compatible with the dedicated frequency band reported in [SFCG, 2023a]). The transmitted signal power is in line with the GPS one (transmitted power for both GNSS and LRNS ~30 W [Wang et al., 2018]).

It is important to note that only the side-lobes of the GNSS antenna pattern can be used due to Earth occultation, thus reducing the antenna gain and consequently the signal-to-noise ratio of the established radio link. However, given that the link with the GNSS is established only using the side lobe of the antenna (once surpassed the GNSS orbit), the majority of the signal will not pass through the Earth's atmosphere thus it is possible to neglect the media effect on the radio link. Moreover, regarding the LRNS, given that the same antenna pattern is adopted and given that the Moon has a smaller radius than the Earth, the link between the spacecraft in the transfer orbit and the lunar satellite constellation can be established not only with the side-lobes but also with the main one (only in some geometric configurations).

To model the radio link between the transmitter (GNSS and LRNS) and the receiver (the spacecraft in the transfer orbit) a python module based on GODOT has been developed to characterize the properties of the radio link, for example, the signal-to-noise ratio. Based on this, a threshold of 15 dB-Hz is set to establish the capability of decoding the GNSS (or LRNS) signal, obtaining the navigation message, and determining the number of satellites the spacecraft can track at each epoch (assuming 20 as the maximum number of simultaneous links for GNSS, which is relevant in the early phase of the lunar transfer as shown in Fig. 8.2). Fig. 8.2

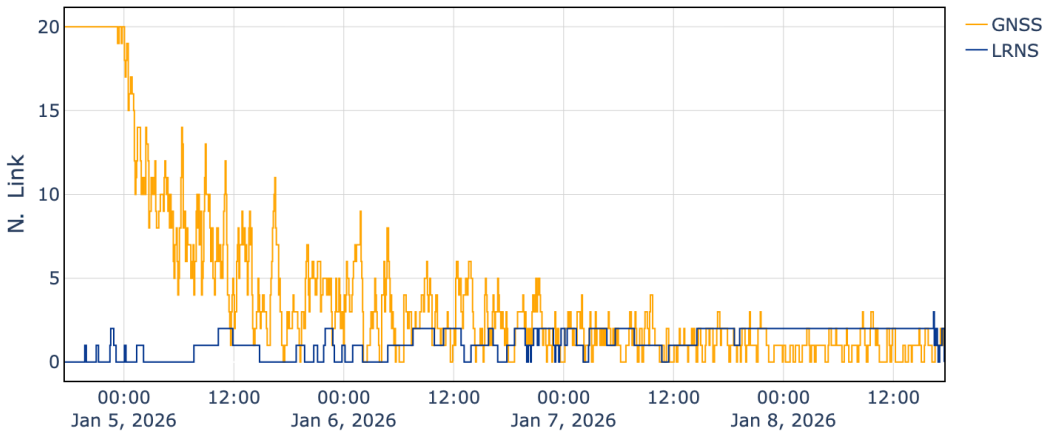

Figure 8.2. The number of established links between the satellites of the navigation constellations and the spacecraft in the transfer orbit. The orange and blue lines are associated with the GNSS and the LRNS.

shows the number of links established with the GNSS and LRNS as a function of time during the MTO.

To complete the description of the radio link, the following properties of the GNSS receiver (also assumed to apply to the LRNS constellation) are adopted (based on [Capuano et al., 2016]):

- Code loop noise bandwidth $B_n = 0.5$ Hz.
- Early-to-late correlator spacing $D = 1$ chip.
- Predetection integration time $T = 20$ ms.
- Front-end bandwidth $B_{fe} = 26$ MHz.
- Chipping rate $R_c = 1.023$ Mchip/s (with chip period $T_c = 1/R_c$).

8.1.3 Dynamical and Observation Models

The dynamical model of the spacecraft in the simulation phase includes:

- The gravitational monopole accelerations due to the Sun, Earth, the Moon, and Solar System planets.
- The spherical harmonics coefficients of the Earth ([Lemoine et al., 2019]) and the Moon ([Lemoine et al., 2014]), up to degree and order 10 for both.
- The non-gravitational acceleration due to the SRP acting on the satellite during the transfer orbit.

The other non-gravitational accelerations are not included given that in this scenario are negligible with respect to the SRP acceleration. To simulate the dynamical mismodeling in the covariance analysis, it is possible to introduce stochastic piecewise constant accelerations (on each component of the ICRF) in the dynamical model during the estimation step and the associated parameters among the ones estimated by the OD filter. These allow us to consider the impact of incorrect modeling of the non-gravitational accelerations on the final covariance matrix. The stochastic acceleration batches (process noise parameters) are updated every 4 hours during the lunar transfer with an a priori sigma of 4×10^{-9} m/s^2 and a time correlation of 12 hours for these exponentially correlated random variable parameters (available process noise parameters when adopting the default GODOT filter[1]). The value of the apriori uncertainty is in line with a 5% mismodeling of the SRP. Indeed, the selected spacecraft mass is 200 kg (smallsat) with the following shape:

- Solar panels with a total area of 3 m^2, always pointed towards the Sun.
- A rectangular bus with side faces covering an area of 0.9 m^2 each, and base areas of 0.4 m^2 each.

In the OD process, the spacecraft along the transfer orbit can collect pseudo-range observables from the GNSS and LRNS constellation in a one-way tracking configuration with a sampling time of 300 seconds. The pseudo-range measurement ρ_i with a generic GNSS (or LRNS) satellite at an epoch n is defined in [Hegarty and Kaplan, 2005] as:

$$\rho_i(n) = c[T_R(n) - T_{Ti}(n)] + \epsilon \tag{8.1}$$

where c and ϵ are respectively the speed of light and the measurement noise, while $T_R(n)$ and $T_{Ti}(n)$ are the receive time corresponding to epoch n of the GNSS (or LRNS) receiver's clock and the transmit time based on the GNSS (or LRNS) satellite clock. The Eq. 8.1 can be rewritten to make the contributions related to the distance between the transmitter and the receiver and the clock offsets of the receiver and the transmitter explicit as follows:

$$\rho = \sqrt{(x_R - x_{Ti})^2 + (y_R - y_{Ti})^2 + (z_R - z_{Ti})^2} + c(\delta t_R - \delta t_{Ti}) + \epsilon \tag{8.2}$$

where x_R, y_R, z_R is the receiver position at reception time, x_{Ti}, y_{Ti}, z_{Ti} is the transmitter position at transmission time, and δt_R and δt_{Ti} are respectively the receiver and transmitter clock offsets at reception and transmission times. In this analysis, the uncertainty related to the GNSS and LRNS ephemerides in the navigation message and their clock offset are taken into account as additional noise sources for the pseudo-range observables. In particular, the transmitter's clock and broadcast ephemeris errors of the GNSS (GPS and Galileo) are assumed to be about 1 m as presented in [Engel, 2008], while for the LRNS of about 10 m, which is in line with the ESA Moonlight requirements and the results shown in Section 6.7.2. The

[1]In this analysis, I utilized the default GODOT filter because this project was conducted during my visiting period at ESOC, where I exposed the observation module from `C++` to `Python`. As a result, I did not use the batch filter implemented in the `rsl` package (see Chapter 5). Instead, I employed the newly exposed observation module and the associated default GODOT filter.

spacecraft onboard clock is considered in the simulation and it is modeled with a constant bias, a drift term, and a quadratic component, namely:

$$\tau = a_0 + a_1(t - t_{ref}) + a_2(t - t_{ref})^2 \tag{8.3}$$

where the τ clock offset parameters a_0, a_1, a_2 are estimated in the OD filter and all of them are considered as process noise parameters with an update time of 12 hours. The value of the clock parameters are:

- $a_0 = 1.0 \times 10^{-6}$ s.
- $a_1 = 1.2 \times 10^{-11}$.
- $a_2 = 1.3 \times 10^{-16}$ s^{-1}.

The value of the constant clock bias (a_0) was chosen conservatively based on the synchronization performance of GNSS systems [Teunissen and Montenbruck, 2017]. The drift (a_1) and quadratic (a_2) terms were selected to ensure that the resulting clock desynchronization is comparable to the bias a_0 after one day. The a priori sigma of these process noise parameters are 1.0×10^{-6} s, 1.2×10^{-11} and 1.3×10^{-16} s^{-1} for respectively a_0, a_1 and a_2, with a time correlation of 12 hours. The reference time t_{ref} is the launcher separation epoch.

As said before, the link is going to be established only with the GNSS sidelobes (except for the small time window, ~1 hour, after launcher separation and before the crossing of the GPS altitude), so it is possible to neglect the Earth's atmosphere and the same can be done with the link with the LRNS satellites (their radio link with the satellite in the transfer orbit do not pass through the Earth atmosphere). Given these assumptions, the dominant error source for the pseudorange observables is the thermal noise range error jitter of the GNSS receiver code tracking loop, the Delay Lock Loop (DLL). For BPSK-R(n) modulations such as the ones adopted in this analysis, the thermal jitter noise is given by the following relations [Hegarty and Kaplan, 2005]:

$$\sigma_{tDLL} = \begin{cases} \sqrt{\dfrac{B_n}{2C/N_0} D \left[1 + \dfrac{2}{TC/N_0(2-D)}\right]}, & D \geq \dfrac{\pi R_c}{B_{fe}} \\ \sqrt{\dfrac{B_n}{2C/N_0} \left[\dfrac{1}{B_{fe}T_c} + \dfrac{B_{fe}T_c}{\pi - 1}\left(D - \dfrac{1}{B_{fe}T_c}\right)^2\right] \left[1 + \dfrac{2}{TC/N_0(2-D)}\right]}, & \dfrac{R_c}{B_{fe}} < D < \dfrac{\pi R_c}{B_{fe}} \\ \sqrt{\dfrac{B_n}{2C/N_0} \left(\dfrac{1}{B_{fe}T_c}\right)\left(1 + \dfrac{1}{TC/N_0}\right)}, & D \leq \dfrac{R_c}{B_{fe}} \end{cases} \tag{8.4}$$

Where C/N_0 is the power-to-noise ratio and the other terms, although previously defined, are repeated here for clarity:

- B_n: code loop noise bandwidth.
- D: early-to-late correlator spacing.

- T: predetection integration time.
- B_{fe}: front-end bandwidth.
- R_c: chipping rate.
- T_c: chip period.

According to this formulation, the measurement noise associated with the pseudo-range observables will change during the lunar transfer as the spacecraft goes further away from the Earth given that the power-to-noise ratio decreases. The other parameters are fixed once the GNSS receiver characteristics. The same considerations hold for the pseudo-range observables noise and radio link with the LRNS constellation, with the advantage that for some configurations even the antenna main lobe could be used.

The pseudo-range observables noise for both constellations (GNSS and GNSS) is obtained as white Gaussian noise (as done in Section 6.3) with a certain standard deviation (see [Hegarty and Kaplan, 2005]), that is computed as the RSS of the thermal jitter, the constellation ephemerides and clocks uncertainty contributions (values presented above for GNSS and LRNS) and an additional component of about 10 cm to conservatively take into account other possible error sources as suggested by [Capuano et al., 2016].

Table 8.1 reports the estimated parameters in the OD filter and in addition to the ones presented above there are:

- The spacecraft state at launcher separation in the ICRF (reference epoch is 2026-01-04 at 17:33:12 TDB), with an a priori uncertainty on state parameters obtained from a launcher dispersion for a Geostationary Transfer Orbit (GTO) [Arianespace, 2021], that is a reasonable assumption also for the MTO.
- The TCM magnitude and direction, with an a priori uncertainty equals 1% of the value for the maneuver magnitude and 3° degree for both maneuver direction angles.

Given that this MTO performance study is a covariance analysis, the a priori values of all the parameters in Table 8.1 coincide with their values in the simulation phase for the synthetic generation of the observables.

8.2 Results

To assess the advantages of using the LRNS constellation, the OD process for the lunar transfer orbit has been performed using both the GNSS and LRNS constellations, as well as with only the GNSS. Fig. 8.3 shows the position uncertainty (for each component) and the clock offset uncertainty (converted into position uncertainty) of the spacecraft during the lunar transfer orbit. These values are plotted as a function of time after launcher separation (processing only the observables up to that epoch) for both analyzed scenarios, namely the GNSS-only and GNSS+Lunar Radio Navigation System (LRNS) cases. It is interesting to note that before crossing

Table 8.1. List of the parameters estimated by the OD filter for the MTO with the associated a priori values and uncertainty.

Parameter	A priori value	A priori uncertainty
Spacecraft position components (ICRF)	[3807.2, 8357.9, -1082.9] km	[66.7, 116.5, 15.3] km
Spacecraft velocity components (ICRF)	[-5.0975, 7.5734, -0.9510] km/s	[51.1, 59.6, 7.7] m/s
TCM magnitude	14.3 m/s	0.14 m/s (1% value)
TCM direction (right ascension and declination in tangential, cross-track, normal frame satellite-Earth)	[160.04°, 181.51°]	3°
Spacecraft clock bias term (a_0)	1×10^{-6} s	1×10^{-6} s
Spacecraft clock drift term (a_1)	1.2×10^{-11}	1.2×10^{-11}
Spacecraft clock quadratic term (a_2)	1.3×10^{-16} s^{-1}	1.3×10^{-16} s^{-1}
Stochastic accelerations parameters	0.0 m/s^2	4×10^{-9} m/s^2

the GPS orbit, the position uncertainty decreases significantly, as it is possible to use the main lobe of the GNSS antenna before this point. When the observables from the LRNS are included, the positioning accuracy improves not only in the later stages of the transfer trajectory but also at the beginning. This is because the additional measurements come from different directions than the GNSS ones, addressing the high DOP issue of GNSS-only navigation.

Fig. 8.4 shows the RSS position uncertainty as a function of time after launcher separation (processing only the observables up to that epoch) using GNSS-only observables and using the combination of GNSS and LRNS data. Both scenarios are analyzed with and without the TCM among the OD filter parameters.

Looking at Fig. 8.2, it is possible to note that when the link with the LRNS is established, the OD performance increases (positioning uncertainty decreases). This behavior is more relevant towards the end of the lunar transfer orbit, near the Moon, where the introduction of LRNS pseudo-range observables improves the RSS position uncertainty by an order of magnitude compared to GNSS-only orbit determination. Indeed, near the end of the lunar transfer, the positioning uncertainty improves from hundreds of meters to tens of meters. This is because these additional measurements are more accurate, given the lower thermal jitter from the higher signal-to-noise ratio: the spacecraft is closer to the LRNS constellation.

It is interesting to note that using the LRNS data, it is possible to fully recover the TCM before reaching the lunar orbit: the solid line converges to the dashed one in the LRNS+GNSS case. This is particularly relevant given that good positioning

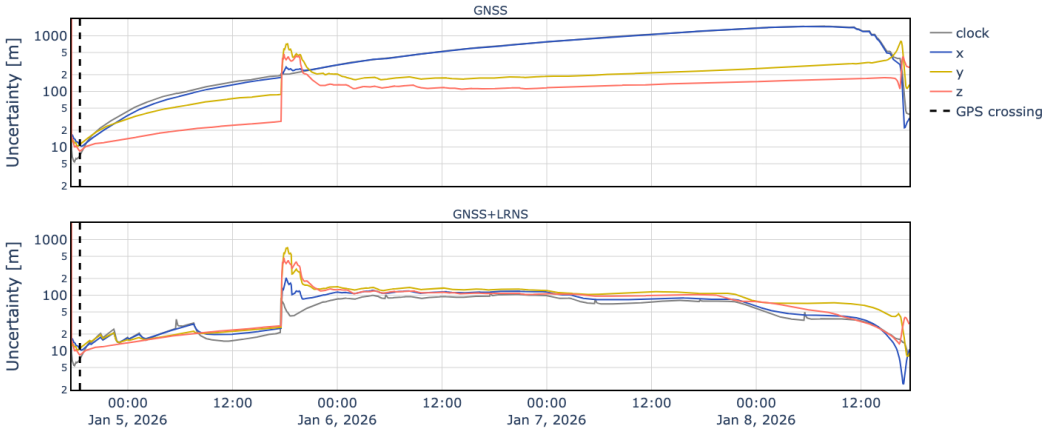

Figure 8.3. Position uncertainty (1-σ in x, y, z (ICRF, centered on the Earth) and clock offset uncertainty (1-σ, converted to position uncertainty) for the spacecraft during the MTO using GNSS-only observables (top) and combining GNSS and LRNS measurements (bottom). The blue, yellow, red, and gray lines show, respectively, the evolution of each position component (x, y, z) and clock offset uncertainty at each epoch for the GNSS-only and GNSS+LRNS scenarios processing the observations up to that epoch. The vertical dashed black line indicates the epoch when the satellite crosses the GPS altitude.

accuracy is fundamental to planning and executing the lunar orbit insertion maneuver, assuring a good targeting of the desired lunar orbit.

The improvement obtained by combining the GNSS and LRNS data characterizes also the spacecraft velocity uncertainty shown in Fig. 8.5. As expected, given that the uncertainty at each epoch is obtained by processing the observables up to that epoch, the effect of the maneuver uncertainty is the same in all the cases (same a priori uncertainty).

In both scenarios, the positioning uncertainty reaches its minimum when crossing the GPS altitude, as beyond this point, the spacecraft can only establish a link with the GNSS satellites using the side-lobes of the antenna, which decreases the signal-to-noise ratio and increases the thermal jitter of the measurements.

Finally, it is important to emphasize that in Fig. 8.3, Fig. 8.4 and Fig. 8.5 the uncertainty at a given epoch is obtained from the covariance matrix estimated by the OD filter, processing the observables up to that point. This allows us to evaluate the performance of the onboard OD process at any point during the lunar transfer orbit as the satellite approaches the Moon. It is worth noting that the shown results are obtained in a pessimistic scenario under certain assumptions, e.g. the dynamical mismodeling or the onboard omnidirectional antenna (with 0 dB gain). Thus, an improvement of the hypothesis of the scenario will reduce the uncertainty of the orbit reconstruction, however, the advantages and improvements related to the LRNS usage in conjunction with the GNSS are relevant and noticeable from the performed analysis.

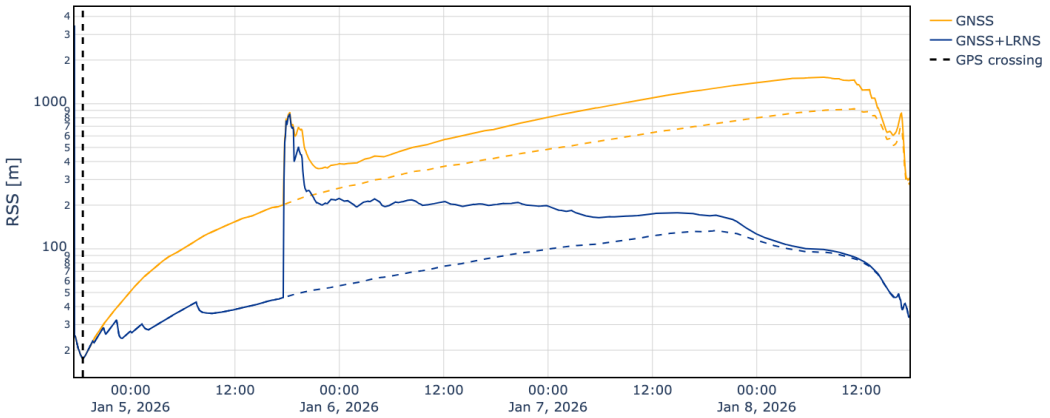

Figure 8.4. RSS of position uncertainty (1-σ) for the spacecraft during the MTO as a function of time after launcher separation. The solid orange and blue lines show the evolution of the RSS position uncertainty at each epoch for the GNSS-only and GNSS+LRNS scenarios, processing the observations up to that epoch. The dashed orange and blue lines correspond to the same scenario described above but assuming that the TCM is known exactly, thus the TCM is not among the estimated parameters. The vertical dashed black line indicates the epoch when the satellite crosses the GPS altitude.

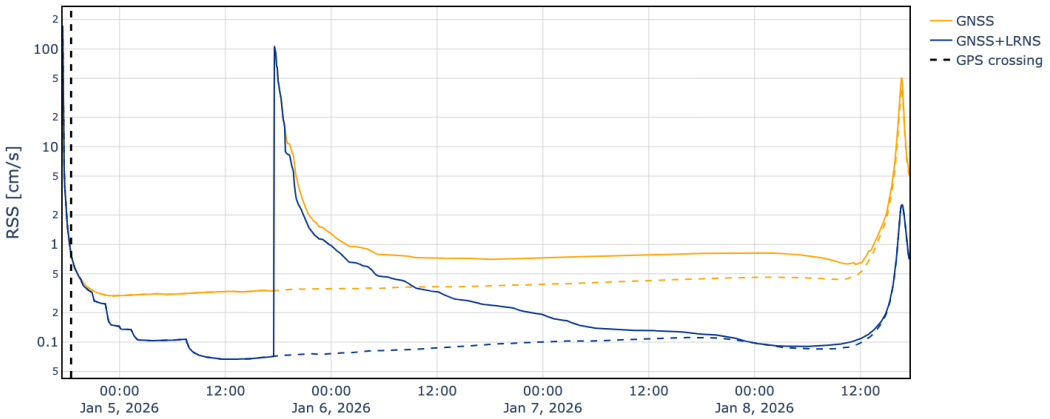

Figure 8.5. RSS of velocity uncertainty (1-σ) for the spacecraft during the MTO as a function of time after launcher separation. The solid orange and blue lines show the evolution of the RSS velocity uncertainty at each epoch for the GNSS-only and GNSS+LRNS scenarios, processing the observations up to that epoch. The dashed orange and blue lines correspond to the same scenario described above but assuming that the TCM is known exactly, thus the TCM is not among the estimated parameters. The vertical dashed black line indicates the epoch when the satellite crosses the GPS altitude.

Chapter 9

Conclusions

This thesis focuses on the two main concepts:

1. The proposal and validation of a lunar radio navigation system architecture to provide PNT (Position Navigation and Timing) services to future lunar users. I evaluated the orbit determination and time synchronization system performance through the most relevant index: the Signal-In-Space Error, as explained in Chapter 1.

2. The proposition and analysis of a possible secondary user for the LRNS (Lunar Radio Navigation System) described above, namely the OD for a lunar transfer orbit using in conjunction GNSS and LRNS data. The most interesting aspect of this configuration is that it allows us to autonomously perform the orbit determination onboard the spacecraft, thus reducing the need for ground support and paving the way for autonomous guidance of the satellite.

The first objective of my research was to present and analyze the baseline architecture of the LRNS. The proposed system relies on a dedicated ground network of small tracking stations (~26 cm of diameter), able to establish simultaneously two-way coherent K-band links with all the satellites of the constellation thanks to MSPA (Multiple Spacecraft Per Aperture) tracking and CDM-M (Code Division Multiplexing with Majority voting) technique. The orbit determination is based on spread spectrum ranging, Doppler, and SBI (Same Beam Interferometry) measurements. At the same time, the ground-to-space time synchronization can be performed without interrupting the tracking operations, thanks to the proposed novel approach based on two-way coherent ranging measurements, assisted by orbit determination. The clock comparison can be performed any time a satellite is visible from a ground station, i.e., almost continuously as shown in Fig. 6.5, thus reducing the degradation of the LRNS service due to onboard clock drifts.

The proposed navigation constellation can satisfy the ESA Moonlight requirements both for the Initial Operational Capability (IOC) and Full Operational Capability (FOC) phases. In particular, the required positioning and velocity performances for the real-time SISE (AOD $>$ 0 hours) are the following ([Moonlight Team, 2024]):

- SISE_{pos} shall be less than:
  - IOC: 20 m at least 95% of the time over any 24 hours.

  - FOC: 10 m at least 95% of the time over any 24 hours.

- $SISE_{vel}$ shall be less than:

  - IOC: 2 mm/s at least 95% of the time over any 24 hours.
  - FOC: 1.5 mm/s at least 95% of the time over any 24 hours.

In the baseline configuration, looking at the 95% lines of Fig. 6.15 and Fig. 6.16, the required time updates for the navigation message broadcasted by the LRNS to satisfy these requirements are (rounding up the value):

- $SISE_{pos}$: ~10 hours for the IOC and ~5 hours for the FOC.
- $SISE_{vel}$: ~7 hours for the IOC and ~5 hours for the FOC.

Selecting the value that satisfies both requirements at the same time, it is possible to obtain the navigation message update for both the LRNS phases: 7 hours for the IOC and 5 hours for the FOC.

In the baseline configuration, looking at Fig. 6.9, the OD reconstruction of the constellation ephemerides is at meter level (or less) and about 0.1 mm/s, respectively for the 3D spacecraft position and velocity. This result is obtained after only 4 days of data, thanks to the availability of precise SBI measurements and an accurate media calibration system.

After I evaluated the performance for the baseline configuration of the lunar navigation constellation, I analyzed the effect of the different LRNS system design choices on the SISE (see Table 7.1 and Table 7.2). From these simulations, it is clear that even if the usage of the SBI and WVR are relevant for the OD reconstruction together with the possibility to continuously track the constellation (with an additional 4^{th} station), the most relevant improvements in the SISE evolution are obtained by improving the dynamical model of the spacecraft (slower ephemerides aging) and the clock long-term frequency stability (lower desynchronization error). This is especially true for the $SISE_{vel}$ mainly affected by the clock behavior. Moreover, the selection of a clock with poor long-term stability greatly worsens the SISE performance even with an accurate OD reconstruction, as it is clear looking at the USO case in Table 7.1 and Table 7.2.

Another relevant aspect for the OD performance of any navigation satellite system, and more in general for any spacecraft, is the effect of orbital maneuvers, e.g., station keeping and reaction wheel desaturation maneuvers. I analyzed the effect of the maneuvers on the OD in different scenarios, namely for different orbital configurations of the execution of the maneuvers. The most likely scenario for these maneuvers is when the satellite is at the periseline, outside the expected service volume for the LRNS [Moonlight Team, 2024], to minimize the effect on the PNT service for the users at the Moon's South Pole. In this case, without restarting the OD process and with the possibility to track the satellite across the maneuver, the required amount of data to reach a degradation factor lower than 20% is just 2 hours (see Table 7.3).

The proposed architecture benefits from a relatively simple and compact implementation, both for the space and ground segments. In addition, the compactness of the ground infrastructure facilitates the expansion to an increased number of satellites and, ultimately, a global coverage of the Moon. Moreover, the proposed LRNS system, being based on high Technology Readiness Level (TRL) elements, is compatible with the timeline of the ESA Moonlight project, which envisages an initial deployment for the 2026-2027 time-frame.

In my thesis, I proposed a possible secondary use of the LRNS constellation: the application to a Moon transfer orbit. In particular, I analyzed the OD performance using pseudo-range observables from the LRNS in conjunction with the ones from the GNSS. This configuration allows us to perform an autonomous on-board orbit determination solving the main issues related to a GNSS-only navigation in cislunar space, namely the large DOP and the low SNR. In particular, looking at Fig. 8.4, the OD reconstruction improvement is obtained during all the transfer orbit (whenever signals from the LRNS are decoded), but it is especially relevant close to the Moon, where the RSS positioning uncertainty decreases of an order of magnitude when processing also the LRNS pseudo-range data. Moreover, Fig. 8.4 shows how it is possible to recover from a TCM before reaching the lunar orbit (final part of the transfer). This is particularly relevant because, in this final time window, the lunar orbit insertion needs to be executed, thus an accurate orbit reconstruction allows better targeting of the desired final lunar orbit.

This onboard approach allows to reduce the mission cost, especially the operational one, thanks to the decreased need to rely on the ground station infrastructure. Moreover, the usage of the GNSS+LRNS observables onboard reduce the load on the ground station infrastructure related to DWE radio links. At the same time, it is straightforward to apply it to a high number of missions. As stated before, the possibility of autonomously reconstructing the spacecraft trajectory onboard paves the way for fully autonomous onboard navigation and guidance of the satellite.

My research work is included in the following papers:

- [Audet et al., 2024], Positioning of a lunar surface rover on the south pole using LCNS and DEMs. *Advances in Space Research.*

- [Di Benedetto et al., 2022], An architecture for a lunar navigation system: Orbit determination and time synchronization. *Proceedings of the 8th International Colloquium on Scientific and Fundamental Aspects of GNSS.*

- [Molli et al., 2023], Navigation performance of low lunar orbit satellites using a lunar radio navigation satellite system. *In proceedings, pages 4051–4083.*

- [Iess et al., 2023], High performance orbit determination and time synchronization for lunar radio navigation systems. *Proceedings of the 36th International Technical Meeting of the Satellite Division of The Institute of Navigation (ION GNSS+ 2023).*

- [Iess et al., 2024], A novel orbit determination and time synchronization architecture for a radio navigation satellite constellation in the cislunar environment [under review]. *Navigation: Journal of the Institute of Navigation.*
- [Plumaris et al., 2024], Time synchronization strategies for a lunar radio navigation system. *In 75th International Astronautical Congress (IAC), Milan, Italy.*
- [Sesta et al., 2024], Atlas: Orbit determination and time transfer for a lunar radio navigation system [under review]. *Navigation: Journal of the Institute of Navigation.*

Bibliography

[Accubeat, 2021] Accubeat (2021). Uso datasheet. `https://www.accubeat.com/uso`. Retrieved 8 October 2023.

[Acton et al., 2018] Acton, C., Bachman, N., Semenov, B., and Wright, E. (2018). A look towards the future in the handling of space science mission geometry. *Planetary and Space Science*, 150:9–12.

[Acton, 1996] Acton, C. H. (1996). Ancillary data services of nasa's navigation and ancillary information facility. *Planetary and Space Science*, 44:65–70.

[Annex et al., 2020] Annex, A., Pearson, B., Seignovert, B., Carcich, B., Eichhorn, H., Mapel, J., von Forstner, J., McAuliffe, J., del Rio, J., Berry, K., Aye, K.-M., Stefko, M., de Val-Borro, M., Kulumani, S., and ya Murakami, S. (2020). Spiceypy: a pythonic wrapper for the spice toolkit. *Journal of Open Source Software*, 5:2050.

[Archinal et al., 2011] Archinal, B. A., A'Hearn, M. F., Bowell, E., Conrad, A., Consolmagno, G. J., Courtin, R., Fukushima, T., Hestroffer, D., Hilton, J. L., Krasinsky, G. A., Neumann, G., Oberst, J., Seidelmann, P. K., Stooke, P., Tholen, D. J., Thomas, P. C., and Williams, I. P. (2011). Report of the iau working group on cartographic coordinates and rotational elements: 2009. *Celestial Mechanics and Dynamical Astronomy*, 109:101–135.

[Arianespace, 2021] Arianespace (2021). *Ariane 6 User's Manual*, issue 2 revision 0 edition. Issued and approved by Roland LAGIER, Senior Vice President, Chief Technical Officer.

[Arias et al., 2011] Arias, E. F., Panfilo, G., and Petit, G. (2011). Timescales at the bipm. *Metrologia*, 48:S145–S153.

[Asmar et al., 2005] Asmar, S. W., Armstrong, J. W., Iess, L., and Tortora, P. (2005). Spacecraft doppler tracking: Noise budget and accuracy achievable in precision radio science observations. *Radio Science*, 40.

[Audet et al., 2024] Audet, Y., Melman, F. T., Molli, S., Sesta, A., Plumaris, M., Psychas, D., Swinden, R., Giordano, P., and Ventura-Traveset, J. (2024). Positioning of a lunar surface rover on the south pole using lcns and dems. *Advances in Space Research*, 74:2532–2550.

[BAE Systems, 2023] BAE Systems (2023). Bae systems technology to support european space agency mission to jupiter's

icy moons. https://www.baesystems.com/en/digital/article/bae-systems-technology-to-support-european-space-agency-mission-to-jupiters-icy-m Accessed: 2024-09-30.

[Barnes et al., 1971] Barnes, J. A., Chi, A. R., Cutler, L. S., Healey, D. J., Leeson, D. B., McGunigal, T. E., Mullen, J. A., Smith, W. L., Sydnor, R. L., Vessot, R. F. C., and Winkler, G. M. R. (1971). Characterization of frequency stability. *IEEE Transactions on Instrumentation and Measurement*, IM-20:105–120.

[Bauer et al., 2017] Bauer, S., Hussmann, H., Oberst, J., Dirkx, D., Mao, D., Neumann, G., Mazarico, E., Torrence, M., McGarry, J., Smith, D., and Zuber, M. (2017). Analysis of one-way laser ranging data to lro, time transfer and clock characterization. *Icarus*, 283:38–54.

[Bender, 1994] Bender, P. L. (1994). Proposed microwave transponders for early lunar robotic landers. *Advances in Space Research*, 14:233–242.

[Berner et al., 1999] Berner, J. B., Layland, J. M., Kinman, P. W., and Smith, J. R. (1999). Regenerative Pseudo-Noise Ranging for Deep-Space Applications. *Telecommunications and Mission Operations Progress Report*, 137:1–18.

[BIPM, 2023] BIPM (2023). Circular t 425. https://www.bipm.org/en/time-ftp/circular-t. Accessed: 2024-09-30, ISSN 1143-1393.

[Bury et al., 2020] Bury, G., Sośnica, K., Zajdel, R., and Strugarek, D. (2020). Toward the 1-cm galileo orbits: challenges in modeling of perturbing forces. *Journal of Geodesy*, 94:16.

[Bury et al., 2019] Bury, G., Zajdel, R., and Sośnica, K. (2019). Accounting for perturbing forces acting on galileo using a box-wing model. *GPS Solutions*, 23:74.

[Cappuccio et al., 2020] Cappuccio, P., Notaro, V., di Ruscio, A., Iess, L., Genova, A., Durante, D., di Stefano, I., Asmar, S. W., Ciarcia, S., and Simone, L. (2020). Report on first inflight data of bepicolombo's mercury orbiter radio science experiment. *IEEE Transactions on Aerospace and Electronic Systems*, 56:4984–4988.

[Cappuccio et al., 2024] Cappuccio, P., Sesta, A., Benedetto, M. D., Durante, D., Filippis, U. D., di Stefano, I., Iess, L., Mackenzie, R., and Godard, B. (2024). Analysis of radio science data from the kat instrument of the 3gm experiment during juice's early cruise phase [under review]. *Aerospace*.

[Capuano et al., 2016] Capuano, V., Basile, F., Botteron, C., and Farine, P.-A. (2016). Gnss-based orbital filter for earth moon transfer orbits. *Journal of Navigation*, 69:745–764.

[CCSDS, 2011] CCSDS (2011). *CCSDS 415.1-B-1 "Data Transmission and PN Ranging for 2 GHz CDMA" (Blue Book)*.

[CCSDS, 2014] CCSDS (2014). *Pseudo-Noise (PN) Ranging Systems. Report Concerning Space Data System Standards (Green Book) Issue 2, CCSDS 414.0-G-2*.

[CCSDS, 2021] CCSDS (2021). *Radio Frequency and Modulation System – Informational Report (Green Book).*

[CCSDS, 2022] CCSDS (2022). *Pseudo-noise (PN) ranging systems. Recommendation for space data system standards (Blue Book) Issue 3, CCSDS 414.1-B-3.*

[Cheetham et al., 2022] Cheetham, B., Gardner, T., Forsman, A., Kayser, E., and Clarkson, M. (2022). Capstone: A unique cubesat platform for a navigation demonstration in cislunar space. In *ASCEND 2022*. American Institute of Aeronautics and Astronautics.

[Cortinovis et al., 2023] Cortinovis, M., Iiyama, K., and Gao, G. (2023). Satellite ephemeris approximation methods to support lunar positioning, navigation, and timing services. pages 3647–3663.

[Delva et al., 2012] Delva, P., Meynadier, F., Poncin-Lafitte, C. L., Laurent, P., and Wolf, P. (2012). Time and frequency transfer with a microwave link in the aces/pharao mission. In *2012 European Frequency and Time Forum*, pages 28–35. IEEE.

[Delépaut et al., 2020] Delépaut, A., Giordano, P., Ventura-Traveset, J., Blonski, D., Schönfeldt, M., Schoonejans, P., Aziz, S., and Walker, R. (2020). Use of gnss for lunar missions and plans for lunar in-orbit development. *Advances in Space Research*, 66(12):2739–2756. Scientific and Fundamental Aspects of GNSS - Part 1.

[Di Benedetto et al., 2022] Di Benedetto, M., Boscagli, G., De Marchi, F., Durante, D., Santi, F., Sesta, A., Plumaris, M. K., Fienga, A., Linty, N., Sośnica, K., Belfi, J., and Iess, L. (2022). An architecture for a lunar navigation system: Orbit determination and time synchronization. In *Proceedings of the 8th International Colloquium on Scientific and Fundamental Aspects of GNSS*, Sofia.

[Donà and Iess, 2017] Donà, G. and Iess, L. (2017). Cdma implementation for tt&c and precision navigation - scenario analysis and signal definition. [technical note tn-002-1]. ESA Contract No. 4000117076/16/NL/FE.

[Dousa and Vaclavovic, 2015] Dousa, J. and Vaclavovic, P. (2015). *The Evaluation of Ground-Based GNSS Tropospheric Products at Geodetic Observatory Pecný*, pages 759–765.

[DSN, 2015] DSN (2015). *Atmospheric and Environmental Effects.*

[Duchayne et al., 2009] Duchayne, L., Mercier, F., and Wolf, P. (2009). Orbit determination for next generation space clocks. *Astronomy & Astrophysics*, 504:653–661.

[Ehlmann et al., 2022] Ehlmann, B. L., Klima, R. L., Seybold, C. C., Klesh, A. T., Au, M. H., Bender, H. A., Bennett, C. L., Blaney, D. L., Bowles, N., Calcutt, S., Copley-Woods, D., Dickson, J. L., Djotni, K., Hanna, K. D., Edwards, C. S., Evans, R., Felder, E., Fogg, R., Green, R. O., Hawkins, G., House, M., Islas, S., Lantoine, G., Linch, S., McCaa, T., McKinley, I., Merkley, T. F., Miura,

J. K., Pieters, C. M., Santiago, W., Scire, E., Sherwood, R., Shirley, K., Smith, C., Sondheim, M., Sullivan, P., Temples, J., Thompson, D. R., Waldorff, K. I., Williamson, W. R., Warren, T. J., Wood, J. L., and Zareh, S. (2022). Nasa's lunar trailblazer mission: A pioneering small satellite for lunar water and lunar geology. In *2022 IEEE Aerospace Conference (AERO)*, pages 1–14. IEEE.

[Engel, 2008] Engel, U. (2008). Improving position accuracy by combined processing of galileo and gps satellite signals. In *2008 11th International Conference on Information Fusion*, pages 1–8.

[ESA, 2022a] ESA (2022a). Argonaut. `https://www.esa.int/Science_Exploration/Human_and_Robotic_Exploration/Exploration/Argonaut`. 09-08-2024.

[ESA, 2022b] ESA (2022b). Godot user documentation. `https://godot.io.esa.int/godotpy`. 26-09-2024.

[Estler et al., 2002] Estler, W., Edmundson, K., Peggs, G., and Parker, D. (2002). Large-scale metrology – an update. *CIRP Annals*, 51(2):587–609.

[Euroconsult, 2023] Euroconsult (2023). Prospect for space exploration, 4th edition. `https://digital-platform.euroconsult-ec.com/product/prospects-for-space-exploration/`. 09-08-2024.

[European GNSS (Galileo), 2021] European GNSS (Galileo) (2021). Service definition document. issue 1.2.

[European GNSS (Galileo) Open Service, 2016] European GNSS (Galileo) Open Service (2016). Ionospheric correction algorithm for galileo single frequency users.

[Feltens et al., 2018] Feltens, J., Bellei, G., Springer, T., Kints, M. V., Zandbergen, R., Budnik, F., and Schönemann, E. (2018). Tropospheric and ionospheric media calibrations based on global navigation satellite system observation data. *Journal of Space Weather and Space Climate*, 8:A30.

[Gentleman, 1975] Gentleman, M. (1975). Error analysis of qr decomposition by givens transformations. *Linear Algebra and its Applications*, 10:189–197.

[Giordano et al., 2021a] Giordano, P., Grenier, A., Zoccarato, P., Bucci, L., Cropp, A., Swinden, R., Otero, D., Eldali, W., Care, W., Duvet, L., Hufenbach, B., Joly, F., and Ventura-Traveset, J. (2021a). Moonlight navigation service - how to land on peaks of eternal light. In *72nd International Astronautical Congress (IAC)*. [Paper presentation].

[Giordano et al., 2021b] Giordano, P., Grenier, A., Zoccarato, P., Swinden, R., Trenta, D., Schönemann, E., Liucci, F., Enderle, W., Hufenbach, B., and Ventura-Traveset, J. (2021b). Orbit determination and time synchronisation in lunar orbit with gnss -lunar pathfinder experiment.

[Giordano et al., 2022] Giordano, P., Malman, F., Swinden, R., Zoccarato, P., and Ventura-Traveset, J. (2022). The lunar pathfinder pnt experiment and moonlight navigation service: The future of lunar position, navigation and timing. pages 632–642.

[Gregnanin et al., 2012] Gregnanin, M., Bertotti, B., Chersich, M., Fermi, M., Iess, L., Simone, L., Tortora, P., and Williams, J. (2012). Same beam interferometry as a tool for the investigation of the lunar interior. *Planetary and Space Science*, 74:194–201.

[Grenier et al., 2022] Grenier, A., Giordano, P., Bucci, L., Cropp, A., Zoccarato, P., Richard, S., and Ventura-Traveset, J. (2022). Positioning and velocity performance levels for a lunar lander using a dedicated lunar communication and navigation system. *NAVIGATION: Journal of the Institute of Navigation*, 69:navi.513.

[Hegarty and Kaplan, 2005] Hegarty, C. and Kaplan, E. (2005). *Understanding GPS Principles and Applications, Second Edition.*

[Holmes, 1982] Holmes, J. K. (1982). *Coherent spread spectrum systems.*

[Howe et al., 1989] Howe, D., Hanson, D., Jespersen, J., and Lombardi, M. (1989). Satellite two-way time transfer: Fundamentals and recent progress. In *Proceedings of the 21st Annual Precise Time and Time Interval Systems and Applications Meeting*, pages 117–130, Redondo Beach, California.

[Iess et al., 2021] Iess, L., Asmar, S. W., Cappuccio, P., Cascioli, G., Marchi, F. D., di Stefano, I., Genova, A., Ashby, N., Barriot, J. P., Bender, P., Benedetto, C., Border, J. S., Budnik, F., Ciarcia, S., Damour, T., Dehant, V., Achille, G. D., Ruscio, A. D., Fienga, A., Formaro, R., Klioner, S., Konopliv, A., Lemaître, A., Longo, F., Mercolino, M., Mitri, G., Notaro, V., Olivieri, A., Paik, M., Palli, A., Schettino, G., Serra, D., Simone, L., Tommei, G., Tortora, P., Hoolst, T. V., Vokrouhlický, D., Watkins, M., Wu, X., and Zannoni, M. (2021). Gravity, geodesy and fundamental physics with bepicolombo's more investigation. *Space Science Reviews*, 217:21.

[Iess et al., 2023] Iess, L., Benedetto, M. D., Boscagli, G., Racioppa, P., Sesta, A., Marchi, F. D., Cappuccio, P., Durante, D., Molli, S., Plumaris, M. K., Tartaglia, P., Santi, F., Fienga, A., Linty, N., Sosnica, K., Belfi, J., Giordano, P., Swinden, R., and Ventura-Traveset, J. (2023). High performance orbit determination and time synchronization for lunar radio navigation systems. In *Proceedings of the 36th International Technical Meeting of the Satellite Division of The Institute of Navigation (ION GNSS+ 2023)*, pages 4029–4050.

[Iess et al., 2024] Iess, L., Benedetto, M. D., Boscagli, G., Racioppa, P., Sesta, A., Marchi, F. D., Cappuccio, P., Durante, D., Molli, S., Plumaris, M. K., Tartaglia, P., Santi, F., Fienga, A., Linty, N., Sosnica, K., Belfi, J., Giordano, P., Swinden, R., and Ventura-Traveset, J. (2024). A novel orbit determination and time synchronization architecture for a radio navigation satellite constellation in the cislunar environment [under review]. *Navigation: Journal of the Institute of Navigation.*

[Iess et al., 2014] Iess, L., Benedetto, M. D., James, N., Mercolino, M., Simone, L., and Tortora, P. (2014). Astra: Interdisciplinary study on enhancement of the end-to-end accuracy for spacecraft tracking techniques. *Acta Astronautica*, 94:699–707.

[ISECG, 2018] ISECG (2018). The global exploration roadmap.

[Langley et al., 2017] Langley, R. B., Teunissen, P. J., and Montenbruck, O. (2017). *Introduction to GNSS*, pages 3–23. Springer International Publishing.

[Lasagni Manghi et al., 2023] Lasagni Manghi, R., Bernacchia, D., Casajus, L. G., Zannoni, M., Tortora, P., Martellucci, A., Vicente, J. D., Villalvilla, J., Maschwitz, G., Cappuccio, P., and Iess, L. (2023). Tropospheric delay calibration system performance during the first two bepicolombo solar conjunctions. *Radio Science*, 58.

[Lemoine et al., 2014] Lemoine, F. G., Goossens, S., Sabaka, T. J., Nicholas, J. B., Mazarico, E., Rowlands, D. D., Loomis, B. D., Chinn, D. S., Neumann, G. A., Smith, D. E., and Zuber, M. T. (2014). Grgm900c: A degree 900 lunar gravity model from grail primary and extended mission data. *Geophysical Research Letters*, 41:3382–3389.

[Lemoine et al., 2019] Lemoine, J.-M., Biancale, R., Reinquin, F., Bourgogne, S., and Gégout, P. (2019). CNES/GRGS RL04 Earth gravity field models, from GRACE and SLR data.

[Li et al., 2021] Li, C., Zuo, W., Wen, W., Zeng, X., Gao, X., Liu, Y., Fu, Q., Zhang, Z., Su, Y., Ren, X., Wang, F., Liu, J., Yan, W., Tan, X., Liu, D., Liu, B., Zhang, H., and Ouyang, Z. (2021). Overview of the chang'e-4 mission: Opening the frontier of scientific exploration of the lunar far side. *Space Science Reviews*, 217:35.

[Li et al., 2019] Li, X., Yuan, Y., Huang, J., Zhu, Y., Wu, J., Xiong, Y., Li, X., and Zhang, K. (2019). Galileo and qzss precise orbit and clock determination using new satellite metadata. *Journal of Geodesy*, 93:1123–1136.

[Linfield et al., 1996] Linfield, R. P., Keihm, S. J., Teitelbaum, L. P., Walter, S. J., Mahoney, M. J., Treuhaft, R. N., and Skjerve, L. J. (1996). A test of water vapor radiometer-based troposphere calibration using very long baseline interferometry observations on a 21-km baseline. *Radio Science*, 31:129–146.

[Liu et al., 2021] Liu, Q., Hernández-Pajares, M., Yang, H., Monte-Moreno, E., Roma-Dollase, D., García-Rigo, A., Li, Z., Wang, N., Laurichesse, D., Blot, A., Zhao, Q., Zhang, Q., Hauschild, A., Agrotis, L., Schmitz, M., Wübbena, G., Stürze, A., Krankowski, A., Schaer, S., Feltens, J., Komjathy, A., and Ghoddousi-Fard, R. (2021). The cooperative igs rt-gims: a reliable estimation of the global ionospheric electron content distribution in real time. *Earth System Science Data*, 13:4567–4582.

[Machuzak et al., 2008] Machuzak, R., Berner, J., Pham, T., and Stipanuk, J. (2008). Deep space network (dsn) external interface specification: Trk-2-23 media calibration interface. Technical Report JPL D-16765, TRK-2-23, Revision C, Jet Propulsion Laboratory, California Institute of Technology, Pasadena, California. Revision C: draft March 5, 2008.

[Marquis and Reigh, 2015] Marquis, W. A. and Reigh, D. L. (2015). The gps block iir and iir-m broadcast l-band antenna panel: Its pattern and performance. *Navigation*, 62:329–347.

[Melman et al., 2022] Melman, F. T., Zoccarato, P., Orgel, C., Swinden, R., Giordano, P., and Ventura-Traveset, J. (2022). Lcns positioning of a lunar surface rover using a dem-based altitude constraint. *Remote Sensing*, 14:3942.

[Meurer and Antreich, 2017] Meurer, M. and Antreich, F. (2017). *Signals and Modulation*, pages 91–119. Springer International Publishing.

[Molli et al., 2023] Molli, S., Tartaglia, P., Audet, Y., Sesta, A., Plumaris, M., Melman, F., Swinden, R., Giordano, P., and Ventura-Traveset, J. (2023). Navigation performance of low lunar orbit satellites using a lunar radio navigation satellite system. pages 4051–4083.

[Montenbruck et al., 2018] Montenbruck, O., Steigenberger, P., and Hauschild, A. (2018). Multi-gnss signal-in-space range error assessment – methodology and results. *Advances in Space Research*, 61:3020–3038.

[Moonlight Team, 2024] Moonlight Team (2024). Moonlight lcns esa service requirements document (esrd).

[Moyer, 2003] Moyer, T. D. (2003). *Formulation for Observed and Computed Values of Deep Space Network Data Types for Navigation*. Wiley.

[Murata et al., 2022] Murata, M., Kawano, I., and Kogure, S. (2022). Lunar navigation satellite system and positioning accuracy evaluation. pages 582–586.

[NASA, 2020a] NASA (2020a). Nasa names companies to develop human landers for artemis moon missions. `https://www.nasa.gov/news-release/nasa-names-companies-to-develop-human-landers-for-artemis-moon-missions/`. 10-08-2024.

[NASA, 2020b] NASA (2020b). Nasa's lunar exploration program overview.

[NASA and ESA, 2023] NASA and ESA (2023). Lunanet interoperability specification document. Accessed: 2024-09-03.

[Niell, 1996] Niell, A. E. (1996). Global mapping functions for the atmosphere delay at radio wavelengths. *Journal of Geophysical Research: Solid Earth*, 101:3227–3246.

[Orolia, 2023a] Orolia (2023a). minirafs datasheet. `https://www.orolia.com/product/minirafs-rb-atomic-frequency-standard/`. Retrieved 8 October 2023.

[Orolia, 2023b] Orolia (2023b). Rafs datasheet. `https://www.orolia.com/product/rafs/`. Retrieved 8 October 2023.

[Park et al., 2012] Park, R. S., Asmar, S. W., Fahnestock, E. G., Konopliv, A. S., Lu, W., and Watkins, M. M. (2012). Gravity recovery and interior laboratory simulations of static and temporal gravity field. *Journal of Spacecraft and Rockets*, 49:390–400.

[Parker et al., 2022] Parker, J. J. K., Dovis, F., Anderson, B., Ansalone, L., Ashman, B., Bauer, F. H., D'Amore, G., Facchinetti, C., Fantinato, S., Impresario, G., McKim, S. A., Miotti, E., Miller, J. J., Musmeci, M., Pozzobon, O., Schlenker, L., Tuozzi, A., and Valencia, L. (2022). The lunar gnss receiver experiment (lugre). pages 420–437.

[Plumaris et al., 2024] Plumaris, M., Di Benedetto, M., De Marchi, F., Iess, L., and Sesta, A. (2024). Time synchronization strategies for a lunar radio navigation system. In *75th International Astronautical Congress (IAC)*, Milan, Italy. IAC-24-B2,IPB,22,x85340.

[Rovelli and Donà, 2016] Rovelli, D. and Donà, G. (2016). Code division multiplexing transmitter options for single aperture multiple link applications. In *3rd ESA Workshop on Advanced Flexible Telecom Payloads*.

[Schönfeldt et al., 2020] Schönfeldt, M., Grenier, A., Delépaut, A., Giordano, P., Swinden, R., and Ventura-Traveset, J. (2020). Across the lunar landscape: Towards a dedicated lunar pnt system. Accessed: 2024-09-03.

[Sesta et al., 2024] Sesta, A., Durante, D., Boscagli, G., Cappuccio, P., Benedetto, M. D., di Stefano, I., Plumaris, M. K., Racioppa, P., Iess, L., Giordano, P., Swinden, R., and Ventura-Traveset, J. (2024). Atlas: orbit determination and time transfer for a lunar radio navigation system [under review]. *Navigation: Journal of the Institute of Navigation*.

[SFCG, 2023a] SFCG (2023a). Recommendation sfcg 32-2r5 communication and positioning, navigation, and timing frequency allocations and sharing int the lunar region.

[SFCG, 2023b] SFCG (2023b). Recommendation sfcg 41-1 efficient spectrum utilization for space research systems in the lunar region.

[Smith and Weintraub, 1953] Smith, E. and Weintraub, S. (1953). The constants in the equation for atmospheric refractive index at radio frequencies. *Proceedings of the IRE*, 41:1035–1037.

[Stallo et al., 2023] Stallo, C., Lauro, C. D., Carosi, M., Zini, E. E., Musacchio, D., Leo, L. D., Cretoni, D., Laurenti, M., and Henno, B. (2023). Performance analysis of lunar radio navigation odts system. pages 190–203.

[Tapley et al., 2004] Tapley, B. D., Schutz, B. E., and Born, G. H. (2004). *Statistical Orbit Determination*. Elsevier.

[Teunissen and Montenbruck, 2017] Teunissen, P. J. and Montenbruck, O., editors (2017). *Springer Handbook of Global Navigation Satellite Systems*. Springer International Publishing.

[Timmer and Koenig, 1995] Timmer, J. and Koenig, M. (1995). On generating power law noise. *Astronomy and Astrophysics*, 300:707.

[Tondaś et al., 2020] Tondaś, D., Kapłon, J., and Rohm, W. (2020). Ultra-fast near real-time estimation of troposphere parameters and coordinates from gps data. *Measurement*, 162:107849.

[Vondrak et al., 2010] Vondrak, R., Keller, J., Chin, G., and Garvin, J. (2010). Lunar reconnaissance orbiter (lro): Observations for lunar exploration and science. *Space Science Reviews*, 150:7–22.

[Wang et al., 2019] Wang, P., Wang, G., Gao, Y., Cai, H., and Liu, N. (2019). Comparison of vlbi and gnss common view for time transfer. *International Journal of Metrology and Quality Engineering*, 10:15.

[Wang et al., 2018] Wang, T., Ruf, C., Block, B., McKague, D., and Gleason, S. (2018). Characterization of gps l1 eirp: Transmit power and antenna gain pattern. pages 2879–2890.